

General relativity and its classical modification in gravitational collapse

Justin Lloyd Ripley

A Dissertation

Presented to the Faculty
of Princeton University
in Candidacy for the Degree
of Doctor of Philosophy

Recommended for Acceptance by
the Department of
Physics

Advisor: Frans Pretorius

September 2020

© Copyright 2020 by Justin Lloyd Ripley.

All rights reserved.

Abstract

In this thesis, we describe numerical spherical collapse solutions to a “modified gravity” theory, Einstein dilaton Gauss-Bonnet (EdGB) gravity. Of the class of all known modified gravity theories, EdGB gravity has attracted recent attention due to speculations that the theory may have a classically well-posed initial value formulation and yet also exhibit stable scalarized black hole solutions (what makes this surprising is the plethora of black hole “no hair theorems”, the assumptions behind which EdGB gravity manages to avoid). If EdGB gravity indeed possess these properties, it would be an ideal theory to perform model-selection tests against general relativity (GR) in binary black hole merger using gravitational waves. Furthermore, the theory is an important member of the so-called “Horndeski theories”, which have been invoked to construct, e.g. nonsingular black hole and cosmological solutions, and to address the classical flatness and horizon problems of the early universe.

In constructing numerical solutions to EdGB gravity (without any approximations beyond the restriction to spherically symmetric configurations), we are able to carefully examine various claims made in the literature about EdGB gravity, perhaps most importantly whether or not the theory admits a classically well-posed initial value problem. One conclusion of these studies has been, at least in spherical collapse, EdGB gravity can *dynamically* lose hyperbolicity, which shows EdGB gravity is fundamentally of “mixed type”. Mixed type problems appear in earlier problems in mathematical physics, perhaps most notably in the problem of steady state, inviscid, compressible fluid flow. The loss of hyperbolicity and subsequent formation of “el-

liptic regions” outside of any sort of horizon implies that the theory violates cosmic censorship, broadly defined. Arguably it is clear that this result is gauge invariant, although we do not formulate a rigorous proof that this is so. In addition to discussing the hyperbolicity of EdGB gravity, we discuss several other interesting features to the numerical solutions, including the formation of scalarized black hole solutions in the theory, at least for certain parameter ranges for the theory and certain open sets of initial data.

To my family.

Acknowledgements

I could not have completed this thesis without my adviser, Frans Pretorius, who has been a constant source of friendly and expert help and ideas. I have come to truly appreciate the power of solving problems using numerical methods by working with you. Thank you for your guidance and for your confidence in me. I also thank Paul Steinhardt, whose expertise and ideas in theoretical cosmology inspired parts of the research contained in this thesis. I thank David Spergel for supervising my experimental project and for generously sharing his time to discuss current research in cosmology and astrophysics. I am thankful to Leo Stein, the second reader for this thesis, for his continual interest in my research and for providing useful, detailed, and extensive comments which improved this thesis. I thank Helvi Witek and Nicolas Yunes for their thoughtful comments on the work that went into [RP20a] and chapter 4 of this thesis. I am thankful to Mihalis Dafermos for always being willing to take time to discuss mathematical relativity. I greatly benefited from attending his interesting seminars on that subject. I thank Mariangela Lisanti and Matias Zaldarriaga for graciously allowing me to participate in their research groups early in my graduate career. I thank Lyman Page and Mihalis Dafermos for serving on my thesis committee.

I have benefited from working with many of the postdoctoral researchers at Princeton and the Institute for Advanced Study during my tenure here. I thank Anna Ijjas for collaboration on [IRS16], and I especially wish to thank Kent Yagi for his help in the project [RY18]. That project would not have happened without his guidance and encouragement. I thank Valentin Assassi, Tobias Baldauf, Miriam Cabero-Müller,

Will Cook, Evan Goetz, and especially Lasha Berezhiani, Vasileios Paschalidis, and Huan Yang for conversations and advice that helped shape my thinking on this subject. Finally, I wish to thank Elena Giorgi and Nicholas Loutrel for the enjoyable collaboration on several works in progress we have done together, which unfortunately could not be included in this thesis.

I thank my fellow graduate students in the gravitational theory group—Roman Kolevaton, Aaron Levy, Seth Olsen, Alex Pandya, Javier Roulet, Nikolay Sukhov, and Wayne Zhao—for the many interesting conversations that have contributed to my graduate education as a whole.

I wish to thank Kate Brosowsky and Angela Lewis for their help throughout my years as a graduate student, and for making things run so smoothly in Jadwin.

Finally, I am profoundly thankful to my family and friends, who have all added so much to my life.

Contents

Abstract	iii
Acknowledgements	vi
Contents	viii
1 Introduction	1
1.1 Review and notation	1
1.1.1 Notation	1
1.1.2 Einstein equations	3
1.2 A brief survey of modified gravity theories	4
1.3 Motivations for studying modified gravity	6
1.3.1 Finding a complete theory of quantum gravity	6
1.3.2 Determining dynamics of the early universe	6
1.3.3 Determining dynamics of the late universe	8
1.3.4 Interior of black holes	10
1.3.5 Understanding complexity of solutions to partial differential equations of classical physics	10
1.3.6 Testing general relativity in the strong-field, dynamical regime	11
1.4 Modified gravity theories must admit a mathematically consistent in- terpretation	12
1.4.1 Quantizability	13

1.4.2	Well-posed initial value problem	14
1.4.3	Quantizability and having a well-posed initial value problem are not equivalent	17
1.4.4	Linear stability and having a well-posed initial value problem are not equivalent	18
1.5	Higher derivative theories, effective field theory (EFT), and order re- duction	20
1.6	EdGB gravity	23
1.6.1	The model	23
1.6.2	Method of study: spherically symmetric dynamics	24
2	Dilaton field dynamics during spherical collapse in EdGB gravity with linear Gauss-Bonnet coupling	26
2.1	Basic equations	26
2.1.1	Linearly coupled EdGB gravity	26
2.1.2	Polar coordinates	27
2.1.3	Boundary and regularity conditions	29
2.1.4	Initial data	30
2.2	Numerical methods	30
2.2.1	CN Hyperbolic PDE solver for Q and P	32
2.2.2	RK4 PDE solver for Q and P	33
2.2.3	ODE integrator for B	34
2.2.4	ODE integrator for A	35
2.2.5	Partially Constrained Evolution	36
2.3	Hyperbolicity analysis	36
2.3.1	Characteristics calculation	38
2.3.2	Invariance of the characteristics under coordinate transforma- tions	39
2.3.3	Horizons	41

2.4	Quasi-local mass	41
2.5	Null convergence condition	42
2.6	Results: Hyperbolicity	44
2.6.1	<i>Dynamic</i> loss of hyperbolicity and the “mixed type” properties of EdGB gravity	44
2.6.2	Scaling and loss of hyperbolicity	50
2.7	Results: Misner-Sharp mass and Null Convergence Condition	51
2.8	Convergence of simulations	55
2.9	Conclusion	55
3	Black holes in EdGB gravity with a linear Gauss-Bonnet coupling	59
3.1	Introduction	59
3.2	Equations of motion	63
3.3	Description of code and simulations	65
3.3.1	Diagnostics	65
3.3.2	Spatial compactification	68
3.3.3	Initial data	69
3.3.4	Excision	69
3.3.5	Fixed mesh refinement with a hyperbolic-ODE system	71
3.4	Scalarized black holes: numerical results	71
3.4.1	Overview of simulations and plots	71
3.4.2	Growth of “hair” from Schwarzschild initial data	72
3.4.3	Perturbed Schwarzschild initial data	75
3.4.4	Internal structure of an EdGB black hole, and the near extremal limit	77
3.5	Discussion	83
3.6	Appendix: Convergence of an independent residual	86

4	Dynamics of a \mathbb{Z}_2 symmetric EdGB gravity in spherical symmetry	88
4.1	Introduction	88
4.2	Equations of motion	90
4.3	Earlier work on \mathbb{Z}_2 symmetric EdGB gravity	92
4.4	Description of code and simulations	94
4.4.1	Code description	94
4.4.2	Diagnostics	95
4.5	Characteristics versus linearized perturbation analysis	96
4.6	Initial data	97
4.6.1	General considerations	97
4.6.2	Black hole initial data with a small exterior scalar pulse	98
4.6.3	Approximate scalarized profile	99
4.7	Numerical results	100
4.7.1	Compact scalar pulse initial data	100
4.7.2	Numerical results: approximately scalarized black hole initial data	102
4.8	Discussion	105
5	Concluding remarks	108
A	Covariant treatment of spherically symmetric spacetimes	110
A.1	Spherically symmetric spacetimes	110
A.2	Kodama vector and Misner-Sharp mass	112
A.3	Misner-Sharp mass and EdGB gravity	114
A.4	Noether charge for shift-symmetric EdGB gravity	115
B	An adaptive mesh code for 1 + 1 dimensional systems	117
B.1	Adaptive mesh refinement for hyperbolic systems	118
B.2	Including Ordinary Differential Equations	120

B.3 Fixed mesh refinement around a black hole	121
C Variation of the Gauss-Bonnet scalar	122
D Decoupled scalar profile for linear EdGB coupling	124

Chapter 1

Introduction

In this thesis we describe several investigations of the nonlinear dynamics of a modified gravity theory called Einstein dilaton Gauss-Bonnet (EdGB) gravity. EdGB gravity is called a “modified gravity” theory, as Einstein’s General Relativity (GR) is taken to be *the* current theory of gravity, due to its successful application to essentially all gravitational problems within experimental test/observational reach since its introduction over 100 years ago¹. Despite the well documented success of GR, there is a sizable community of researchers who study modified gravity theories, and in this Introduction we provide several reasons for studying these theories.

1.1 Review and notation

1.1.1 Notation

We begin with a very brief review of GR to set our notation. Standard textbooks on GR include [Wei72, MTW17, Wal84, Car04]. In this thesis we follow the sign conventions of Misner, Thorne, and Wheeler (MTW) [MTW17] (for example $-+++$ sign convention for the metric), and we will use geometric units ($8\pi G = c = 1$).

¹For a detailed review of tests of GR before the first gravitational wave observation of binary compact object coalescence by the LIGO/Virgo collaboration, see [Wil14]

In GR, gravity is modeled in terms of a four dimensional Lorentzian differentiable manifold called spacetime². While we will not provide a detailed account of (pseudo) Riemannian geometry, for completeness we list the relevant geometric objects that will appear in this thesis. For more discussion on Riemannian geometry, see the above referenced books or for example [FdC13]. We work in a coordinate basis. The metric tensor is $g_{\mu\nu}$. Covariant derivatives are denoted by ∇_α and partial derivatives by ∂_α . The Riemann tensor describes the curvature of spacetime:

$$R^\alpha{}_{\mu\beta\nu} = 2\partial_{[\beta}\Gamma^\alpha{}_{\nu]\mu} + 2\Gamma^\alpha{}_{\lambda[\beta}\Gamma^\lambda{}_{\nu]\mu}, \quad (1.1)$$

where the $\Gamma^\lambda{}_{\rho\sigma}$ are the Christoffel symbols

$$\Gamma^\lambda{}_{\rho\sigma} = \frac{1}{2}g^{\lambda\kappa} (\partial_\rho g_{\kappa\sigma} + \partial_\sigma g_{\kappa\rho} - \partial_\kappa g_{\rho\sigma}), \quad (1.2)$$

and square brackets denote antisymmetrization of indices. The trace of the Riemann tensor is the Ricci tensor

$$R_{\mu\nu} \equiv R^\alpha{}_{\mu\alpha\nu}, \quad (1.3)$$

and the trace of the Ricci tensor is the Ricci scalar

$$R \equiv R^\alpha{}_\alpha. \quad (1.4)$$

The tracefree part of the Riemann tensor is called the Weyl tensor. For a n dimensional spacetime (although we will only be consider with $n = 4$ in this thesis)

$$W^{\alpha\mu}{}_{\beta\nu} \equiv R^{\alpha\mu}{}_{\beta\nu} - \frac{2}{n-2}\delta^{[\alpha}{}_{[\beta}R^{\mu]}{}_{\nu]} + \frac{2}{(n-1)(n-3)}\delta^{[\alpha}{}_{[\beta}\delta^{\mu]}{}_{\nu]}R. \quad (1.5)$$

The Weyl tensor has the same algebraic symmetries as the Riemann tensor. From Eq. (1.5) we see that we can write the Riemann tensor as a sum of the Weyl tensor, the Ricci tensor, the metric tensor, and the Ricci scalar.

²Note it is possible to interpret the equations of motion of GR nongeometrically [Wei72].

1.1.2 Einstein equations

In GR, the dynamics of the spacetime metric $g_{\mu\nu}$ are prescribed by the Einstein Equations

$$G_{\mu\nu} = T_{\mu\nu}, \tag{1.6}$$

where $G_{\mu\nu}$ is the Einstein tensor,

$$G_{\mu\nu} \equiv R_{\mu\nu} - \frac{1}{2}g_{\mu\nu}R, \tag{1.7}$$

and $T_{\mu\nu}$ is the stress-energy tensor. The stress-energy tensor can be derived by varying the *matter Lagrangian* L_m with respect to the metric

$$T_{\mu\nu} \equiv -\frac{2}{\sqrt{-g}} \frac{\delta L_m}{\delta g^{\mu\nu}}. \tag{1.8}$$

From the Bianchi identities, $G_{\mu\nu}$ is divergenceless. From the Einstein equations we see that $T_{\mu\nu}$ must be divergenceless as well. This requirement on the stress-energy tensor can be interpreted as “energy conservation”, although there is no coordinate invariant notion of quasilocal energy in GR (for a review see [Sza09])³.

The stress-energy tensor is less well-understood than the Einstein tensor. The form of the Einstein tensor is essentially fixed once one demands a covariant equation of motion for a metric field that has only up to second order equations of motion [Lov71]. While various *energy conditions* have been proposed to constrain the form of $T_{\mu\nu}$ ⁴, there are no universally accepted conditions for what form $T_{\mu\nu}$ *must* take in order to obtain sensible classical differential equations for the Einstein equations (for a discussion of some of the candidate conditions see e.g. [HE75]). Instead, the precise form of the stress-energy tensor depends on the physical problem being studied, and must be determined through careful experimental and observational work. In fact, many current research questions in cosmology and astrophysics can be phrased

³ We note though that in spherical symmetry there is a natural notion of quasilocal mass, which we use frequently in this thesis; see e.g. Appendix A.

⁴For a classic discussion the energy conditions see [HE75].

theory	date first introduced
Massive gravity	1939 [FPD39]
Brans-Dicke gravity	1961 [BD61]
Lovelock gravity	1971 [Lov71]
Horndeski gravity	1974 [Hor74]
Einstein dilaton Gauss-Bonnet (EdGB) gravity	1985 [Zwi85]

Table 1.1: Notable modified gravity theories through the ages. This is by no means an exhaustive list, and we have made no attempt to document the various extensions of these theories beyond their original publication in this table.

in terms of the stress-energy tensor. For example, it is presently unknown what is the precise form of the stress-energy tensor for dark matter or dark energy, or even what is the precise form of the stress-energy tensor of the matter that makes up the interior of a neutron star.

1.2 A brief survey of modified gravity theories

Ever since Einstein introduced his theory of General Relativity, researchers have attempted to generalize, extend, or modify the theory. For reference in Table. (1.1) we list some influential modified gravity theories and the dates they were introduced.

The authors cited in Table (1.1) mainly provide more theoretically oriented reasons for modifying GR (if they give reasons at all). Fierz and Pauli [FPD39] were not considering gravitational theories per say, but were simply considering the equations of motion for massive arbitrary spin particles. They found that in order to obtain a mass term for a spin-2 field that has an action invariant under the symmetry (here $h_{\mu\nu}$ is the linearized spin-2 field about Minkowski space $\eta_{\mu\nu}$)

$$h_{\mu\nu} \rightarrow h_{\mu\nu} + \partial_\mu \xi_\nu + \partial_\nu \xi_\mu, \quad (1.9)$$

fixed the mass term to take a specific form:

$$\mathcal{L}_{FP} \supset m^2 (h_{\mu\nu} h^{\mu\nu} - (\eta^{\mu\nu} h_{\mu\nu})^2). \quad (1.10)$$

The symmetry (1.9) is the linearization of the diffeomorphism $\mathcal{L}_\xi g_{\mu\nu}$ about Minkowski spacetime, where \mathcal{L}_ξ is the Lie derivative with respect to the vector ξ^μ . Massive gravity has since been extended in a nonperturbative framework (for a review see [Hin12]).

Brans and Dicke considered modifying GR to make the theory more consistent with *Mach's principle*, which roughly stated is the idea that inertial frames can only be defined with respect to other matter sources⁵. They consider the gravitational action

$$S_{BD} = \int d^4x \sqrt{-g} \left(\phi R - \frac{\omega}{\phi} (\partial_\mu \phi \partial^\mu \phi) + \mathcal{L}_m \right), \quad (1.11)$$

where ϕ is a dynamical scalar field, ω is a constant and \mathcal{L}_m is the *matter Lagrangian density* (the matter Lagrangian density is related to the matter Lagrangian via $L_m \equiv \sqrt{-g} \mathcal{L}_m$). The value of the scalar field can be thought of as setting the local value of the Newton constant: $\phi \sim c^4/(16\pi G)$. Thus in some sense ϕ locally determines the strength of the gravitational field.

Lovelock and Horndeski simply considered the most general kinds of theories one could write that have second order equations of motion given certain constraints: Lovelock only considered theories that could involve derivatives of the metric field $g_{\mu\nu}$ in the equations of motion, while Horndeski (Lovelock's graduate student) allowed for derivatives of a scalar field ϕ as well. Considering only second order equations of motion can be motivated as the most general class of theories that *may* admit sensible quantization (for further discussion we refer the reader to [Woo15]; see also Sec. 1.4.1).

While EdGB gravity can be written as a Horndeski theory, this was not known until some time after it was introduced [KYY11], and it has interesting enough fea-

⁵Mach's principle has an interesting history. It influenced Einstein when he constructed GR, although his theory is ultimately not compatible with Mach's principle. The principle has inspired other theories as well, such as "Einstein-Cartan-Sciama" gravity; see e.g. [Sci53]. We should qualify this discussion by stating that it is not entirely clear what Mach's principle exactly is; various authors have interpreted Mach's original thought experiment differently over time. We refer the reader to Hawking and Ellis for further discussion of this highly influential, if nebulous, principle [HE75].

tures (such as admitting scalarized black hole solutions, e.g. [SZ14b]) that we place it separately from the Horndeski theories in Table (1.1). The general form of actions we will consider in this thesis for this theory are

$$S_{EdGB} = \int d^4x \sqrt{-g} (R - (\partial\phi)^2 - V(\phi) - W(\phi)\mathcal{G}), \quad (1.12)$$

where V and W are as-yet unspecified functions of the scalar (“dilaton”) field ϕ and \mathcal{G} is the (four dimensional) Gauss-Bonnet scalar:

$$\mathcal{G} \equiv R^2 - 4R_{\mu\nu}R^{\mu\nu} + R_{\mu\alpha\nu\beta}R^{\mu\alpha\nu\beta}. \quad (1.13)$$

1.3 Motivations for studying modified gravity

1.3.1 Finding a complete theory of quantum gravity

It has long been known that GR is nonrenormalizable (for an introductory discussion, see e.g. [Sho07]), which indicates that GR is most likely not a complete quantum theory of gravity⁶. Currently, the main two main theoretical frameworks considered by most researchers in quantum gravity are string theory (see e.g. [Pol98]) and loop quantum gravity (see e.g. [Rov98]). In their respective low energy limits, both theories appear to modify general relativity by adding new fields and curvature couplings; both of these theories have been frequently invoked to justify various modified gravity theories over the last few decades.

1.3.2 Determining dynamics of the early universe

To current observational precision the large scale structure of the universe is well described by a Friedman-Robertson-Lemaître-Walker (FLRW) cosmology [A+18]. What

⁶Although if GR is “asymptotically safe” perhaps the theory will not need to be modified to make it compatible with quantum mechanics; see e.g. [Eic19] and references therein. We should also note that there is no issue with quantizing GR as long as one treats it as an effective field theory; see e.g. [Bur04] and references therein.

is most relevant to this discussion is that the universe is expanding, and all observations suggest it has been expanding since the “big bang”, a point where the universe had essentially “zero size”. More precisely: the FLRW cosmologies are geodesically incomplete (see e.g. [HE75]), and their $t = 0$ “boundary” sets the initial conditions for the expansion of the universe (the big bang). While the FLRW cosmologies (with the addition of a cosmological constant, radiation, and matter, including a larger amount of “dark matter”) fits cosmological observations to their current precision, we lack a good theory to explain why the universe began with FLRW-like initial conditions. The basic question that models of the “very early universe” attempt to address is:

- What physical mechanism sets the homogeneous, flat, isotropic, initial conditions at (or before) the big bang that subsequently led to FLRW expansion?

Most attempts to address this question with a classical field theory have required the introduction of additional fundamental fields, and/or modifications of GR. The initial singularity/incompleteness of the FLRW solutions are not censored by a horizon, so it is in principle possible to probe pre-FLRW expansion physics. At the moment though any pre-FLRW physics is not directly observable as the cosmic microwave background (our current best developed observable of early universe physics) was opaque to electromagnetic radiation in the very early universe (see e.g. [Muk05]); with the CMB we can essentially only directly see the physics near and after the point radiation decoupled from baryonic matter (i.e. the “era of recombination”). Observing gravitational radiation from the very early universe may allow for observing physics at times much closer to the big bang than is currently possible from observations of the cosmic microwave background⁷, although gravitational wave detectors of sufficient precision to measure those effects do not (or at least do not yet) exist.

From the incompleteness theorems [HE75], resolving the incompleteness of the big bang using classical fields within GR requires violating the Null Convergence

⁷These gravitational waves may be indirectly observable in the cosmic microwave background through study of its polarization.

Condition (NCC). This condition sets all contractions of the spacetime Ricci tensor with two null vectors to be positive semidefinite

$$R_{\mu\nu}k^\mu k^\nu \geq 0. \tag{1.14}$$

Many (if not most) attempts to modify the NCC with a classical field theory of gravity have required modifying GR. For example, recently many researchers have used Horndeski theories of gravity (e.g. [CNT10, IS17]) to violate the NCC.

1.3.3 Determining dynamics of the late universe

An enormous amount of effort has been expended over the last three decades to model the cosmological and astrophysical observations of dark matter and dark energy, which appear to dominate cosmological dynamics in the late universe⁸.

Observational astronomical evidence for the existence of dark matter, which is a presumably non-baryonic source of gravitation that clumps together at galactic scales, has been growing since at least the 1950's. Cosmological observations of baryonic acoustic oscillations in large scale structure surveys and of the precise structure of the acoustic peaks in the cosmic microwave background have provided additional strong evidence for the existence of dark matter (a fairly accessible and broad overview of these observations can be found in [Roo10]). While it is widely expected that dark matter is indeed a form of *matter*, it is striking that the only observational evidence for dark matter is through measurements of its gravitational effects. This has prompted efforts to model dark matter by modifying GR. Only additional, more accurate measurements of the gravitational effects of dark matter, or the detection of the putative dark matter particle may lead to a resolution of this problem in basic physics. For a review of some of these issues related to particle dark matter detection see e.g. [Lis17].

⁸Dark matter begins to play an important role once the universe enters the matter domination stage, while the cosmological constant appears to only very recently be important in cosmological evolution.

While dark matter remains unexplained, there is a well known, simple, minimal, and (at least for now) accurate approach to model dark energy: simply add a “cosmological constant” term, Λ , to the Einstein equations

$$G_{\mu\nu} + \Lambda g_{\mu\nu} = T_{\mu\nu}, \tag{1.15}$$

and then pick Λ to match the observed late time cosmological expansion. Many researchers in theoretical physics find this solution unsatisfactory, even though it *does* match all observations to their present accuracy and precision, and it requires no additional dynamical fields. A commonly invoked line of reasoning for why adding a cosmological constant term is not a satisfactory explanation for the observed late-time acceleration of the universe is that in order to properly fit the data one needs a Λ that is very small with respect to the Planck length⁹ $l_p = \sqrt{\hbar G/c^3} \approx 10^{-35}m$: i.e. one needs $l_p^2 \Lambda \sim 10^{-122} \ll 1$ to properly fit the cosmological expansion data. The Planck length is the natural length scale that appears from the fundamental constants of gravity (G), special relativity (c), and quantum mechanics (\hbar). From effective field theory reasoning one would expect a relativistic quantum theory of gravity to involve dimensionless quantities such as Λl_p^2 to be of order unity. We note that anthropic arguments [Wei89] led Weinberg to “predict” a value of the cosmological constant that was very close to its presently observed value, although the validity of anthropic reasoning remains controversial. We will not describe the arguments that have gone into obtaining a cosmological constant that *naturally* (in the sense of effective field theory; see e.g. [Bur15]) results in the very small observed cosmological constant, except to say that one avenue of research in that program has been to modify gravity at cosmological scales.

⁹ \hbar is the reduced Planck constant; we deviate from geometric units only here.

1.3.4 Interior of black holes

From the incompleteness theorems [HE75], the interior of black hole solutions in GR must be geodesically incomplete, provided the NCC holds. If cosmic censorship holds, any problems due to incomplete solutions in black hole solutions will be inside their event horizons (the “interior” of the black hole). As in early universe cosmology, eliminating the interior black hole incompleteness/singularity requires modifying GR (or invoking quantum effects); see e.g. [MM01, Mat05] for some relatively recent suggestions that have attracted attention. Unlike in cosmology, unfortunately many of these proposed solutions lack a concrete mathematical formulation. We should note that while understanding the interior of black holes remains an interesting problem in mathematical and theoretical physics, as classical black hole interiors are by definition outside of causal contact with the outside world, it may be end up being impossible to gain observational information of the nature of black hole interiors.

1.3.5 Understanding complexity of solutions to partial differential equations of classical physics

It is by now well-understood that many of the simple, deterministic equations of classical physics can have enormously complex solutions [GK99]. As just one example, the Euler equations, which describe the dynamics of a perfect fluid

$$\frac{\partial v^i}{\partial t} + v^j \partial_j v^i = 0, \tag{1.16}$$

can describe such complex behavior such as turbulent fluid flow [FK95]. Here v^i is the local fluid velocity at the point (t, x^j) (the *Eulerian* specification of fluid flow).

By contrast, the Einstein equations of GR form a much more complex system of equations than the equations of Newtonian mechanics or fluid dynamics. This being said, the known physical systems where gravity is the dominant force (the regions around black holes, and the large scale dynamics of observable universe) can be described with remarkably simple solutions to the theory.

The final state conjecture roughly speaking is that the generic asymptotic (in time) solution to the Einstein equations with asymptotically flat initial data is the formation of a black hole or Minkowski spacetime (for a review see [Col19]). Moreover this end state black hole solution is conjectured to generically be the Kerr solution,¹⁰ see e.g. [IK15]. The difficulty in assigning a degree of complexity to black hole solutions even when including leading order quantum effects, (beyond the still mysterious Bekenstein entropy and Hawking radiation), remains an interesting direction for research in quantum gravity today.

One goal of modified gravity research has been to find gravitational theories that admit more complicated black hole solutions than the three-parameter Kerr-Newman black hole solutions. This research program often goes under the name of finding “black hole hair”. For a review on finding modified gravity theories that admit scalarized black hole solution see [HR14].

At least some classes of EdGB gravity theories admit stable scalarized black hole solutions (a non-exhaustive list of publications that touch upon this fact is [KMR⁺96, SZ14a]). This has been part of the reason why this theory has attracted so much recent attention. We should note though that the kind of scalarized black hole solutions found in EdGB gravity are still fairly “simple” solutions, in that they at best only allow one more free parameter in the solution family, and often times the scalar field profile is completely set by the black hole mass, so the black hole solution in some fundamental sense is no more complicated than the Kerr-Newman family of solutions.

1.3.6 Testing general relativity in the strong-field, dynamical regime

Measuring the gravitational waves emitted from the inspiral, merger, and ringdown of two black holes (or of two very compact objects which merge to form a black hole)

¹⁰If there is net electric charge in the initial data then the generic black hole solution would be the Kerr-Newman solution.

provides an exciting opportunity to study GR in the *strong field, dynamical regime* (see, e.g. [A⁺16b, YYP16, A⁺16a]). This gravitational regime, where dynamics are near the speed of light and gravitational potentials $Gm/(c^2r) \sim 1$, have until the recent discoveries of the LIGO/Virgo gravitational wave detections, been unexplored. Gravitational wave astrophysics offers a novel opportunity to determine the regime of validity of GR, which as discussed above may need to be subsumed by another theory of gravity to properly describe astrophysical and cosmological observations. As gravitational waves are extremely weak, but are coherent over a single inspiral, merger, and ringdown event, matched filtering has become the dominant procedure to extract signal from noise in the LIGO/Virgo gravitational wave detectors (for a review see e.g. [Mag08]). Matched filtering requires the construction of accurate templates, or predictions, of gravitational waves from a given theory. In order to make full use of gravitational wave observations to test GR thus requires deriving detailed predictions of gravitational waves in modified gravity theories in the strong field, dynamical regime.

Some of the original motivation to undertake the projects described in this thesis came from the desire to make gravitational wave templates in a modified gravity theory.

1.4 Modified gravity theories must admit a mathematically consistent interpretation

Any modification of GR must admit a mathematically consistent interpretation. In this section we outline several different ways to make mathematical sense of modified gravity theories.

1.4.1 Quantizability

By “quantizability”, we mean that the equations of motion for the theory in question must admit a sensible quantum mechanical interpretation. For our purposes, the main obstruction to obtaining a modified gravity theory that admits a sensible quantum version is that its equations of motion should be at most second order in time. If the equations of motion for the theory have higher order derivatives in time, then the Hamiltonian for the theory is unbounded from above and below, and the theory is said to be *Ostrogradsky unstable*¹¹; for a review see [Woo15]. To see this (here we follow [Woo15]), we consider Lagrangians in 1 + 0 dimensions for a field f (adding spatial dimensions and more fields, provided they do not add new constraints to the system, does not change the basic argument):

$$L \left(f, \frac{df}{dt}, \dots, \frac{d^N f}{dt^N} \right). \quad (1.17)$$

Varying f the equation of motion is

$$\sum_{i=0}^N \left(-\frac{d}{dt} \right)^i \frac{\partial L}{\partial (d^i x/dt^i)} = 0. \quad (1.18)$$

We want to define canonical positions and momenta $\{Q_i, P_i\}$ so that we can define a Hamiltonian via a Legendre transformation of the Lagrangian

$$H = \sum_i Q_i P_i - L, \quad (1.19)$$

and so that the equations of motion (1.18) can be rewritten in canonical form

$$\frac{dQ_i}{dt} = \frac{\partial H}{\partial P_i}, \quad (1.20a)$$

$$\frac{dP_i}{dt} = -\frac{\partial H}{\partial Q_i}. \quad (1.20b)$$

In order to achieve this, following Ostrogradsky we define

$$Q_i \equiv \frac{d^{i-1} f}{dt^{i-1}}, \quad (1.21a)$$

¹¹This is not always true if the theory has carefully chosen “constraint”; see [CFLT13]

$$P_i \equiv \sum_{j=i}^N \left(-\frac{d}{dt} \right)^{j-i} \frac{\partial L}{\partial (d^j f / dt^j)}. \quad (1.21b)$$

In order for the Legendre transformation to be well defined, we require that the Lagrangian be *nondegenerate*, is that there exists a function $\mathcal{A}(Q_1, \dots, Q_N, P_N)$ such that

$$\frac{\partial L}{\partial (d^N f / dt^N)} = P_N. \quad (1.22)$$

The Hamiltonian then equals

$$\begin{aligned} H &= P_1 \frac{df}{dt} + P_2 \frac{d^2 f}{dt^2} + \dots + P_N \mathcal{A} - L \\ &= P_1 Q_2 + P_2 Q_3 + \dots + P_N \mathcal{A} - L. \end{aligned} \quad (1.23)$$

We see that terms like $P_1 Q_2$ are unbounded from below and above provided $P_1 \neq 0, Q_2 \neq 0$. The terms like $P_1 Q_2$ cannot be cancelled off by the terms like $P_N \mathcal{A}$ or L as they are only functions of $\{Q_i, P_N\}$. Notice that not only is (1.23) unbounded from above and below, the Hamiltonian does not even any local minimums in the field direction $P_1, \dots, P_{N-1}, Q_2, \dots, Q_{N-1}$. It is not entirely settled what this means for the classical dynamics of higher derivative theories, but quantum mechanically an unbounded Hamiltonian most likely spells disaster. This is because one could conserve energy by moving down the energy potential of (1.23) while producing more and more positive energy particles—for example one could evolve arbitrarily quickly to a state moving in the direction $P_1 \rightarrow +\infty, Q_2 \rightarrow -\infty, P_2 \rightarrow \infty, Q_3 \rightarrow \infty$ while conserving the Hamiltonian. We refer the reader to [Woo15] for further discussion of the Ostrogradsky instability.

1.4.2 Well-posed initial value problem

General definition

In addition to being quantizable, a theory must also admit mathematically sensible classical solutions, and for us this criteria will mean the theory must have a well-posed

initial value problem. We only consider initial value problems as this conforms with the general sentiment that with the laws of physics we should be able to predict the future knowing only the present. A system of partial differential equations in general has a well-posed initial value problem if (see e.g. [Eva10])

1. The problem has a solution
2. The solution is unique
3. The solution depends continuously on the (initial, and potentially boundary) data for the problem

The last criteria is somewhat subtle, as what “continuous” means depends on the function space one works in. A theory may have a well-posed initial value problem with respect to one function space but not another. For the purpose of the discussion we will use standard notions of continuity related to the Sobolev space H_0^2 , and we will say a theory has a well posed initial value problem if it has a strongly hyperbolic formulation¹².

Strong hyperbolicity

See for example [KL89] or [ST12] for further discussion on hyperbolicity. We first define the *principal symbol* of a system of partial differential equations. Consider a system of first order partial differential equations:

$$\mathcal{E}_A(v_B, \partial_a v_B) = 0, \tag{1.24}$$

here A labels the system of equations and fields, and a labels the coordinates (we assume the number of equations equals the number of unknowns). Essentially any system of PDE can be written in first order form through field redefinitions so do

¹² H_0^2 is the space of all functions that have weak partial derivatives of at least second order that are contained in L^k .

sacrifice any generality with the above assumptions. The principal symbol is defined to be

$$\mathcal{P}_A^B(\xi_c) \equiv \frac{\delta \mathcal{E}_A}{\delta(\partial_c v_B)} \xi_c. \quad (1.25)$$

The system (1.24) is *strongly hyperbolic* (which again, for our purposes is synonymous with the theory having a well posed initial value problem) if there are a complete set of ξ_c which satisfy the *characteristic equation*

$$\det [\mathcal{P}_A^B(\xi_c)] = 0. \quad (1.26)$$

We will further discuss the physical interpretation of the characteristic covectors in Chapter 2.

General Relativity

There is some subtlety to defining the initial value problem for GR due to the gauge invariance of the equations of motion. In fact the theory does not not admit a well-posed initial value problem for any choice of gauge; we refer the reader to the review [ST12] (see also [Wal84]) for more discussion. Choquet-Bruhat first found a gauge (harmonic gauge) for which the theory does admit a well-posed initial value problem [CB08]. As will be detailed in the later chapters, *strongly hyperbolic* systems admit well posed initial value problems, and we will consider whether or when EdGB admits a strongly hyperbolic formulation.

Modified gravity theories

Systematic studies of the initial value problem for modified gravity theories that involve a dynamical scalar field (such as EdGB) gravity have only recently been undertaken; see e.g. [PR17, Pap17, Kov19, KR20a, KR20b] for recent work on this problem. We will discuss the initial value problem for EdGB gravity in more depth in this thesis in later chapters.

1.4.3 Quantizability and having a well-posed initial value problem are not equivalent

A theory may admit a well-posed initial value problem (in terms of it being strongly hyperbolic), but it may still not admit a sensible quantization by being Ostrogradsky unstable. An interesting example of this is quadratic gravity [Noa83]:

$$S_{QG} = \int d^4x \sqrt{-g} (R + \alpha R^2 + \beta R_{\mu\nu} R^{\mu\nu}). \quad (1.27)$$

This theory has equations of motion that have four derivatives in time: the theory is Ostrogradsky unstable. Nevertheless the theory does have a well posed initial value problem, although it appears that the initial value problem depends on some of the initial data being *analytic* (in the complex variables sense), which is too restrictive a condition for the initial data of a physical theory.

For a simpler (and perhaps more convincing) example to illustrate the difference between quantizability¹³ and well-posedness of the initial value problem, we consider the toy model

$$S = \int d^4x \sqrt{-g} ((\square\phi)^2 - V(\phi)). \quad (1.28)$$

This theory is higher derivative in time, and with no obvious symmetry to reduce number of degrees of freedom it is Ostrogradsky unstable. We explicitly show this by constructing its Hamiltonian. We define

$$Q_1 \equiv \phi, \quad (1.29a)$$

$$Q_2 \equiv \partial_t \phi, \quad (1.29b)$$

$$\begin{aligned} P_1 &\equiv \frac{\partial L}{\partial(\partial_t \phi)} - \frac{\partial}{\partial t} \left(\frac{\partial L}{\partial(\partial_t^2 \phi)} \right) \\ &= -2\partial_t^3 \phi, \end{aligned} \quad (1.29c)$$

$$P_2 \equiv \frac{\partial L}{\partial(\partial_t^2 \phi)}$$

¹³Which recall for our purposes is Ostrogradsky stability.

$$= \partial_t^2 \phi. \tag{1.29d}$$

The Hamiltonian is

$$\begin{aligned} H &\equiv P_1 \partial_t \phi + P_2 \partial_t^2 \phi - L \\ &= P_1 Q_2 + P_2^2 - (-P_2^2 + \Delta Q_1)^2 + V(Q_1). \end{aligned} \tag{1.30}$$

We see the appearance of a $P_1 Q_2$ term, so the Hamiltonian is unbounded from above and below, and presumably does not admit a sensible quantization.

The equations of motion for (1.28) are

$$-\square \square \phi - V'(\phi) = 0. \tag{1.31}$$

If we define $\psi \equiv \square \phi$ we have a strongly hyperbolic system of equations

$$-\square \psi - V'(\phi) = 0, \tag{1.32a}$$

$$\square \phi - \psi = 0, \tag{1.32b}$$

so the theory admits a well-posed initial value problem. Unfortunately there is not much rigorous work on the classical dynamics of Ostrogradsky unstable theories.

1.4.4 Linear stability and having a well-posed initial value problem are not equivalent

Finding the linear stability of a solution involves finding the equations of motion of linear perturbations about a (non)linear solution, and determining if the solutions grow (typically exponentially) or not. Determining if a theory has a well-posed initial value problem consists in determining if the theory has a unique solution, and that the theory has a strongly hyperbolic formulation (see Sec. 1.4.2).

As an example to demonstrate the difference between linear stability and hyperbolicity, we consider the following toy model equations of motion

$$(- (1 - \phi^2) \partial_t^2 + \partial_x^2) \phi - V(\phi) = 0. \tag{1.33}$$

The equations of motion for linear perturbations about a $\phi = \phi_0$ solution are

$$(- (1 - \phi_0^2) \partial_t^2 + \partial_x^2) \phi - V'(\phi_0)\phi = 0. \quad (1.34)$$

Looking for mode solutions of the form $e^{i\omega t - ikx}$, we see that

$$((1 - \phi_0^2) \omega^2 - k^2) \phi - V'(\phi_0)\phi = 0. \quad (1.35)$$

Typically it is said the background is “stable” if there are no $\omega^2 < 0$ solutions, as then the evolution would be of the form $e^{\pm\omega t}$ like solutions: the system would *evolve* exponentially fast away from the background solution. The principal symbol is essentially the “ $\omega, k \rightarrow \infty$ ” version of this equation:

$$\mathcal{P} = (- (1 - \phi_0^2) \xi_t^2 + \xi_x^2). \quad (1.36)$$

We see that in a hyperbolicity analysis we only look at the highest order terms in derivatives. The theory is strongly hyperbolic if $|\phi_0| < 1$: if $|\phi_0| > 1$ the theory lacks well-posed initial value problem. There is no meaningful way to say a background with $|\phi_0| > 1$ is unstable, as instability implies that the solution will presumably *evolve* to a new solution state. If the problem has an ill posed initial value problem though, it does not make sense to talk of the system evolving in time: in the model chase shown here for $|\phi_0| > 1$ it makes more sense to solve the system as a boundary value problem (the problem becomes elliptic; for further discussion of a very similar model equation see [\[Mor82\]](#)).

The main point that is if the theory was merely unstable, there would then be a maximum rate of growth independent of the details of the initial data. If we set $\phi_0 = 0$, we see from the linear stability analysis that

$$\omega = \pm (k^2 + V'(0))^{1/2}. \quad (1.37)$$

If the background is unstable, the maximum rate of growth is set to be $(V'(0))^{1/2}$ (which has units of $1/\text{times}$). Meanwhile, consider $\phi_0 = 2$. We then have

$$\omega = \pm (-k^2 + V'(-2))^{1/2}. \quad (1.38)$$

The rate of growth can be unbounded, provided there are high enough k modes in the initial data¹⁴. Sometimes in the cosmology literature failure of hyperbolicity is called a “gradient instability”, but as we see this nomenclature is misleading (for further discussion, see e.g. [PR15]).

1.5 Higher derivative theories, effective field theory (EFT), and order reduction

While we do not consider an EFT treatment of EdGB gravity (instead we directly solve the equations of motion of EdGB gravity as-is), we briefly review the EFT approach to contrast it with the approach taken in this thesis.

The formalism of effective field theory provides a well-motivated way to interpret higher derivative theories (see e.g. [Bur04]). In the effective field theory interpretation of a field theory, we assume that we are not dealing with a mathematically consistent field theory, but instead are dealing with some low-energy truncated version of a well-defined theory. The claim is that one can consider corrections to the background dynamics of the theory order by order in some small coupling parameter, such as the background energy of the process being considered. The background dynamics are driven by the lowest energy terms in the theory, which typically constitute a well-defined field theory in themselves.

The main subtlety in the EFT approach is that to each higher order in perturbation theory, we need to include all terms in the equations of motion that are consistent with the symmetries of the (potentially unknown) “complete theory” we are approximating. Computing to a higher order in perturbation theory requires potentially adding a large number of new terms. Additionally we must keep in mind that the solutions to an effective field theory typically do not “approach” the *exact* solutions

¹⁴Consider that functions of compact support in real space cannot have compact support in momentum space.

(if exact solution exist) to any given truncation of the EFT.

As a simple example to explain some of this reasoning, we consider the following toy model

$$\epsilon a_2 \frac{d^2 x}{dt^2} + a_1 \frac{dx}{dt} + a_0 x = 0. \quad (1.39)$$

Here we consider the a_2 term as the leading order EFT correction to the equations of motion $a_1 dx/dt + a_0 x = 0$, and $\epsilon \ll 1$ is a dimensionless number. From the EFT perspective then, we would interpret Eq. (1.39) as containing the leading order corrections to the background theory $a_1 dx/dx + a_0 x = 0$, truncated to order ϵ . The full solution to this truncation is given by

$$x = c_+ \exp \left[\frac{i}{2\epsilon a_2} \left(ia_1 + \sqrt{4\epsilon a_2 a_0 - a_1^2} \right) t \right] + c_- \exp \left[\frac{i}{2\epsilon a_2} \left(ia_1 - \sqrt{4\epsilon a_2 a_0 - a_1^2} \right) t \right], \quad (1.40)$$

where the constants c_{\pm} are set by the initial data. As $\epsilon \rightarrow 0$, the solution approaches

$$x = c_+ \exp \left[-\frac{a_1}{\epsilon a_2} t \right] + c_- \exp \left[-\frac{a_0}{a_1} t \right] + \dots. \quad (1.41)$$

We see there is a term that decays exponentially with timescale ϵ (provided $a_1/a_2 > 0$, which we will assume is the case). This term is *nonperturbative* in ϵ —there is no Taylor series expansion of functions like $e^{-1/\epsilon}$. To solve the truncation Eq. (1.39) in an order reduction approach, we solve it order by order in ϵ :

$$x = x_0 + \epsilon x_1 + \dots. \quad (1.42)$$

An expansion of this form will clearly never give us terms that are nonperturbative in ϵ . If we want to interpret Eq. (1.39) as an EFT though, then we shouldn't take exact solutions like Eq. (1.40) very seriously, as in effective field theory corrections to the equations of motion should *not* add new integration constants (degrees of freedom), but only slightly change the background solution by terms perturbative in the corrections.

As a more involved example, we return to quadratic gravity, Eq. (1.27), but now interpret it as containing the leading order terms in an effective field theory of some “complete” gravity theory. We consider a solution of the form

$$g_{\mu\nu} = g_{\mu\nu}^{(0)} + \epsilon g_{\mu\nu}^{(1)} + \epsilon^2 g_{\mu\nu}^{(2)} + \dots, \quad (1.43)$$

where ϵ is a small coupling parameter. We consider α and β to be of order ϵ , and find solutions order by order in ϵ . That is, the “background” term $g_{\mu\nu}^{(0)}$ is determined by the Einstein equations, which have a well-posed initial value problem. As mentioned earlier this is the order reduction approach to solving the equations of motion; although we note that the order reduction of the equations of motion is conceptually distinct from the EFT interpretation of the equations of motion. The equation of motion to order ϵ is of the form

$$G_{\mu\nu}^{(1)} = \mathcal{S} [g_{\mu\nu}^{(0)}], \quad (1.44)$$

where \mathcal{S} depends on the higher derivative terms that are proportional to α and β , and $G_{\mu\nu}^{(1)}$ is the Einstein tensor evaluated to order ϵ . To go to ϵ^2 , we should include higher order terms in the equations of motion; that is we should consider an action of the form

$$S = \int d^4x \sqrt{-g} (R + \alpha R^2 + \beta R_{\mu\nu} R^{\mu\nu} + \gamma R^3 + \rho R_{\alpha\mu\beta\nu} R^{\alpha\mu}{}_{\gamma\kappa} R^{\gamma\kappa\beta\nu} + \dots), \quad (1.45)$$

where γ and ρ are constants (we have not written all possible new terms). We caution that if we consider deviations to *vacuum* solutions to the Einstein equations, then $R = R_{\mu\nu} = 0$ and in fact we only begin to see nontrivial corrections at $\mathcal{O}(R^3)$ in the action; see [EGHS17]. Thus more properly in this example we should have included a matter term in the action, and considered potential EFT deviations from that matter model as well.

The main point we want to draw from this discussion is that simply writing down the equations of motion for a (modified gravity) theory is not enough—the kinds of solutions one obtains from the theory depends on whether one treats it as an effective

field theory or as a complete, self-contained theory. For further discussion of the order reduction approach to a higher derivative modified gravity theory, including a discussion of other issues related to this approach, see [OSSH17, AL19].

1.6 EdGB gravity

1.6.1 The model

We return to EdGB gravity, Eq. (1.12), which we repeat here for convenience:

$$S_{EdGB} = \int d^4x \sqrt{-g} (R - (\partial\phi)^2 - V(\phi) - W(\phi)\mathcal{G}). \quad (1.46)$$

This class of theories is interesting as, at least for certain choices of V and W , they admit scalarized black hole solutions so these theories may produce gravitational (and scalar) wave signatures that greatly differ from the predictions of GR for binary black hole inspiral. Being a representative member of the Horndeski class of scalar-tensor theories, the study of this theory may shed interesting light on the nonlinear dynamics of other Horndeski theories (although more work will be necessary to determine if that is in fact the case).

In Chapters 2 and 3 we study the nonlinear dynamics of this theory with

$$V(\phi) = 0, \quad (1.47a)$$

$$W(\phi) = \lambda\phi, \quad (1.47b)$$

where λ is a constant. This form of the EdGB gravity is invariant under shifts $\phi \rightarrow \phi + const.$ as the Gauss-Bonnet scalar \mathcal{G} is locally a total derivative in four dimensional spaces. This theory may be motivated as containing the leading order shift symmetric terms of an effective field theory have has a scalar degree of freedom.

In Chapter 4 we study

$$V(\phi) = \mu^2\phi^2 + 2\lambda\phi^4, \quad (1.48a)$$

$$W(\phi) = \frac{1}{4}\eta\phi^2, \tag{1.48b}$$

where μ, λ, η are constants. This theory is invariant under $\phi \rightarrow -\phi$ (“ \mathbb{Z}_2 ” symmetry). This theory contains some (but not all; see e.g. [KMR⁺96, MSB⁺19, KR20b]) of the leading order scalar field terms that are invariant under this symmetry.

1.6.2 Method of study: spherically symmetric dynamics

In this thesis we exclusively concerned with the dynamics of EdGB gravity in 1 + 3 dimensional spherically symmetric spacetimes. In those spacetimes the metric can be written in full generality as

$$ds^2 = \alpha_{ab}du^a du^b + r^2 (d\theta^2 + \sin^2\theta d\phi^2), \tag{1.49}$$

where α_{ab} is some as-yet unspecified two dimensional Lorentzian metric. We provide a more complete discussion of spherically symmetric spacetimes in Appendix A.

Ultimately researchers would like to compare the predictions modified gravity theories such as EdGB gravity in binary black hole setups; those solutions are fairly far away from spherical symmetry. There are two main reasons to initiate studying the nonlinear dynamics of this theory in spherical symmetry, as opposed to going directly to trying to solve the full problem in a symmetry unconstrained spacetime. The first reason is simply because it is easier to write, debug, and run codes in spherical symmetry than for general 1 + 3 dimensional evolution, so spherical symmetry is a good test group to begin exploring how to solve for the dynamics of these kinds of theories. The second (related) reason is that the initial value problem for EdGB gravity (and the other Horndeski theories) is still fairly poorly understood, especially in comparison to General Relativity and the fluid (Euler and Navier Stokes) equations. There is much more purely gauge freedom in full 1 + 3 dimensional evolution that may cloud any insights that one may gain on the initial value problem for the theory, and understanding at least the broad features of the initial value problem of EdGB gravity is essential before complete 1 + 3 evolution in the theory should be attempted.

It may now be possible to extend our results to studying the full dynamics of EdGB gravity about more generic backgrounds with the recent formulation of a new gauge condition by Kovacs and Reall [[KR20a](#), [KR20b](#)]. It was recently shown by those authors that EdGB gravity, and more generally the Horndeski theories, have a well-posed initial value formulation in a class of “modified harmonic” gauges for spacetimes where the Gauss-Bonnet corrections are “small” enough. We leave discussion of this and other future directions to the Concluding remarks, [Sec. 5](#).

Chapter 2

Dilaton field dynamics during spherical collapse in EdGB gravity with linear Gauss-Bonnet coupling

Here we discuss a series of numerical studies on the nonlinear dynamics of EdGB gravity with a linear Gauss-Bonnet coupling, in two different coordinate systems. This chapter is largely adapted from (and hopefully improves some of the discussion and presentation of) the publications [RP19a] and [RP19b], which we coauthored with Frans Pretorius.

2.1 Basic equations

2.1.1 Linearly coupled EdGB gravity

We consider the following EdGB action

$$S = \frac{1}{2} \int d^4x \sqrt{-g} (R - (\nabla\phi)^2 + 2\lambda\phi\mathcal{G}). \quad (2.1)$$

Where (as is discussed in the Introduction) \mathcal{G} is the Gauss-Bonnet scalar. Varying (2.1) in turn with respect to the metric $g^{\mu\nu}$ and scalar ϕ gives

$$R_{\mu\nu} - \frac{1}{2}g_{\mu\nu}R + 2\lambda\delta_{\alpha\beta\rho\sigma}^{\gamma\delta\kappa\lambda}R^{\rho\sigma}{}_{\kappa\lambda}(\nabla^\alpha\nabla_\gamma\phi)\delta^\beta_{(\mu}g_{\nu)\delta} - T_{\mu\nu} = 0, \quad (2.2a)$$

$$\square\phi + \lambda\mathcal{G} = 0, \quad (2.2b)$$

where

$$T_{\mu\nu} \equiv \nabla_\mu\phi\nabla_\nu\phi - \frac{1}{2}g_{\mu\nu}(\nabla\phi)^2. \quad (2.3)$$

2.1.2 Polar coordinates

For this study, we used the line element (“polar coordinates”)

$$ds^2 = -e^{2A(t,r)}dt^2 + e^{2B(t,r)}dr^2 + r^2(d\vartheta^2 + \sin^2\vartheta d\varphi^2). \quad (2.4)$$

Defining the variables

$$Q(t, r) \equiv \partial_r\phi, \quad (2.5a)$$

$$P(t, r) \equiv e^{-A+B}\partial_t\phi, \quad (2.5b)$$

and taking appropriate algebraic combinations of the non-trivial components of Eq. (2.2a) and of Eq. (2.2b) results in the following system of PDEs:

$$\begin{aligned} & \left(\mathcal{I}^2 - 32\lambda^2\mathcal{B}^2 + 128\lambda^2e^{-2B}\mathcal{B} \left(1 - 2\lambda(3e^{-2B} + 1)\frac{Q}{r} \right) \frac{\partial_r B}{r} \right. \\ & \left. + 256\lambda^3\mathcal{B}^2(e^{-2B}\partial_r Q - e^{-B}rP\mathcal{K}) \right) \partial_r A \\ & + 4\lambda e^{-3B}\mathcal{B}(128\lambda^2e^{2B}r\mathcal{B}P\mathcal{K} - 4\lambda e^B P^2 + e^B(re^{2B} - 12\lambda Q)Q) \partial_r B \\ & - 512\lambda^3 r e^{-B}\mathcal{B}^2\mathcal{K}\partial_r P - 4\lambda r\mathcal{B}\mathcal{I}\partial_r Q \\ & - \frac{r\mathcal{B}}{2}(e^{2B} + 128\lambda^2\mathcal{K}^2) + 4\lambda\mathcal{B}(-1 + 128\lambda^2\mathcal{K}^2)Q + 2\lambda e^{-2B}Q^3 \\ & + \left(64\lambda^2e^{-2B}r\mathcal{B} - 16r^3\lambda^2\mathcal{B}^2 - \frac{r^3}{4} \right) \left(\frac{Q}{r} \right)^2 \\ & + 4\lambda r^2 e^B P\mathcal{I}\mathcal{B}\mathcal{K} + \left(16\lambda^2 r\mathcal{B}^2 - \frac{r}{4}\mathcal{I} \right) P^2 = 0, \end{aligned} \quad (2.6a)$$

$$\begin{aligned} & \left(1 + 4\lambda(1 - 3e^{-2B})\frac{Q}{r}\right)\partial_r B - \frac{r}{4}(Q^2 + P^2) - \frac{1 - e^{2B}}{2r} \\ & + 4\lambda r \mathcal{B}(-\partial_r Q + re^B P \mathcal{K}) = 0, \end{aligned} \quad (2.6b)$$

$$\partial_t Q - \partial_r(e^{A-B}P) = 0, \quad (2.6c)$$

$$\begin{aligned} & \left(\mathcal{I} + 64\lambda^2 e^{-2B} \mathcal{B} \frac{\partial_r B}{r}\right)\partial_t P - \left(\mathcal{I} - 64\lambda^2 e^{-2B} \mathcal{B} \frac{\partial_r A}{r}\right)\frac{1}{r^2}\partial_r(r^2 e^{A-B}Q) \\ & + 16\lambda e^{A-B} \mathcal{I} \left(\frac{\partial_r A}{r} \frac{\partial_r B}{r} - \mathcal{K}^2\right) \\ & + 4\lambda e^{A-B} \mathcal{B} \left((P^2 - Q^2) + 32\lambda r Q \mathcal{K}^2 - 16\lambda e^{-2B} \frac{Q}{r} (\partial_r A)^2\right) \\ & + 16\lambda e^{-B} ((\partial_r B - \partial_r A)P - 2\partial_r P) \mathcal{K} \\ & + 2\frac{\partial_r B}{r} + 2\left(-1 - 16\lambda e^{-2B} \frac{Q}{r} - 2r\left(1 - 4\lambda e^{-2B} \frac{Q}{r}\right)\partial_r B\right)\frac{\partial_r A}{r} = 0, \end{aligned} \quad (2.6d)$$

where

$$\mathcal{B} \equiv (1 - e^{-2B})/r^2, \quad (2.7a)$$

$$\mathcal{I} \equiv 1 - 8\lambda e^{-2B} Q/r, \quad (2.7b)$$

$$\mathcal{K} \equiv e^B \frac{\frac{PQ}{2} + 4\lambda \mathcal{B}(-P\partial_r B + \partial_r P)}{e^{2B} + 4\lambda(-3 + e^{2B})\frac{Q}{r}}. \quad (2.7c)$$

Eqs. (2.6), though more involved, retain the basic structure of the spherically symmetric Einstein massless-scalar system ($\lambda \rightarrow 0$). Namely, (2.6a) and (2.6b) can be considered constraint equations for the metric variables A and B given data for P and Q on any $t = \text{const.}$ time slice; then (2.6c) and (2.6d) can be considered evolution equations (where hyperbolic) for P and Q . Moreover, as in GR, the system of PDEs (2.2) is over-determined, and can provide another evolution equation for one of the metric functions; we do not solve this equation, rather we monitor its convergence to zero (or more specifically its proxy in the $\vartheta\vartheta$ component of (2.2a)) as a check for the correctness of our solution. We solved Eqs. (2.6) using second order finite difference methods; more details of our numerical approach are detailed in Sec. 2.2.

2.1.3 Boundary and regularity conditions

We discretize the above equations over a domain $r \in [0..r_{\max}]$. At the origin $r = 0$ we require regularity of the fields, leading to

$$\partial_r A(t, r) \Big|_{r=0} = 0, \quad (2.8a)$$

$$B(t, r) \Big|_{r=0} = 0, \quad \partial_r B \Big|_{r=0} = 0, \quad (2.8b)$$

$$Q(t, r) \Big|_{r=0} = 0, \quad (2.8c)$$

$$\partial_r P(t, r) \Big|_{r=0} = 0. \quad (2.8d)$$

Equations (2.6a,2.6b) are first order ODEs for A and B , so strictly speaking we can only impose one boundary condition at one of the boundaries for each. In practice we integrate from $r = 0$ to r_{\max} , setting $A(t, r = 0) = 0$ and $B(t, r = 0) = 0$; with the scalar field variables P and Q appropriately regular as above, the structure of the field equations guarantees that A and B also satisfy the above regularity conditions. Our coordinate system (2.4) has residual gauge freedom in that we can rescale t by an arbitrary function of itself, and we use this to rescale $A(t, r)$ after each ODE integration step so that $A(t, r)|_{r=r_{\max}} = 0$. In that way our time coordinate t measures proper time of static observers at the outer boundary.

For Q and P at the outer boundary we impose the following approximate outgoing radiation boundary conditions:

$$\partial_t Q + \frac{1}{r} \partial_r (rQ) \Big|_{r=r_{\max}} = 0, \quad (2.9a)$$

$$\partial_t P + \frac{1}{r} \partial_r (rP) \Big|_{r=r_{\max}} = 0. \quad (2.9b)$$

These equations can be motivated as follows: from the scalar field equation (2.2b), and from the *assumption* that \mathcal{G} dies off faster than $1/r$ (for example, $\mathcal{G} \sim 1/r^6$ for Schwarzschild black holes), and that the metric corrections due to EdGB corrections are subleading in $1/r$, as $r \rightarrow \infty$ outgoing scalar waves in an asymptotically flat spacetime will approximately obey

$$\partial_t \phi + \frac{1}{r} \partial_r (r\phi) = 0. \quad (2.10)$$

Moreover with the above assumptions we will have $P \approx \partial_t \phi$; taking t and r derivatives (2.10) and ignoring terms subleading in $1/r$ gives us the conditions Eqs. (2.9).

2.1.4 Initial data

For initial data, we are free to choose $P(t = 0, r)$ and $Q(t = 0, r)$ (subject to the regularity conditions described in the previous subsection). For the simulation results presented here, we begin with the following family of initial data for $\phi(t = 0, r)$:

$$\phi(t, r)\Big|_{t=0} = a_0 \left(\frac{r}{w_0}\right)^2 \exp\left(-\left(\frac{r-r_0}{w_0}\right)^2\right), \quad (2.11)$$

where a_0 , w_0 , and r_0 are constants. This then gives $Q(t, r)\Big|_{t=0} = \partial_r \phi\Big|_{t=0}$, and we choose P so that the scalar pulse is initially approximately ingoing:

$$P(t, r)\Big|_{t=0} = -\frac{1}{r}\phi(t, r) - Q(t, r)\Big|_{t=0}. \quad (2.12)$$

Because of spherical symmetry and our constrained evolution scheme, the only “free” data for the metric variables A and B is the overall scale of A , which as discussed in the previous subsection we set so that t measures proper time for static observers at the outer boundary of our domain.

2.2 Numerical methods

We implemented three different finite difference PDE solution methods to solve equations (2.6a)-(2.6d), in order gain confidence that the code crashes occurring some time after formation of sonic lines are due to a property of the underlying continuum equations, rather than a numerical instability associated with a particular discretization scheme. The first two methods, described here, are fully constrained, the third is a partially constrained scheme, described below in 2.2.5. All methods we implemented treat the (P, Q) subsystem as hyperbolic, and are (globally) second order accurate with fixed time and spatial steps. The two hyperbolic methods for (P, Q)

we developed are an iterative Crank-Nicolson scheme (CN), and a fourth order in time Runge-Kutta (method of lines) scheme (RK4). We ran simulations with CFL numbers that varied from 10^{-2} to 0.5. The different methods all give the same results to within truncation error, and once the elliptic region forms all crash in a qualitatively similar manner (growth of short wavelength solution components within the elliptic region at a rate proportional to their wave number. Since our initial data is smooth, these short wavelength components are sourced by truncation error for the most part, and their “initial” amplitudes on the sonic line therefore decrease with resolution. There is some tension here with the fact that higher resolution also allows us to resolve higher frequency modes, which could in principle also allow for more quick growth of oscillations depending on their initial amplitudes.). This gives us confidence that the crashes are due to trying to solve a mixed type equation using hyperbolic methods, which are not well-posed in elliptic regions.

We use the notation f_j^n for a discretized field, where n stands for the time step and $j \in 0..N_r - 1$ is the index within the spatial grid with N_r points. The basic iteration loop we use for both the CN and RK4 evolution schemes, solving for the unknowns at time step $n + 1$ given data at time step n , is as follows:

1. Initialize time step $n + 1$ values for the fields A , B , Q , and P with their values at time step n (this step is unnecessary for the RK4 scheme).
2. For the CN scheme (2.2.1) perform one step of a Newton iteration to correct the unknown values of Q_j^{n+1}, P_j^{n+1} ; for the RK4 integration (2.2.2) take the next substep of the RK4 scheme, saving the results in temporary arrays, or Q_j^{n+1}, P_j^{n+1} for the final step.
3. Integrate the constraints for A_j^{n+1} and B_j^{n+1} given the current values of Q_j^{n+1}, P_j^{n+1} (or the appropriate substep arrays when using RK4). Since equation (2.6b) for B does not depend on A , we first integrate this for B (2.2.3), then substitute the result into (2.6a) before integrating it for A (2.2.4).

4. Repeat steps (ii) and (iii) until (a) for the CN iterative scheme the residuals for the full nonlinear set of equations are below a tolerance set to be a few orders of magnitude smaller than truncation error; (b) for RK4, we have completed all the RK substeps.
5. Apply a Kreiss-Oliger filter (e.g. [KKOC73]) to the now known variables Q_j^{n+1} and P_j^{n+1} . While in principle one may worry that the application of a filter could completely wash out any high frequency growth of modes once an elliptic region forms, with higher resolution the Kreiss-Oliger filter is designed to “converge away”, and with convergence tests we believe we can determine the features of our solutions which are independent of the dissipation we apply to our numerical solution.

2.2.1 CN Hyperbolic PDE solver for Q and P

For the iterative methods we employ a Crank-Nicolson discretization in time (see e.g. [GKO95]), where the equations (2.6a) and (2.6a) are discretized at a time half way between time steps n and $n+1$, which we denote as time step $n+1/2$. Explicitly, we replace each field f and its gradients with the following stencils

$$f \rightarrow \frac{1}{2} (f_j^{n+1} + f_j^n), \quad (2.13a)$$

$$\partial_t f \rightarrow \frac{1}{\Delta t} (f_j^{n+1} - f_j^n), \quad (2.13b)$$

$$\partial_r f \rightarrow \frac{1}{4\Delta r} (f_{j+1}^{n+1} - f_{j-1}^{n+1} + f_{j+1}^n - f_{j-1}^n) \quad (2.13c)$$

We define the residual and field vectors \mathcal{R}_k and v_k respectively via

$$\mathcal{R}_{2j} \equiv (E^{(Q)})_j^{n+1/2}, \quad (2.14a)$$

$$\mathcal{R}_{2j+1} \equiv (E^{(P)})_j^{n+1/2}, \quad (2.14b)$$

$$v_{2j} \equiv Q_j^{n+1}, \quad (2.14c)$$

$$v_{2j+1} \equiv P_j^{n+1}, \quad (2.14d)$$

where $0 < k < 2(N_r - 1)$. The residual terms such as \mathcal{R}_{2j} should be interpreted as plugging in at iterated solution k into the equations of motion, so that with increased iteration the residual terms should go to zero. For the iteration step (ii) above we compute the linear correction δv_j by solving the following matrix equation

$$\mathcal{J}_{ij}\delta v_j + \mathcal{R}_i = 0, \quad (2.15)$$

for δv_j , where

$$\mathcal{J}_{ij} \equiv \frac{\delta \mathcal{R}_i}{\delta v_j}. \quad (2.16)$$

We invert the matrix \mathcal{J}_{ij} in two different ways. For the first method we directly solve (2.15) with a banded matrix solver (the LAPACK routine `dgbsv` [ABB⁺99]). For the second method we solve (2.15) with Gauss-Seidel iteration (e.g. [GVL13]).

2.2.2 RK4 PDE solver for Q and P

We use a standard fourth order in time Runge-Kutta algorithm (see e.g. [AHS11]), so will not describe it here, but note that we still only employ a second order accurate discretization for spatial gradients; i.e. for each field f we use the stencils

$$f \rightarrow f_j^n, \quad (2.17a)$$

$$\partial_r f \rightarrow \frac{1}{2\Delta r} (f_{j+1}^n - f_{j-1}^n). \quad (2.17b)$$

For this study we are able to achieve the requisite accuracy with second order methods and reasonable computer power. We do not use a second order Runge-Kutta method with the radial differences (2.17a) and (2.17b), as it is unconditionally unstable for the linear wave equation. For completeness we explicitly show this. We consider the one dimensional wave equation written in first order form (say $-\partial_t^2 \psi + \partial_x^2 \psi = 0$, and set $v = \partial_t \psi$ and $w = \partial_x \psi$)

$$\partial_t \begin{pmatrix} v \\ w \end{pmatrix} = \begin{pmatrix} 0 & 1 \\ 1 & 0 \end{pmatrix} \partial_x \begin{pmatrix} v \\ w \end{pmatrix}. \quad (2.18)$$

We next Fourier transform in space to obtain

$$\partial_t \begin{pmatrix} \hat{v} \\ \hat{w} \end{pmatrix} = \frac{i \sin(k\Delta x)}{\Delta x} \begin{pmatrix} 0 & 1 \\ 1 & 0 \end{pmatrix} \begin{pmatrix} \hat{v} \\ \hat{w} \end{pmatrix}. \quad (2.19)$$

The second order Runge-Kutta time integrator is essentially a Taylor series expansion to second order of the RHS—that is, for linear operators G the second order Runge-Kutta expression for the equation of motion $df/dt = Gf$ would be $f^{n+1} = (1 + \Delta t G + (1/2)(\Delta t)^2 G^2) f^n$. For our problem at hand we have

$$\begin{pmatrix} \hat{v}^{n+1} \\ \hat{w}^{n+1} \end{pmatrix} = \begin{pmatrix} 1 - \frac{1}{2} \sin^2(k\Delta x) & i \sin(k\Delta x) \\ i \sin(k\Delta x) & 1 - \frac{1}{2} \sin^2(k\Delta x) \end{pmatrix} \begin{pmatrix} \hat{v}^n \\ \hat{w}^n \end{pmatrix}. \quad (2.20)$$

The eigenvalues of the evolution operator on the RHS are

$$\lambda_{\pm} = 1 - \frac{1}{2} \sin^2(k\Delta x) \pm i \sin^2(k\Delta x), \quad (2.21)$$

and their absolute magnitude is $|\lambda_{\pm}| = 1 + \sin^4(k\Delta x)/4 > 1$, so the method is absolutely unstable. If one instead uses fourth order Runge-Kutta though (i.e. if one approximates the time derivative to fourth order in a Taylor series expansion) the wave equation evolution is conditionally stable (subject to a Courant-Friedrichs-Lewy condition).

2.2.3 ODE integrator for B

(2.6b) for the B field takes the schematic form

$$c_{(B)} \partial_r B + d_{(B)} = 0, \quad (2.22)$$

where both $c_{(B)}$ and $d_{(B)}$ are nonlinear functions of B , P , Q , and the radial derivatives of P , and Q . We solved this equation in two different ways. The first involves Newton's method: we define the vectors \mathcal{R}_j and v_j , with $0 \leq j \leq N_r - 1$ and

$$\mathcal{R}_j \equiv (E^{(B)})_{j+1/2}^{n+1}, \quad (2.23)$$

$$v_j \equiv B_j^{n+1}, \quad (2.24)$$

where $(E^{(B)})_{j+1/2}^{n+1}$ is the LHS of (2.6b), with the fields finite differenced using the trapezoid stencil¹ :

$$f \rightarrow \frac{1}{2} (f_{j+1}^{n+1} + f_j^{n+1}), \quad (2.25a)$$

$$\partial_r f \rightarrow \frac{1}{\Delta r} (f_{j+1}^{n+1} - f_j^{n+1}). \quad (2.25b)$$

(2.6b) is nonlinear in B , so we iteratively solve for B_j by solving for the linear correction δv_j in

$$\mathcal{J}_{ij} \delta v_j + \mathcal{R}_i = 0. \quad (2.26)$$

for δv_j , where

$$\mathcal{J}_{ij} \equiv \frac{\delta \mathcal{R}_i}{\delta v_j}. \quad (2.27)$$

As in 2.2.1 we inverted \mathcal{J}_{ij} two different ways: one using a banded matrix solver, and another iteratively using a Gauss-Seidel method. The Newton iteration was then repeated until the residual \mathcal{R}_j was below some tolerance well below truncation error.

We also directly solved (2.22) using a second order Runge-Kutta method, by writing the equation as $\partial_r B = -d/c$.

2.2.4 ODE integrator for A

The ODE for the A field, (2.6a) is of the form

$$c_{(A)} \partial_r A + d_{(A)} = 0, \quad (2.28)$$

where $c_{(A)}$ and $d_{(A)}$ are functions of B , P , Q , and their radial derivatives. We discretize the fields and their derivatives using the trapezoidal rule as above (Eq. (2.25)). Since the ODE for A is linear it is trivial to directly integrate it from the origin $j = 0$ outward; specifically we directly solve for A_{j+1}^{n+1} knowing A_j^{n+1} and the other field values via

$$A_{j+1}^{n+1} = A_j^{n+1} - \Delta r \frac{(d_{(A)})_{j+1/2}^{n+1}}{(c_{(A)})_{j+1/2}^{n+1}}, \quad (2.29)$$

¹We apply these finite difference formulas about the point $f_{j+1/2}^n$, so the stencils are second order.

2.2.5 Partially Constrained Evolution

In a partially constrained evolution, one (or more) variables are typically solved for using an evolution instead of constraint equation. Here, one can do that for B , with the $\vartheta - \vartheta$ component of (2.2a) the corresponding second-order-in-time evolution equation for it. However, in Schwarzschild-like coordinates the momentum constraint (the $t - r$ component of (2.2a)) is effectively a “first integral” for this equation, and instead then we consider this as our evolution equation for B (recall for our constrained evolution we do not use the plain form of the momentum constraint, but first eliminate the time derivative of B using the other equations). For initial data, we solve for B using (2.6b) with either an RK2 or a relaxation method. Once we begin evolving in time, we then use (2.6b) as an independent residual to monitor the constraint.

We solved a discretized version of the $t - r$ component of (2.2a) for B using an iterative Crank-Nicolson method. On any given time step, we follow a similar procedure as above for the iterative constrained scheme, but now iterate over the evolution equations for Q^{n+1} , P^{n+1} , and B^{n+1} a fixed number of times, then solve for A^{n+1} using the constraint equation, (2.6a). We repeat this process until the residuals of the evolutions equations for Q , P , and B are below a tolerance set to be a few orders of magnitude below the truncation error. Afterward we apply a Kreiss-Oliger filter on the variables Q^{n+1} , P^{n+1} , and B^{n+1} , before advancing to the next time step.

2.3 Hyperbolicity analysis

We briefly summarize the theory of characteristics; standard references include [CH62, Whi11, KL89]. Consider a system of first order PDEs ²

$$E^I (v^J, \partial_a v^K) = 0, \tag{2.30}$$

²Through field redefinitions essentially any system of PDEs may be written in this form.

where I, J, K index the N equations of motion and dynamical fields v^J , and a indexes the n coordinates $\{x^a\}$ of the underlying (spacetime) manifold M (and here because of our restriction to spherical symmetry a only runs over the (t, r) coordinates). The *principal symbol* is defined to be

$$\mathbf{p}_J^I(\xi_a) \equiv \frac{\delta E^I}{\delta(\partial_a v^J)} \xi_a, \quad (2.31)$$

where ξ_a is an n dimensional covector. This definition makes no assumption on the properties of the system of partial differential equations E^I , except that we can take function derivatives of them. A *characteristic surface* $\Sigma \subset M$ is spanned by covectors that satisfy the *characteristic equation*

$$\det(\mathbf{p}_J^I(\xi_a)) = 0. \quad (2.32)$$

Replacing ξ_a with ∂_a , one obtains from (2.32) the *eikonal equation* for the characteristic surface.

For a physical interpretation of characteristics, we consider a system of N first order PDEs for N fields (i.e. of the form (2.30)) that is *totally hyperbolic*: i.e it has N real (possibly degenerate) characteristic surfaces³. Consider the solution to small amplitude high frequency wave solutions: $v_0^I e^{ik_a x^a / \epsilon}$, with $0 < \epsilon \ll 1$. Solutions of this form to leading order in ϵ satisfy $\mathbf{p}_J^I(k_a)v_0^J = 0$. Nontrivial solutions to this equation exist if and only if $\det(\mathbf{p}_J^I(k_a)) = 0$; i.e. if and only if the wave vector satisfies (2.32). Thus the wavefronts of high frequency wave solutions propagate on the characteristic surfaces. The characteristic surfaces locally delimit the causal region of influence for hyperbolic PDE (e.g. [Ger96]).

In local coordinates, letting t index the timelike coordinate and i index the space-like coordinates of the background geometry, the speed of these perturbations for the n^{th} characteristic is given by $c^{(n)} = (w^{(n)})^i / w^t$, where $(w^{(n)})^\mu$ is a vector parallel to the n^{th} characteristic surface. We may relate $c^{(n)}$ to the characteristic covector

³For a system that is not totally hyperbolic we could instead consider a totally hyperbolic subsystem; see e.g. Section 2.3.1. Our treatment of characteristics roughly follows that of [Chr08].

by noting that since locally the n^{th} characteristic covector is equal to the gradient of the n^{th} characteristic surface, $\xi_\mu^{(n)} = \partial_\mu \Sigma^{(n)}$, then $(v^{(n)})^\mu \xi_\mu^{(n)} = 0$, from which we find $c^{(n)} = -\xi_t^{(n)}/\xi_x^{(n)}$. For a simple example of this procedure, consider the 1 + 1 dimensional scalar transport equation $\partial_t \psi + v \partial_x \psi = 0$. The symbol is $\mathbf{p} = \xi_t + v \xi_x$, the characteristic equation is $\xi_t + v \xi_x = 0$, and the speed of propagation along the characteristic is $-\xi_t/\xi_x = v$.

We compute the characteristic vectors and speeds for the system of PDEs (2.6a), (2.6b), (2.6c), and (2.6d) in two different ways. In the first, discussed below, we only consider the P, Q evolution subsystem, eliminating all A and B gradients from these equations using the constraints.

2.3.1 Characteristics calculation

Eliminating $\partial_r A$ and $\partial_r B$ from Equations (2.6c) and (2.6d) using Equations (2.6a) and (2.6b), we write the scalar field system in the same form as before,

$$\tilde{E}^I (v^J, \partial_a v^K) = 0, \quad (2.33)$$

but now I, J, K only index the fields Q and P . The principal symbol then reads

$$\mathbf{p}(\xi) = \tilde{\mathbf{a}} \xi_t + \tilde{\mathbf{b}} \xi_r, \quad (2.34)$$

where

$$\tilde{\mathbf{a}} \equiv \begin{pmatrix} \delta \tilde{E}^{(Q)}/\delta (\partial_t Q) & \delta \tilde{E}^{(Q)}/\delta (\partial_t P) \\ \delta \tilde{E}^{(P)}/\delta (\partial_t Q) & \delta \tilde{E}^{(P)}/\delta (\partial_t P) \end{pmatrix}, \quad (2.35a)$$

$$\tilde{\mathbf{b}} \equiv \begin{pmatrix} \delta \tilde{E}^{(Q)}/\delta (\partial_r Q) & \delta \tilde{E}^{(Q)}/\delta (\partial_r P) \\ \delta \tilde{E}^{(P)}/\delta (\partial_r Q) & \delta \tilde{E}^{(P)}/\delta (\partial_r P) \end{pmatrix}. \quad (2.35b)$$

Solving the characteristic equation for the characteristic speeds $c \equiv -\xi_t/\xi_r$, we obtain

$$c_\pm = \frac{1}{2} \left(\text{Tr}(\tilde{\mathbf{c}}) \pm \sqrt{\text{Tr}(\tilde{\mathbf{c}})^2 - 4 \text{Det}(\tilde{\mathbf{c}})} \right), \quad (2.36)$$

where

$$\tilde{\mathbf{c}} \equiv \tilde{\mathbf{a}}^{-1} \cdot \tilde{\mathbf{b}}, \quad (2.37)$$

From standard PDE theory, the sign of the discriminant

$$\mathcal{D} \equiv \text{Tr}(\tilde{\mathbf{c}})^2 - 4\text{Det}(\tilde{\mathbf{c}}) \quad (2.38)$$

of (2.36) at any point of the spacetime determines the character of the PDE there: when $\mathcal{D} > 0$ it is hyperbolic, when $\mathcal{D} = 0$ it is parabolic, and when $\mathcal{D} < 0$ it is elliptic.

In general when $\lambda \neq 0$, $\text{Tr}(\mathbf{c}) \neq 0$, so that $c_+ \neq -c_-$. In GR ($\lambda = 0$), we have

$$\tilde{\mathbf{a}}|_{\lambda=0} = \begin{pmatrix} 1 & 0 \\ 0 & 1 \end{pmatrix}, \quad (2.39a)$$

$$\tilde{\mathbf{b}}|_{\lambda=0} = \begin{pmatrix} 0 & -e^{A-B} \\ -e^{A-B} & 0 \end{pmatrix}, \quad (2.39b)$$

so that $\text{Tr}(\mathbf{c}) = 0$, and the characteristic speeds are $c_{\pm}|_{\lambda=0} = \pm e^{A-B}$. The general expressions for the components of the matrices $\tilde{\mathbf{a}}$, $\tilde{\mathbf{b}}$, and $\tilde{\mathbf{c}}$ can be obtained through straightforward algebraic manipulation of Equations (2.6a)-(2.6d); the resultant expressions are long and not particularly insightful, so we do not write out their full forms here.

2.3.2 Invariance of the characteristics under coordinate transformations

As mentioned, one of the main results of our study is that the EdGB equations in spherical symmetry can be of mixed elliptic/hyperbolic type in certain scenarios. Specifically then, evolution, beginning with initial data where the scalar equation is everywhere hyperbolic, leads to formation of a region where the characteristic structure switches to elliptic (separated by a parabolic so-called *sonic line*, though generically is a co-dimension one surface and not a “line”). The elliptic region is particularly problematic for the validity of EdGB gravity as a classically well-posed,

predictive modified theory of gravity (see the discussion in [RP19b]), and so we would like to be certain that our identification of the elliptic region is not somehow a coordinate artifact. It is well-known that the characteristic structure of a PDE is invariant under so-called point transformations (essentially coordinate transformations treating all the dependent variables as scalars), though it is unclear that this must hold when solving the PDEs of EdGB gravity as a Cauchy IVP problem in an arbitrary gauge. The problem is that the structure and even rank of the principal symbol is unknown until the gauge equations have been chosen (in the ADM [Arnowitt-Deser-Misner] language, that would be the equations governing the lapse α and shift vector β^i : we have effectively chosen the equation for the shift to be the algebraic condition $\beta^i = 0$, and our choice of polar-areal coordinates in spherical symmetry fixes α to within an overall scale).

However, at least we can show that the characteristic structure is invariant under coordinate transformations in the following sense (this is effectively the point-transformation calculation—we consider the same system of partial differential equations but in a different coordinate system). In our evolution scheme we compute the characteristic surfaces Σ as outlined above, and find the corresponding co-vectors $\xi_a = \partial_a \Sigma$. If at a given point $c \equiv -\xi_t/\xi_r$ is purely real, we know the PDE is hyperbolic at that point, and information will propagate along the characteristic surface. This could be superluminal, luminal, or sub-luminal relative to the metric light-cone depending on whether $\xi^a \xi_a$ is negative, zero, or positive respectively, but the scalar equation is still hyperbolic and will have its own causal-cone of influence. If c has an imaginary component this is no longer true, and the PDE is elliptic. The question then is whether this property of the characteristic surface is invariant under coordinate transformations, and the answer is yes. For consider a general coordinate transformation respecting the spherical symmetry of the spacetime : let $x^a = x^a(\tilde{x}^{\tilde{a}})$ where x^a and $\tilde{x}^{\tilde{a}}$ denote the (t, r) and (\tilde{t}, \tilde{r}) coordinates respectively, and the Jacobian of the transformation is $\Lambda^a_{\tilde{a}} \equiv \partial x^a / \partial \tilde{x}^{\tilde{a}}$ (with all coordinates and metrics real). Then

$\xi_{\tilde{a}} = \xi_a \Lambda^a_{\tilde{a}}$, the new coordinate speed is $\tilde{c} \equiv -\xi_{\tilde{t}}/\xi_{\tilde{r}}$, and it is straight-forward to calculate that

$$\text{Im}(\tilde{c}) = \text{Im}(c) \frac{\det[\Lambda^a_{\tilde{a}}]}{ZZ^*}, \quad (2.40)$$

where $Z \equiv -c\Lambda^t_{\tilde{r}} + \Lambda^r_{\tilde{r}}$, and Z^* its complex conjugate. In other words, as long as the transformation is non-singular an imaginary piece to c in one coordinate system implies one in all.

2.3.3 Horizons

As mentioned above, when hyperbolic, the causal cones of the scalar degree of freedom in EdGB gravity ($\lambda \neq 0$) are generally not null. The latter would govern the speed of propagation of fields minimally coupled to the metric, such as a massless scalar field or a Maxwell field⁴. Regarding metric horizons, our coordinate system does not allow evolution through formation of a black hole, as the geometric light speeds are $c_{g\pm} = \pm e^{A-B}$; i.e. the metric is necessarily singular along metric horizons. In strong-field evolutions we estimate that gravitational collapse occurs when c_{g+} starts to evolve to zero at a finite radius; evolution beyond horizon formation will require the use of horizon penetrating coordinates, which we leave to a future study.

2.4 Quasi-local mass

In spherical symmetry in GR, a standard definition of quasi-local mass is the Misner-Sharp mass [MS64, Sza09] (sometimes also referred to as the Hawking-Israel or Hernandez-Misner mass, e.g. [AV10])

$$m_{MS}(t, r) \equiv \frac{r}{2} (1 - (\nabla r)^2) = \frac{r}{2} (1 - e^{-2B(t,r)}), \quad (2.41)$$

⁴In the published version of this chapter [RP19a] we stated also that gravitational waves would follow null characteristics, but that would only be the case if $\lambda = 0$; when $\neq 0$ generally the speed of gravitational waves would not travel along null characteristics in this theory; see e.g. [TFL18].

where r is the areal radius, and the last term on the right is the specific form it takes in our coordinate system. The Misner-Sharp mass satisfies several useful criteria for a quasi-local mass (e.g. [Hay96]). For example, in asymptotically flat spacetimes it reduces to the ADM mass at spatial infinity and the Bondi-Sachs mass at future null infinity. A further useful property of the Misner-Sharp mass is in spherical symmetry one can relate it to the charge associated with the *Kodama current* [Kod80], which satisfies a conservation law purely from properties of the Einstein tensor in spherical symmetry: one does not need to *a priori* connect the Einstein tensor to the matter stress energy tensor to prove this (see e.g. [AV10]). Therefore it is reasonable to use the Misner-Sharp mass in spherically symmetric EdGB gravity as a measure of geometric mass. Then (akin to GR), if desired we can use the EdGB equations of motion to relate it to an integral of an effective matter energy density. Specifically, we write the EdGB equations (2.2a) as $G_{\mu\nu} = \mathcal{T}_{\mu\nu}$, with

$$\mathcal{T}_{\mu\nu} \equiv -2\lambda\delta_{\alpha\beta\rho\sigma}^{\gamma\delta\kappa\lambda}R^{\rho\sigma}{}_{\kappa\lambda}(\nabla^\alpha\nabla_\gamma\phi)\delta_{(\mu}^\beta g_{\nu)\delta} + \nabla_\mu\phi\nabla_\nu\phi - \frac{1}{2}g_{\mu\nu}(\nabla\phi)^2. \quad (2.42)$$

Then, replacing $G_{\mu\nu}$ with $\mathcal{T}_{\mu\nu}$ in the Kodama current (see e.g. [AV10]), a short calculation gives the following integral for the Misner-Sharp mass in our coordinate system (assuming regularity at $r = 0$):

$$m_{MS}(t, r) = \frac{1}{2} \int_0^r dr' (r')^2 e^{-2A(t, r')} \mathcal{T}_{tt}(t, r'). \quad (2.43)$$

The effective stress tensor $\mathcal{T}_{\mu\nu}$ does not always satisfy the usual energy conditions, hence $m_{MS}(t, r)$ is not necessarily a monotonically increasing function of r , as it is in GR coupled to “ordinary” matter. We will show some examples below illustrating the non-monotonicity of m_{MS} .

2.5 Null convergence condition

The null convergence condition (NCC) is

$$R_{\mu\nu}l^\mu l^\nu \geq 0, \quad (2.44)$$

for all null vectors l^α . The NCC plays a role in, for example the classical black hole and cosmological singularity theorems [HE75], the laws of black hole mechanics and dynamical horizons [BCH73, Hay94, AK04], and in the “topological censorship” theorems [FSW93, GSWW99]. It is often stated that these theorems and properties rely on the null energy condition (NEC), $T_{\mu\nu}l^\mu l^\nu \geq 0$, however that comes from replacing the Ricci tensor in the above with an equivalent function of the stress energy tensor using the Einstein equations. We could likewise recast our analysis in terms of a NEC using the effective stress energy tensor introduced in the previous section, though we prefer the geometric interpretation of the NCC.

Related to the fact that the Misner-Sharp mass does not always monotonically increase with radius as discussed in the previous section, EdGB gravity does not generically satisfy the NCC (coupling to matter that satisfies the NCC). This can be seen by contracting (2.2a) with $l^\mu l^\nu$ to compute the explicit form of $R_{\mu\nu}l^\mu l^\nu$:

$$R_{\mu\nu}l^\mu l^\nu = \frac{1}{1 - 4\lambda \nabla_\alpha \nabla^\alpha \phi} \left((l^\mu \nabla_\mu \phi)^2 + 2\lambda l^\mu l^\nu \left((\nabla_\mu \nabla_\nu \phi) R - 4 (\nabla_\mu \nabla_\alpha \phi) R^\alpha{}_\nu - 2 (\nabla_\alpha \nabla_\beta \phi) R^\alpha{}_\mu{}^\beta{}_\nu \right) \right). \quad (2.45a)$$

Here, the only term that is manifestly positive definite is the kinetic term of the scalar in the small coupling ($\lambda \rightarrow 0$) limit. We will show examples below of scenarios where the NCC is violated during evolution in EdGB gravity (and the regions where it does roughly coincide with negative effective energy density in the Misner-Sharp mass, and is present where the equations become elliptic); specifically, we numerically evaluate $R_{\mu\nu}l^\mu l^\nu$ for outgoing null vectors $l^\mu \equiv (e^{-A}, e^{-B}, 0, 0)$.

2.6 Results: Hyperbolicity

2.6.1 *Dynamic* loss of hyperbolicity and the “mixed type” properties of EdGB gravity

Here we consider initial data (2.11) with $a_0 = 0.02$, $r_0 = 20$, $w_0 = 8$, and $\lambda = \pm 50$; $m \sim 0.93$ for both cases (so this is fairly compact initial data, but is “weak” in the sense that we are still a factor of a few in mass away from initial data that would form a black hole; in [RP19b] further data was given showing scaling to the truly weak field (low compaction), strong coupling regime).

For both cases (i.e. independent of the sign of λ), the solutions develop an elliptic region—see Figures 2.3 and 2.6. Interestingly, even though the sign of the Gauss-Bonnet coupling λ has little effect on the ADM mass of the spacetime, it significantly affects when and where the elliptic region forms, as is evident in these figures. Preceding formation of this elliptic region, the outgoing scalar field characteristic speeds near it become negative, akin to trapped surface formation in GR gravitational collapse. However, the spacetime outgoing null characteristic speeds e^{A-B} remain positive and well away from zero throughout the integration domain⁵. This provides strong evidence (but does not prove as we do not consider any degrees of freedom that travel along null characteristics) that the elliptic region is not “censored” by spacetime causal structure (the ADM mass of the spacetimes are below the smallest known static black hole solutions in EdGB gravity [KMR+96, SZ14a, SZ14b], and even so, the elliptic regions form well outside $r = 2m$, so it does not seem plausible that some spacetime trapped region could eventually form to hide the elliptic region from asymptotic view). At the sonic line bounding the hyperbolic from elliptic region, all field variables are smooth and finite. In particular, there is no geometric or scalar field singularity that might otherwise have suggested the classical theory has already

⁵As we consider dynamics only in spherical symmetry, we cannot say anything about the speed of motion of metric degrees of freedom in our setup.

ceased to give sensible predictions prior to this; see Figures 2.7 and 2.10 that show the Ricci scalar as an example.

That the character of the (P, Q) subsystem is hyperbolic in some regions of the spacetime, and elliptic in others (separated by the parabolic sonic line), means the EdGB equations can be of *mixed type* (note of course that this is different from coupled elliptic/hyperbolic systems often encountered in GR evolution, where some equations are elliptic, others hyperbolic, but each equation maintains its definite character throughout the domain). Mixed-type equations are not as common in the literature, but do arise in several situations, such as steady transonic flow (see for example [Otw15], which also discusses other areas where mixed type equations appear). There are two canonical mixed type equations that at least locally (near the sonic line) are expected to capture the nature of most mixed type equations : the Tricomi equation

$$\partial_y^2 u(x, y) + y \partial_x^2 u(x, y) = 0, \quad (2.46)$$

and the Keldysh equation

$$\partial_y^2 u(x, y) + \frac{1}{y} \partial_x^2 u(x, y) = 0. \quad (2.47)$$

These equations are hyperbolic/parabolic/elliptic for $y < 0$ / $y = 0$ / $y > 0$. The main qualitative differences between these two equations are how the characteristics in the hyperbolic region meet the parabolic sonic line, and how the characteristic speeds become imaginary. For the Tricomi equation, the characteristics intersect the sonic line orthogonally, with the corresponding speeds going imaginary passing through zero there. For the Keldysh equation, the characteristics intersect the sonic line tangentially, with the characteristic speeds diverging there before becoming imaginary. This affects the degree of smoothness one can generally expect for solutions to these equations, with the Keldysh equation having weaker regularity of solutions on the sonic line (see e.g. [Otw15]). Though the EdGB equations are vastly more complicated than these simple prototypes, at least based on the way the characteristics intersect

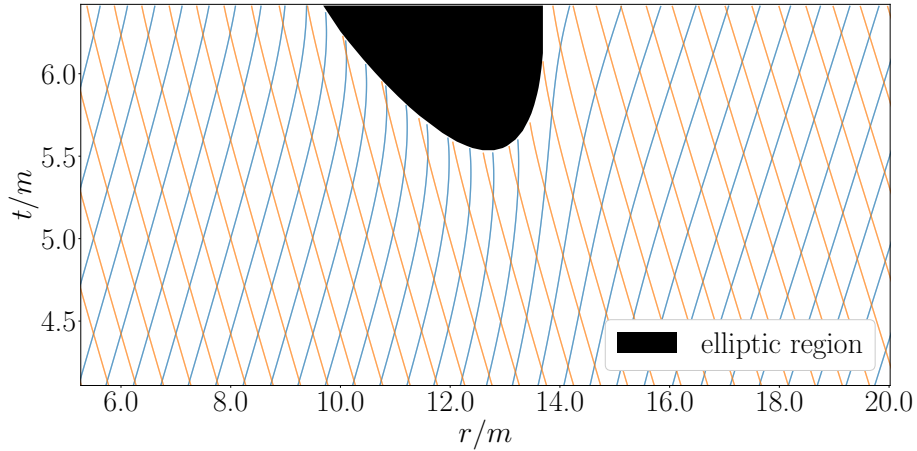


Figure 2.1: EdGB characteristics

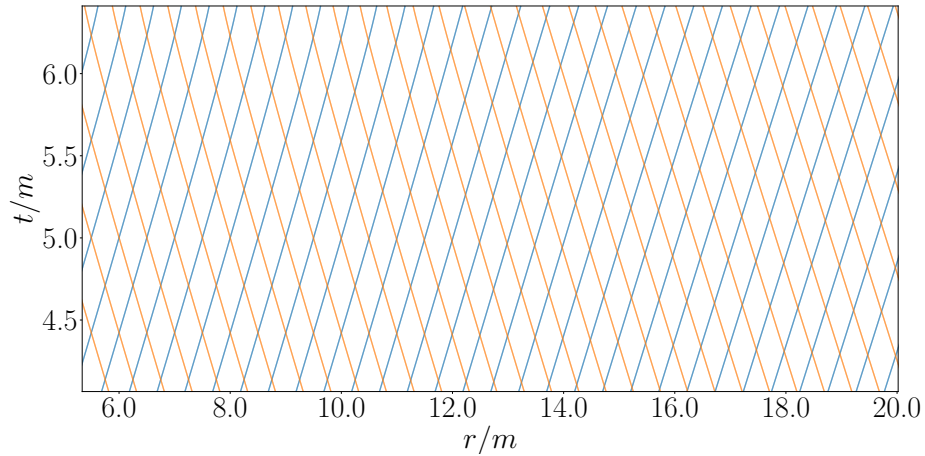


Figure 2.2: Null characteristics

Figure 2.3: Characteristic lines from a strong coupling, weak field case: $a_0 = 0.02, w_0 = 8, r_0 = 20, \lambda = 50, r_{max} = 100, N_r = 2^{12} + 1; m \sim 0.93$. The top panel shows the characteristics of the principal symbol (2.34) of the EdGB equations, the bottom panel the spacetime radial null curves. Compare Figure 2.6 for a case with the same initial data, but opposite sign for λ .

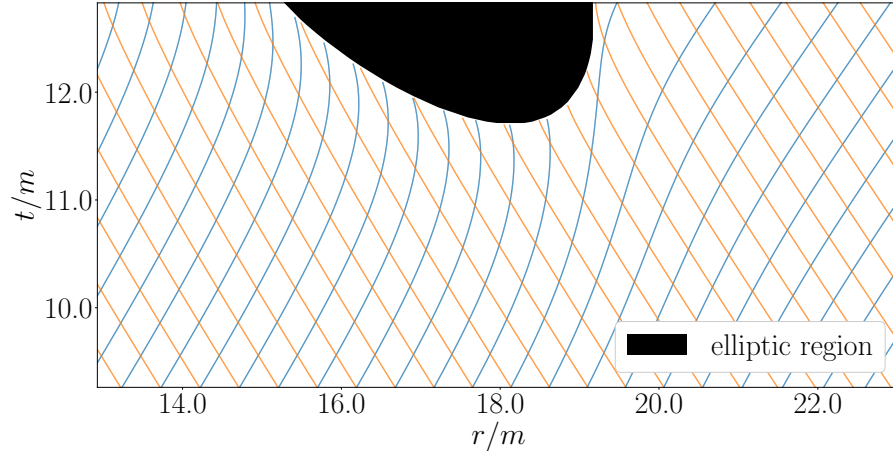


Figure 2.4: EdGB characteristics

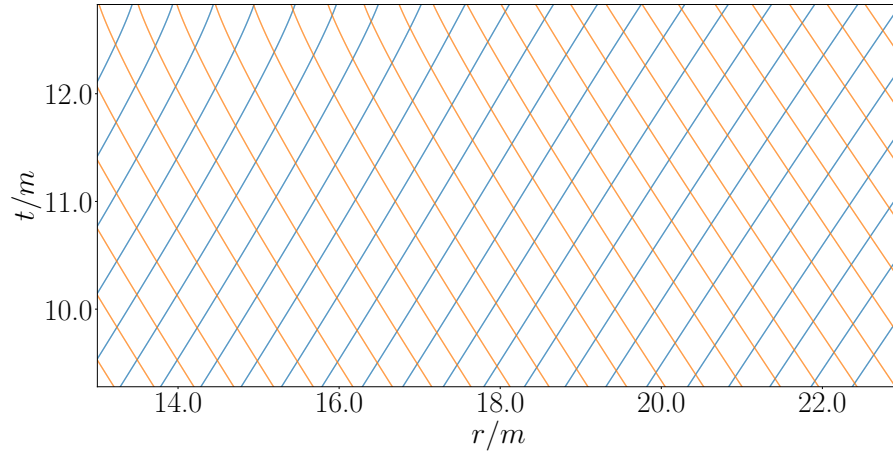


Figure 2.5: Null characteristics

Figure 2.6: Characteristic and null lines from a case with identical initial data as in Figure 2.3, but here $\lambda = -50$ (opposite sign). Qualitatively the figures are similar, but notice the different vertical and horizontal scales.

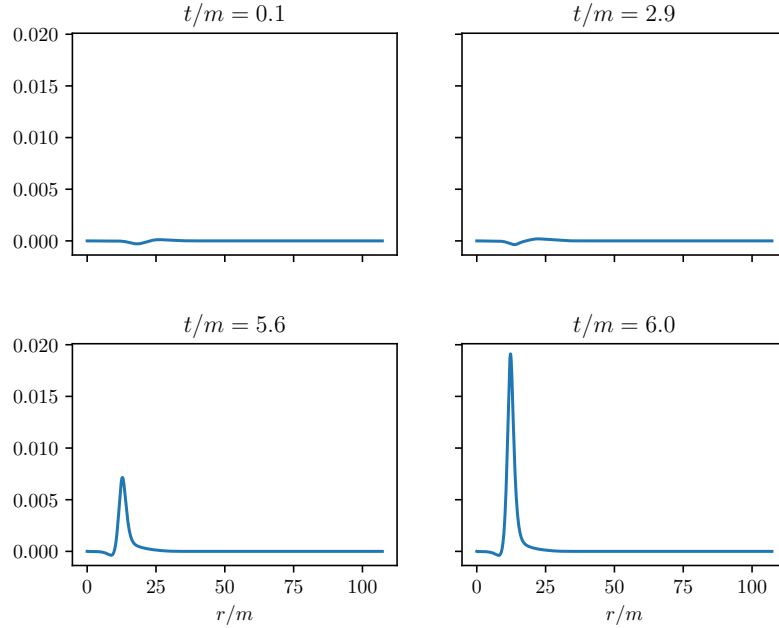


Figure 2.7: The Ricci scalar R at several different times from the strong coupling, weak field run with $\lambda = 50$ (as in Figure 2.3). The lower left panel corresponds to the time the elliptic region first forms at $r/m \sim 12.5$.

the sonic line, as is apparent in Figures 2.3 and 2.6, and that the characteristic speeds go to zero there, it appears that the EdGB equations are of Tricomi type. This is typical for all cases we have run where an elliptic region forms (though interestingly, for a certain class of $P(X)$ Horndeski theories in similar collapse scenarios, [BLL19] find either Tricomi or Keldysh behavior approaching the sonic line, depending upon the initial data in the hyperbolic region).

That the mixed type behavior here appears to be of Tricomi type is a somewhat promising sign for EdGB gravity in terms of regularity on the sonic line (as we explicitly find in our solutions); however, that an elliptic region forms regardless of its type is problematic for the theory being capable of serving as a viable, physical model that can make predictions in the sense of possessing a well-posed initial value problem (for further discussion on this see [RP19b]).

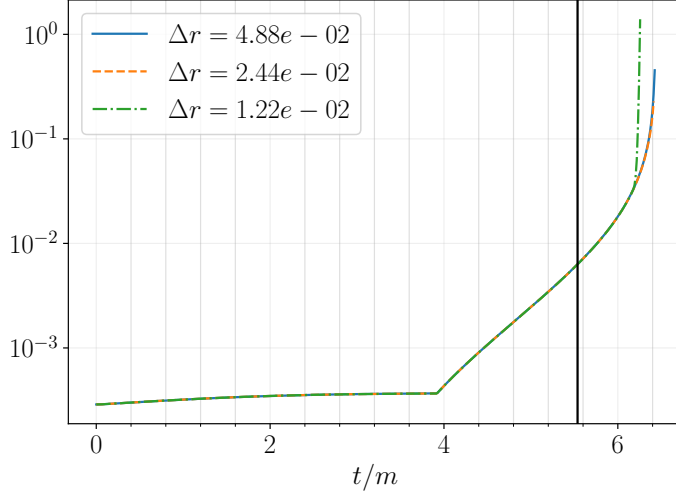


Figure 2.8: $|R|_\infty$ at three resolutions

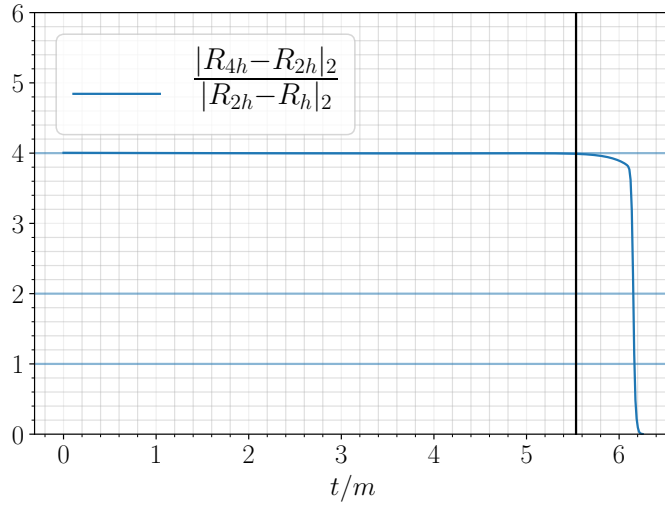


Figure 2.9: Convergence of R

Figure 2.10: The top panel shows the L_∞ norm of the Ricci scalar R with time from the strong coupling, weak field $\lambda = 50$ case (as depicted in Figure 2.7 above). To demonstrate convergence, data from 3 different resolutions are shown. The bottom panel shows a corresponding convergence factor (computed with the L_2 norm), consistent with second order convergence prior to formation of the elliptic region (denoted by the vertical line at $t/m \sim 5.6$). This shows we are converging to a finite value of R at the time the sonic line is first encountered. Since following this time the EdGB (P, Q) subsystem becomes ill-posed treated as a hyperbolic PDE system, as indicated by the drop in the convergence factor (which in theory will happen more rapidly with ever increasing resolution), we cannot say anything conclusive about some putative analytic solution at any given resolution beyond this.

2.6.2 Scaling and loss of hyperbolicity

To characterize the strength of the EdGB modification, we perform the following dimensional analysis. For a compact source of scalar field energy with characteristic length scale L , $|\nabla\phi| \sim |\phi_0|/L$, where $|\phi_0|$ is the maximum difference between ϕ and $\phi(t, r = \infty)$ (as we consider a shift symmetric theory). In GR, $|R_{\mu\alpha\nu\beta}| \sim m/L^3$, where m is the Arnowitt-Deser-Misner (ADM) mass. Using these expressions to characterize the magnitudes of the various terms in (2.2), and noting that λ has dimension *length*², we define a dimensionless parameter

$$\eta \equiv \frac{\lambda}{L^2} |\phi_0|, \quad (2.48)$$

so that for $\eta > 1$ we expect strong modifications from GR solutions. For the class of initial data above (to within factors of a few) $L \sim w_0$ and $|\phi_0| \sim a_0(r_0/w_0)^2$.

The gravitational strength of the initial data can be characterized by the compaction $C \equiv m/L$. Here we present results on cases with large GR-modifications ($\eta \gtrsim 1$), and low ($C \ll 1$) to moderately strong field, but not black hole forming ($C \lesssim 1$). We first show results from one typical case, then a survey confirming the scaling relation (2.48) above.

We now show a result from a survey of evolutions, demonstrating that the previous example is not a fine-tuned special case within the initial data family Eq. (2.11), and that formation of an elliptic region seems to always appear for sufficiently strong coupling, as characterized by η . For this survey we still keep w_0 and r_0 fixed (now $w_0 = 10, r_0 = 20$), but for a given λ search for the amplitude parameter a_0 above which evolution leads to formation of a sonic line (within the run time of the simulations, corresponding to roughly a light-crossing time of the domain). Fig. 2.11 shows the results, and that the slope of the curve is close to -1 suggests the scaling (2.48) implied by the dimensional analysis does roughly hold in this set up.

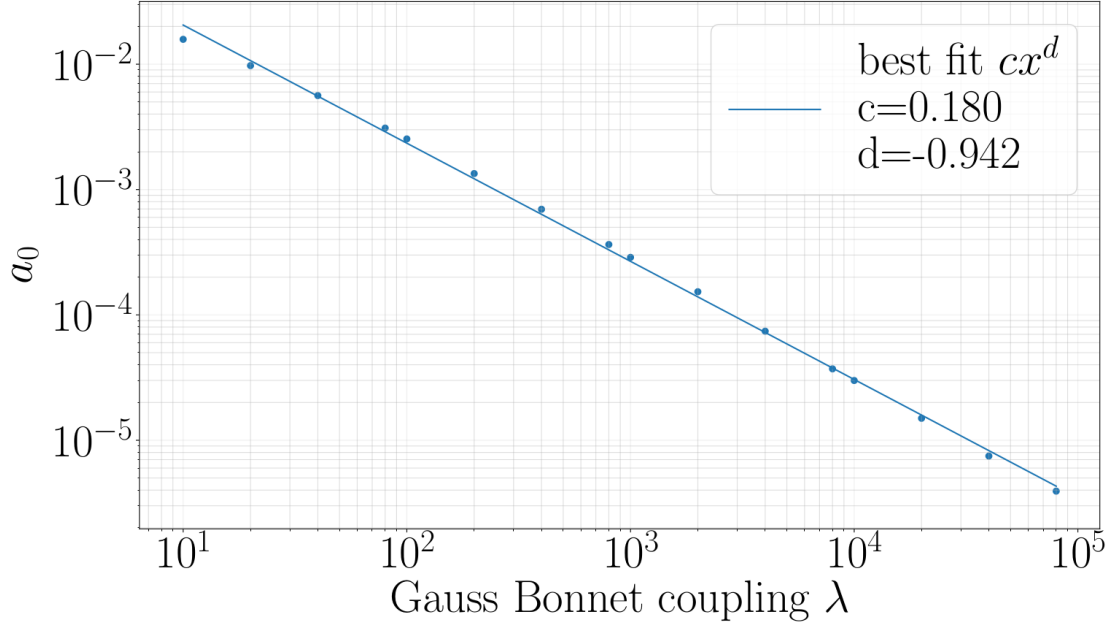


Figure 2.11: Approximate threshold amplitude for the initial data Eq. (2.11) (with fixed $w_0 = 10, r_0 = 20$) above which evolution leads to the formation of a sonic line, as a function of λ (run with a spatial resolution $\Delta r \sim 1 \times 10^{-1}$, and the outer boundary at $R_0 = 100$). The ADM mass m scales as $\sim a_0^2$, and is not particularly sensitive to λ in this range of parameter space, hence the vertical axis also serves as an indication of the gravitational strength of the initial data : at $a_0 \sim 1.6 \times 10^{-2}$, $m \sim 0.26$, while at $a_0 \sim 3 \times 10^{-5}$, $m \sim 1 \times 10^{-6}$.

2.7 Results: Misner-Sharp mass and Null Convergence Condition

Figure 2.12 is a plot of the initial Misner-Sharp mass profiles for the two strong coupling ($\lambda = \pm 50$) weak field cases, together with initial data with equivalent parameters for the GR ($\lambda = 0$) case. As discussed in Section 2.4, we may interpret $\partial_r m_{MS}(t, r)/4\pi r^2$ as an effective local energy density at (t, r) . As is apparent in the figure, for EdGB gravity there are clearly regions where this energy density is negative (this phenomenon has been noticed before in static solutions, see e.g. [KMR⁺96]). Despite large variations in m_{MS} in the interior as the Gauss-Bonnet coupling λ is varied, we find that the ADM mass (estimated by evaluating the Misner-Sharp mass at $r = r_{max}$) depends much more weakly on λ . With fixed initial data ($a_0 = 0.02$,

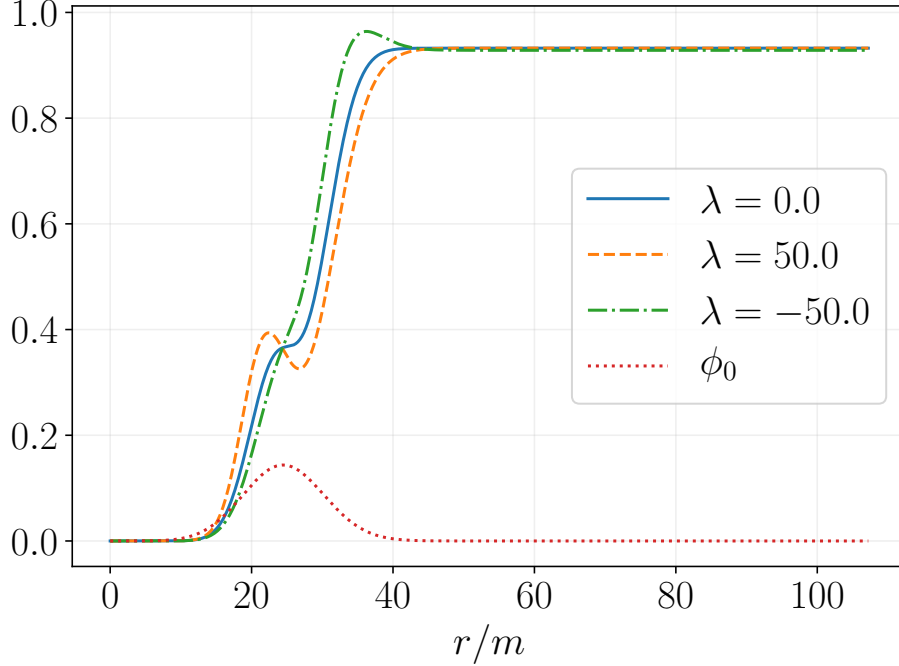


Figure 2.12: The initial Misner-Sharp mass m_{MS} (2.41) and scalar field (2.11) profile for the strong coupling, weak field cases with $\lambda = \pm 50$ (initial data as in Figures 2.3 and 2.6), together with a $\lambda = 0$ case for reference. The initial scalar field data is the same for all three λ runs. We see that m_{MS} is not always monotonically increasing as in GR ($\lambda = 0$), though interestingly despite significant variations with λ in the interior profile of m_{MS} , the asymptotic values are largely insensitive to λ .

$w_0 = 8$, $r_0 = 20$), the ADM mass changes by at most 1 part in 10^3 as λ varies from -75 to 75, where we estimate the numerical error in this quantity to be less than 1 part in 10^4 (from truncation error and finite radius effects).

Related to the negative effective energy densities, we find that the NCC (2.44) is violated around these regions for the non-zero λ cases : see Figures 2.13 and 2.16. We note that we find no correlation between the existence of negative energy density regions or regions of NCC violation and the formation of elliptic regions. While we always observe negative energy density regions and regions of NCC violation at the formation of an elliptic region, we also observe those regions in simulations where the evolution remains hyperbolic.

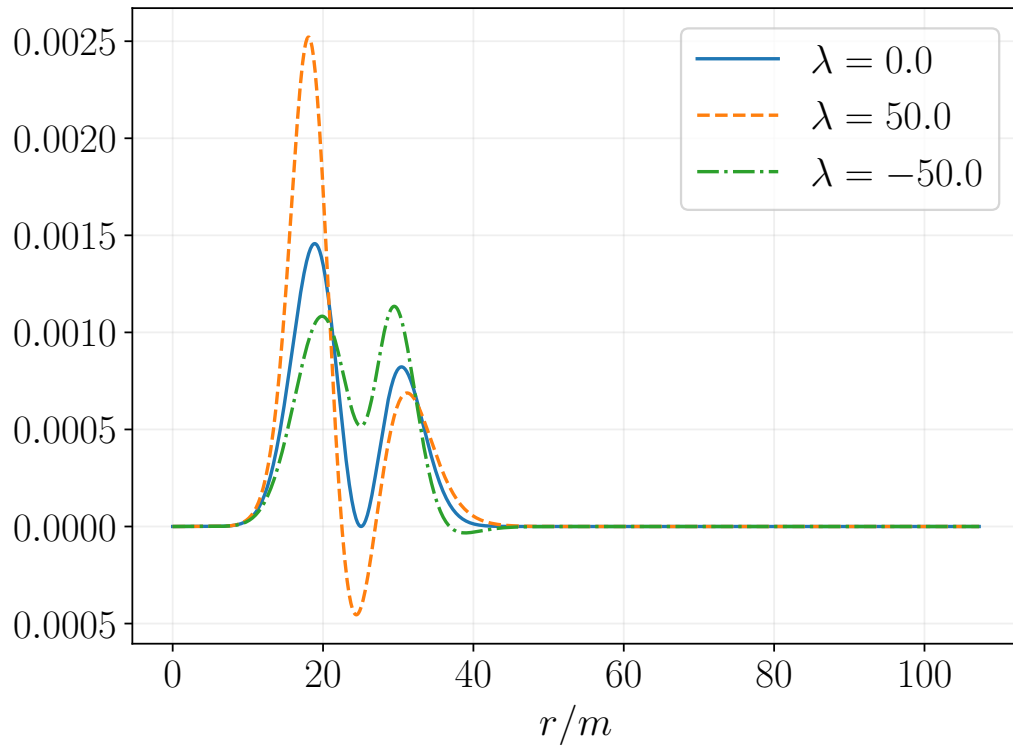


Figure 2.13: The NCC (2.44) evaluated at $t = 0$ for the two strong coupling, weak field cases (as in Figures 2.3 and 2.6), together with the GR case ($\lambda = 0$) for reference. The regions of NCC violation (for $\lambda \neq 0$) roughly correspond to the regions of negative effective energy density; compare with Figure 2.12.

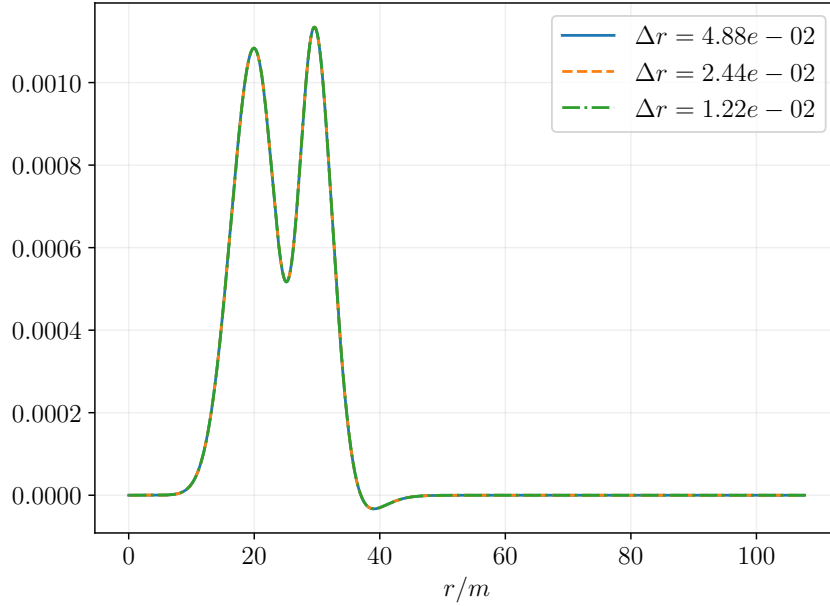


Figure 2.14: NCC at $t = 0$ at three resolutions—notice the small amount of NCC violation near $r/m \approx 40$.

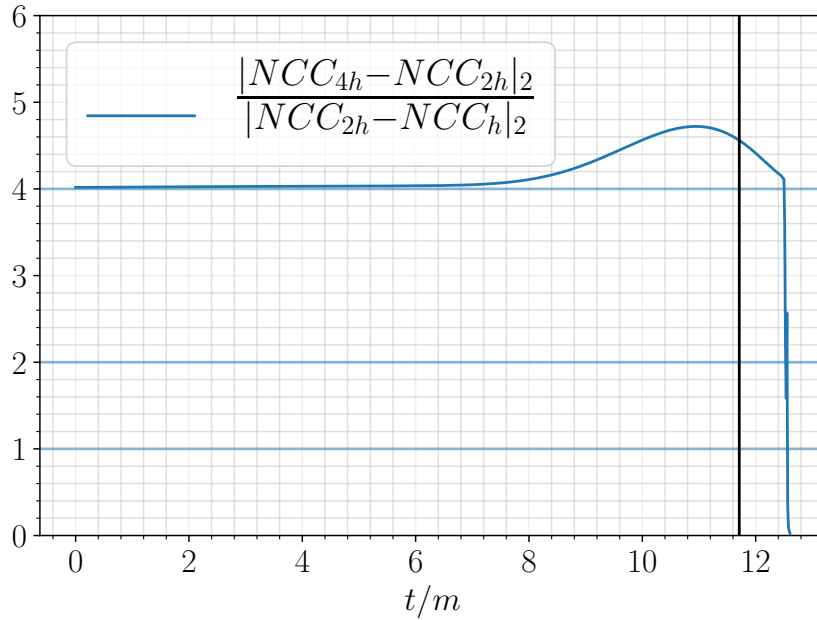


Figure 2.15: Convergence factor of NCC

Figure 2.16: The NCC (2.44) at $t = 0$ (top) for the $\lambda = -50$ case (as in Figure 2.6) computed with 3 resolutions, and a corresponding convergence factor vs time (bottom), consistent with second order convergence of the solution. The sonic line for this case is first encountered at $t/m \sim 11.7$, indicated by the vertical solid line on the right panel.

2.8 Convergence of simulations

In addition to convergence data we have already shown in Figures 2.10 and 2.16, in Figure 2.19 we show convergence plots from the two strong coupling ($\lambda = \pm 50$) cases for the independent residual of the $\vartheta\vartheta$ component of the EdGB equations (2.2a). That this converges to zero (at second order) prior to formation of an elliptic region is a rather non-trivial check of the correctness of our solution, as $E_{\vartheta\vartheta}$ depends on temporal and spatial gradients of all variables (P, Q, A, B) in the problem (the EdGB equations, as GR, are over-determined, allowing for such non-trivial checks of a solution obtained from a complete subsystem of PDEs). That we lose convergence after formation of the elliptic region is consistent with the fact that we are attempting to solve a mixed type equation using hyperbolic methods, which are not well-posed in the elliptic region (for more discussion on this see [RP19b]).

We report that in addition to the convergence tests we have discussed and presented in this paper, we achieved second order convergence before the formation of elliptic regions for all of the fields and diagnostics we implemented in our simulations, including the EdGB and null characteristics (as shown for example in Figure 2.3), and the mass aspect, (Figure 2.12). Interestingly, as with the regions of NCC violation, with the resolutions reported in this paper we resolve the regions of *negative* energy density ($\partial_r m_{MS} < 0$) seen in Figure 2.12.

2.9 Conclusion

In this paper we presented studies of numerical solutions of EdGB gravity in spherical symmetry in gravitational collapse-like scenarios, focusing on how properties of the solutions differ from similar situations in Einstein gravity minimally coupled to a massless scalar field. For sufficiently weak EdGB coupling we find results similar to GR : a weak field limit where the scalar field pulse disperses beyond the integration domain, and a strong field where a geometric horizon begins to form. In the latter

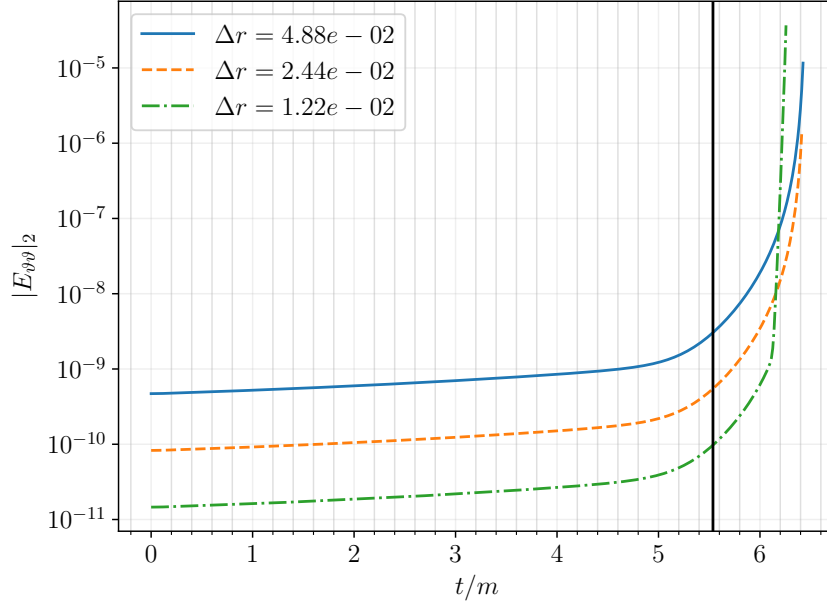


Figure 2.17: $|E_{\vartheta\vartheta}|_2$. $\lambda = 50$

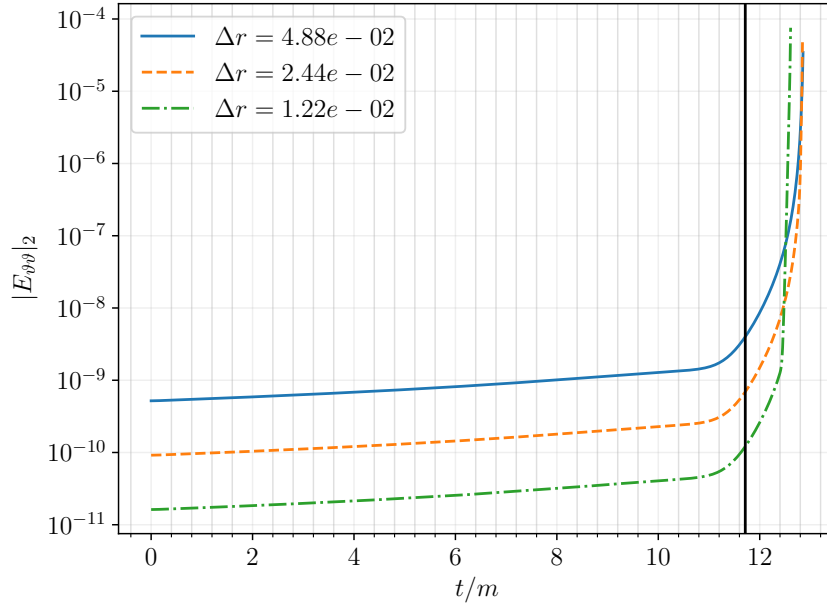


Figure 2.18: $|E_{\vartheta\vartheta}|_2$. $\lambda = -50$

Figure 2.19: The L_2 norm of the residual of $E_{\vartheta\vartheta}$ (2.2a) for the weak field, strong coupling cases (as in Figures 2.3 and 2.6). The convergence to zero prior to formation of the elliptic region is consistent with second order convergence; the growth of the residual and failure of convergence past this time is consistent with trying to solve a mixed type equation using a hyperbolic solution scheme.

scenarios, the EdGB scalar begins to grow outside the nascent horizon in a manner consistent with known static “hairy” BH solutions. In the strong EdGB coupling regime, we find markedly different behavior from GR : (1) the equations of motion can be of mixed type, where an initially hyperbolic system shows development of a parabolic sonic line in a localized region of the domain, beyond which the character of the PDEs switches to elliptic (2) there are regions of negative effective energy density, and (3) there are regions where the NCC is violated. In the cases we have studied these three properties occur together within roughly the same region of spacetime. While the potential physical consequences for negative energy density and NCC violation have been extensively discussed in the modified gravity literature, the physical interpretation of mixed type equations remains largely unexplored. At the very least, mixed type behavior signals loss of predictability in the theory in the sense of it ceasing to possess a well-posed IVP.

One of our main motivations for studying EdGB gravity is to discover a viable, interesting modified gravity theory to confront with LIGO/Virgo binary BH merger data, in particular the part of the signals attributable to coalescence. In that regard, our results reported here and in a companion paper [\[RP19b\]](#) do not yet rule out a coupling parameter that gives a smallest possible static BH solution of around a few solar masses (which would give the most significant differences from GR for stellar mass BH mergers), *if* we assume there is no cosmological background for the EdGB scalar (i.e. it is only present as sourced by curvature produced by other matter/BHs in the universe, though even then we need to ignore problems that might arise in the very early, pre-Big-Bang-Nucleosynthesis universe). So we have a tentative green light to continue this line of exploration of EdGB gravity. The next step is to solve the EdGB equations in spherical symmetry in a horizon penetrating coordinate system. This will allow us to begin addressing issues of long term, non-linear stability of hairy BHs, and perform a more thorough investigation of the strong field, strong coupling regime. Considering the qualitatively different behavior for GR we see in

the EdGB simulations in the strong coupling regime, it would also be interesting to understand the nature of critical collapse in EdGB gravity, where (at least in GR) one can dynamically evolve from smooth initial data to regions of potentially unbounded curvature. We are presently working on a code to study this phenomena as well.

Chapter 3

Black holes in EdGB gravity with a linear Gauss-Bonnet coupling

Here we discuss a series of numerical studies on the nonlinear dynamics of EdGB gravity with a linear Gauss-Bonnet coupling, with a particular set of black hole initial data. This chapter is largely adapted from the publication [RP20b], which we coauthored with Frans Pretorius. Some of the results in this paper indirectly rely on the publication [Rip19] as well.

3.1 Introduction

We present numerical results on the nonlinear evolution of spherically symmetric black hole solutions in a modified gravity theory: Einstein dilaton Gauss-Bonnet (EdGB) gravity. EdGB gravity is one of the few known scalar tensor theories that may admit sensible classical evolution (at least for some open subsets of initial data; see our earlier studies [RP19b, RP19a]), yet does not allow the Schwarzschild or Kerr stationary black hole solutions. Instead the expected solutions are conjectured to be “scalarized” black holes [KMR⁺96, SZ14a, SZ14b] (the detailed form of this statement depends on the functional form of the Gauss-Bonnet coupling and scalar field potential

[SMS⁺19, MSB⁺19]). The variant of EdGB gravity we consider is poorly constrained by weak field gravity measurements (e.g. from binary pulsars [YSY16]), though to be consistent with the speed of gravitational waves inferred by the binary neutron star merger GW170817 [A⁺19] requires a negligible cosmological background for the dilaton field [TFL18]¹. Assuming the latter, the strongest constraints on the theory may then come from gravitational wave observation of the final moments of binary black hole inspiral. The theory thus provides an interesting alternative to general relativity (GR) to compare against when gravity is in the strong field dynamical regime (see e.g. [YYP16] and references therein).

From the perspective of effective field theory, EdGB gravity can be motivated as the leading correction to GR in a low energy expansion of quantum gravity that incorporates mixing between a scalar degree of freedom and the tensor (metric) degrees of freedom of GR [Zwi85, GS87]. Then one would not expect significant modifications to GR away from the Planck scale, and in particular not for astrophysical black holes. Alternatively, as we do here, one could consider the coupling parameter of the theory to be arbitrary, and EdGB gravity taken verbatim as a classical theory of gravity with a scale dependent modification to GR. Such a theory may not be mathematically well-posed in some regimes (or in a generic sense not at all [PR17, Pap17]), though a “healthy” sector of solutions could still be extracted by treating it as an effective field theory and limiting consideration to small perturbative corrections to GR. Several groups are pursuing such an “order reduction” approach to understanding EdGB gravity, and related theories where beyond-Ricci curvature scalars are added to the Einstein Hilbert gravitational action [BSW16, YYP16, OSSH17, OST19, WGPS19, OSST19, Oko19, OSM⁺20]. Another approach, inspired by the Israel-Stewart “fix” of relativistic hydrodynamics [IS79], is to explicitly modify the GR-extensions to lead to well-posed equa-

¹ We note that in asymptotically flat spacetimes it has been explicitly shown that the speed of linearized tensor and scalar perturbations in EdGB gravity approach light speed in regions far away from gravitating sources [Ayy14]

tions [COL17, AL19].

Our approach is instead to attempt to solve the complete classical field theory, and discover which classes of initial data (if any) lead to well-posed evolution. Our motivation is two fold. The first is the desire to know how classical gravity can in principle differ from the predictions of GR in the dynamical strong field regime, as is applicable to the last stages of binary black hole coalescence. This could give more meaning to quantitative statements of consistency of observed waveforms with the predictions of GR, help constrain EdGB gravity, or discover modifications to GR of a class similar to that offered by EdGB gravity. Though an effective field theory approach as described above is likely “guaranteed”, by construction, to give well-posed evolution schemes for small deviations to GR, it is still unknown if this approach could be pushed to solve for modifications large enough to provide waveforms distinguishable from GR in an observation, given the typical signal-to-noise ratios expected from the current generation of ground based detectors, and taking waveform degeneracies into account.

The second reason is that nonlinear modifications of gravity have been introduced in attempts to address the discovery of dark matter, dark energy, solve the flatness and horizon problems of early universe cosmology, and resolve the issues of the initial cosmological singularity and singularities formed during gravitational collapse. EdGB is an important and representative member of a class of modified gravity theories, Horndeski theories, that have been invoked to solve these various issues within classical GR (for a recent review on Horndeski theories see [Kob19]), and it thus is interesting to see if the theory is mathematically sensible as a classical field theory.

Previous studies of EdGB black holes have focused on static solutions to the theory (e.g. [SZ14b, SMS+19, MSB+19]), the dynamics of the EdGB scalar in the *decoupling limit* (e.g. [BSW16, BSW17, WGPS19]), or linear perturbations of static EdGB black hole backgrounds (e.g. [BSMC+16]). Additionally, a recent work [Oko19] explored the dynamics of the scalar and metric fields of the theory from an effective-field theory

framework. There it was shown that scalarized, rotating EdGB black hole solutions are stable for small enough couplings, up to leading order in metric and scalar field perturbations. Restricted to spherical symmetry, our results extend this to all orders in the Gauss-Bonnet coupling, showing consistency for small couplings, and showing where and how the theory breaks down for large couplings.

In a previous work, we studied the dynamics of EdGB gravity in spherically symmetric collapse using horizon-avoiding coordinates [RP19b, RP19a]. There we considered collapse of a dense concentration of the dilaton field, and for sufficient mass could show a horizon was forming, though we could not evolve beyond that time. Here, we give results from a new code solving the EdGB equations in horizon penetrating coordinates, allowing us to investigate the long-term stability of scalarized black holes (for times up to of order $t \sim 10^3 m$, where m is the mass of the black hole). Also, we begin with the Schwarzschild solution as initial data (with an optional exterior dilaton field perturbation).

Upon evolution of Schwarzschild initial data, we find that the scalar hair grows, and an elliptic region forms in the interior of the black hole. This indicates black hole physics in EdGB gravity has aspects of it governed by a mixed elliptic-hyperbolic equation (or simply *mixed-type* equation), and it is unclear how this could affect the Cauchy problem exterior to the horizon. I.e., there is no *a-priori* reason to expect this elliptic region to “obey” cosmic censorship, and leave the scalar in the exterior domain to be governed by a hyperbolic partial differential equation (PDE). Instead, we will simply *assume* that this is possible, and *excise* the elliptic region from the domain. If during subsequent evolution no new elliptic region forms, and the solution settles to a stationary state, we will claim this is a self-consistent application of excision, and the resulting hairy black hole is stable (to within limitations of numerical evolution)².

²Also in this case, that we can freely specify the initial data for all characteristics is not in contradiction with the result of Morawetz on the Tricomi mixed-type equation [Mor70], which seems the relevant mixed-type equation for EdGB gravity here [RP19a]; rather, following the excision philosophy, we simply do not care what irregularities or lack of uniqueness occur in the interior of the excised region.

We do find this to be the case for Gauss-Bonnet couplings below an extremal limit for a given black hole mass. We compare these solutions to the scalarized decoupled black hole solutions of EdGB gravity, and find good agreement, the better the smaller the Gauss-Bonnet coupling is (for a fixed black hole mass). However, above the extremal limit, an elliptic region does form outside the horizon, indicating a break-down of the exterior Cauchy problem for small black holes (relative to the EdGB coupling scale).

An outline of the rest of the paper is as follows. In Sec. 3.2 we describe the equations of motion, variables, and metric ansatz we use. In Sec. 3.3 we describe aspects of the numerical code, including our excision strategy, as well as some diagnostic quantities we monitor. In Sec. 3.4 we describe the results mentioned above in detail, and end in Sec. 3.5 with concluding remarks. We leave some convergence results, and a derivation of the decoupling limit about a Schwarzschild black hole in Painlevé-Gullstrand coordinates, to the appendices. We use geometric units ($8\pi G = 1$, $c = 1$) and follow the conventions of Misner, Thorne, and Wheeler [MTW17].

3.2 Equations of motion

The action for the EdGB gravity theory we consider is

$$S = \frac{1}{2} \int d^4x \sqrt{-g} (R - (\nabla\phi)^2 + 2\lambda f(\phi)\mathcal{G}), \quad (3.1)$$

where $f(\phi)$ is a (so far unspecified) function, and \mathcal{G} is the Gauss-Bonnet scalar

$$\mathcal{G} \equiv \frac{1}{4} \delta_{\rho\sigma\gamma\delta}^{\mu\nu\alpha\beta} R^{\rho\sigma}{}_{\mu\nu} R^{\gamma\delta}{}_{\alpha\beta}, \quad (3.2)$$

where $\delta_{\rho\sigma\gamma\delta}^{\mu\nu\alpha\beta}$ is the generalized Kronecker delta. In geometric units, the Gauss-Bonnet coupling constant λ has dimensions length squared. Varying (3.1) with respect to the metric and scalar fields, the EdGB equations of motion are

$$\begin{aligned} E_{\mu\nu}^{(g)} &\equiv R_{\mu\nu} - \frac{1}{2}g_{\mu\nu}R + 2\lambda\delta_{\alpha\beta\rho\sigma}^{\gamma\delta\kappa\lambda} R^{\rho\sigma}{}_{\kappa\lambda} (\nabla^\alpha\nabla_\gamma f(\phi)) \delta^\beta_{(\mu} g_{\nu)\delta} - T_{\mu\nu} = 0, \quad (3.3a) \\ T_{\mu\nu} &= \nabla_\mu\phi\nabla_\nu\phi - \frac{1}{2}g_{\mu\nu}(\nabla\phi)^2, \end{aligned}$$

$$E^{(\phi)} \equiv \nabla_\mu \nabla^\mu \phi + \lambda f'(\phi) \mathcal{G} = 0. \quad (3.3b)$$

In this work we will only consider the coupling function

$$f(\phi) = \phi. \quad (3.4)$$

While other coupling functions are often considered in the literature on EdGB black holes, this is the simplest which is thought to give rise to stable scalarized black hole solution; see [KMR⁺96, ea15, SZ14b, BSW16, WGPS19] and references therein. This coupling may additionally be motivated as the lowest order term in the effective field theory expansion of a metric theory coupled to a scalar field (e.g. [YSY16]). From the symmetry $\lambda \rightarrow -\lambda, \phi \rightarrow -\phi$, we only consider $\lambda \geq 0$.

We evolve this system in Painlevé-Gullstrand (PG)-like coordinates (e.g. [ABCL05, ZK09, KSH11, Rip19])

$$ds^2 = -\alpha(t, r)^2 dt^2 + (dr + \alpha(t, r)\zeta(t, r)dt)^2 + r^2 (d\vartheta^2 + \sin^2\vartheta d\varphi^2), \quad (3.5)$$

so-named since $t = \text{const.}$ cross sections are spatially flat (the Schwarzschild black hole in these coordinates is given by $\alpha = 1, \zeta = \sqrt{2m/r}$).

We define the variables

$$Q \equiv \partial_r \phi, \quad (3.6a)$$

$$P \equiv \frac{1}{\alpha} \partial_t \phi - \zeta Q, \quad (3.6b)$$

and take algebraic combinations of Eq. (3.3b) and the tr , rr , and $\vartheta\vartheta$ components of Eq. (3.3a) (c.f. [RP19a]) to obtain the following evolution equation for the $\{P, Q\}$ variables:

$$E_{(Q)} \equiv \partial_t Q - \partial_r (\alpha [P + \zeta Q]) = 0, \quad (3.7a)$$

$$E_{(P)} \equiv \mathcal{A}_{(P)} \partial_t P + \mathcal{F}_{(P)} = 0. \quad (3.7b)$$

The quantities $\mathcal{A}_{(P)}$ and $\mathcal{F}_{(P)}$ are lengthy expressions of $\{\alpha, \zeta, P, Q\}$ and their radial derivatives. Their (unenlightening) explicit forms are presented in the Appendix of

[RP20b]. In the limit $\lambda = 0$ Eq. (3.7b) reduces to

$$\partial_t P - \frac{1}{r^2} \partial_r (r^2 \alpha [Q + \zeta P]) = 0. \quad (3.8)$$

Interestingly, in PG coordinates the Hamiltonian and momentum constraints do not change their character as elliptic differential equations going from GR to EdGB gravity:

$$E_{\mu\nu}^{(g)} n^\mu n^\nu \propto \partial_r ((r - 8\lambda f' Q) \alpha^2 \zeta^2) - 8\lambda f' \frac{P}{\alpha} \partial_r (\alpha^3 \zeta^3) - r^2 \alpha^2 \rho = 0, \quad (3.9a)$$

$$\begin{aligned} E_{\mu r}^{(g)} n^\mu \propto & \left(1 - 8\lambda f' \frac{\zeta}{r} P - 8\lambda f' \frac{Q}{r} \right) \zeta \partial_r \alpha - \frac{1}{2} r \alpha j_r \\ & + 2\lambda f' \frac{Q}{r \alpha^2} \partial_r (\alpha^2 \zeta^2) + 4\lambda \frac{\zeta}{r} \partial_r (f' P) = 0, \end{aligned} \quad (3.9b)$$

where

$$\rho \equiv n^\mu n^\nu T_{\mu\nu} = \frac{1}{2} (P^2 + Q^2), \quad (3.10a)$$

$$j_r \equiv -\gamma_r^\mu n^\nu T_{\mu\nu} = -PQ, \quad (3.10b)$$

$f' \equiv df/d\phi$, and $n_\mu \equiv (-\alpha, 0, 0, 0)$. While Eqs. (3.9a) and (3.9b) hold for any f , as mentioned above we only consider $f(\phi) = \phi$ in this article.

3.3 Description of code and simulations

3.3.1 Diagnostics

As PG coordinates are spatially flat the Arnowitt-Deser-Misner mass prescription always evaluates to zero: the ADM mass does not provide a useful characterization of the “mass” of spacetimes in these coordinates. The Misner-Sharp mass [MS64] provides a convenient mass to use in spherical symmetry

$$m_{MS}(t, r) = \frac{r}{2} (1 - (\nabla r)^2) = \frac{r}{2} \zeta(t, r)^2. \quad (3.11)$$

evaluated at spatial infinity to define the spacetime mass (and this does give the correct mass for the Schwarzschild solution in GR)

$$m \equiv \lim_{r \rightarrow \infty} m_{MS}(t, r). \quad (3.12)$$

The Misner-Sharp mass can be thought of as the charge associated with the Kodama current, which is conserved in any spherically symmetric spacetime (regardless of whether the Einstein equations hold) [Kod80, MN08, AV10]. Going through this “derivation” of the Misner-Sharp mass, we find that we can think of $m_{MS}(t, r)$ as representing the radially integrated energy density of the following (conserved) stress-energy tensor for EdGB gravity [RP19a]

$$\mathcal{T}_{\mu\nu} \equiv -2\lambda\delta_{\alpha\beta\rho\sigma}^{\gamma\delta\kappa\lambda}R^{\rho\sigma}{}_{\kappa\lambda}(\nabla^\alpha\nabla_\gamma\phi)\delta_{(\mu}^\beta g_{\nu)\delta} + \nabla_\mu\nabla_\nu\phi - \frac{1}{2}g_{\mu\nu}(\nabla\phi)^2. \quad (3.13)$$

We are unaware of any other definition for a covariantly conserved stress-energy tensor that does not involve both the Riemann tensor and derivatives of the scalar field (besides the Einstein tensor itself, or a constant times the stress-energy tensor) in EdGB gravity. Clearly the standard definition of the scalar field stress-energy tensor, $T_{\mu\nu} \equiv \nabla_\mu\phi\nabla_\nu\phi - \frac{1}{2}g_{\mu\nu}(\nabla\phi)^2$ is not conserved as $\square\phi = \lambda\mathcal{G}$, and \mathcal{G} is generically not zero. We could add terms such as the Einstein tensor to the stress-energy tensor, but as those terms do not involve the scalar field ϕ there is no clear reason why they should be considered as part of the stress-energy tensor for the scalar field. We note that the stress-energy tensor 3.13 also conforms with earlier choices for the stress-energy tensor of EdGB gravity [KMR+96].

As described in the next section we compactify so that infinity is at a finite location on our computational grid. The asymptotic mass m is preserved up to truncation error in our simulations of both EdGB gravity and GR. Given a spacetime with mass m , we define the dimensionless curvature-coupling

$$C \equiv \frac{\lambda}{m^2}. \quad (3.14)$$

We will classify different solutions based on their curvature couplings C , with GR the limit $C = 0$; empirically (as we discuss in our results 3.4) we find strong EdGB corrections arising when $C \gtrsim 0.1$.

Following the procedure used in [RP19b, RP19a], we calculate the radial characteristics of the scalar degree of freedom via Eqs. (3.7a) and (3.7b), after having

removed the spatial derivatives of α and ζ from these equations using the constraints (3.9a, 3.9b). The corresponding characteristic speeds c_{\pm} are

$$c_{\pm} \equiv \mp \xi_t / \xi_r, \quad (3.15)$$

where $\xi_a \equiv (\xi_t, \xi_r)$ solves the characteristic equation

$$\det \left[\begin{pmatrix} \delta E_{(P)} / \delta (\partial_a P) & \delta E_{(P)} / \delta (\partial_a Q) \\ \delta E_{(Q)} / \delta (\partial_a P) & \delta E_{(Q)} / \delta (\partial_a Q) \end{pmatrix} \xi_a \right] = 0. \quad (3.16)$$

In the limit $\lambda = 0$, these speeds reduce to the radial null characteristic speeds in PG coordinates $c_{\pm}^{(n)}$

$$c_{\pm}^{(n)} \equiv \alpha (\pm 1 - \zeta). \quad (3.17)$$

We see that $\zeta = 1$ marks the location of a marginally outer trapped surface (MOTS) (we consider MOTS only for null surfaces; [Tho07] and references therein). We take the location of the MOTS to represent the size of the black hole on any given time slice.

The characteristic equation, Eq. (3.16), takes the following form when expressed as an equation for the characteristic speeds c

$$\mathcal{A}c^2 + \mathcal{B}c + \mathcal{C} = 0, \quad (3.18)$$

where

$$\mathcal{A} \equiv \frac{\delta E_{(P)}}{\delta (\partial_t P)} \frac{\delta E_{(Q)}}{\delta (\partial_t Q)} - \frac{\delta E_{(P)}}{\delta (\partial_t Q)} \frac{\delta E_{(Q)}}{\delta (\partial_t P)}, \quad (3.19a)$$

$$\begin{aligned} \mathcal{B} \equiv & - \left(\frac{\delta E_{(P)}}{\delta (\partial_t P)} \frac{\delta E_{(Q)}}{\delta (\partial_r Q)} - \frac{\delta E_{(P)}}{\delta (\partial_t Q)} \frac{\delta E_{(Q)}}{\delta (\partial_r P)} \right) \\ & - \left(\frac{\delta E_{(P)}}{\delta (\partial_r P)} \frac{\delta E_{(Q)}}{\delta (\partial_t Q)} - \frac{\delta E_{(P)}}{\delta (\partial_r Q)} \frac{\delta E_{(Q)}}{\delta (\partial_t P)} \right), \end{aligned} \quad (3.19b)$$

$$\mathcal{C} \equiv \frac{\delta E_{(P)}}{\delta (\partial_r P)} \frac{\delta E_{(Q)}}{\delta (\partial_r Q)} - \frac{\delta E_{(P)}}{\delta (\partial_r Q)} \frac{\delta E_{(Q)}}{\delta (\partial_r P)}. \quad (3.19c)$$

Where the discriminant $\mathcal{D} \equiv \mathcal{B}^2 - 4\mathcal{A}\mathcal{C} > 0$ are regions of spacetime where the equations are hyperbolic, where $\mathcal{D} < 0$ the equations are elliptic, and following the

language of mixed-type PDEs (e.g. [Otw15] and references therein), the co-dimension one surfaces where $\mathcal{D} = 0$ separating elliptic and hyperbolic regions are called sonic lines. In the GR limit $\lambda = 0$ the scalar equations are always hyperbolic ($\mathcal{D} > 0$), though as we found in [RP19b, RP19a], for sufficiently strong couplings C the discriminant \mathcal{D} is not of definite sign, and the scalar equations are then of mixed-type (similar conclusions have been drawn for other member of the Horndeski class of theories; see e.g. [LZKM11, AGS11, BLL19]). As we are working in spherical symmetry, the tensor degrees of freedom are pure gauge. Our hyperbolicity analysis can thus be thought of as applying to the scalar “sector” of EdGB gravity³.

3.3.2 Spatial compactification

In vacuum when $P = Q = 0$, the general solution to Eqs. (3.9a) and (3.9b) is $\zeta \propto r^{-1/2}$ and $\alpha = \text{const.}$ ⁴. We found that this falloff in ζ made it difficult to impose stable outer boundary conditions at a fixed, finite r . To alleviate this problem, we spatially compactify through a stereographic projection

$$r \equiv \frac{x}{1 - x/L}, \quad (3.20)$$

where L is a constant, and discretize along a uniform grid in x , with spatial infinity $x = L$ now the outer boundary of our computational domain. For all the simulations presented in this article we chose $L = 5m$, where m is the mass of the initial Schwarzschild black hole. At $x = L$ we impose the conditions $\alpha|_{x=L} = 1$, $\zeta|_{x=L} = 0$, $P|_{x=L} = 0$, $Q|_{x=L} = 0$, $\phi|_{x=L} = 0$. These conditions are consistent with our initial conditions and asymptotic fall off of the metric and scalar field. For the latter, generally $\phi \rightarrow 1/r$, though if we impose exact Schwarzschild initial data outside some

³Note that generically in a less symmetrical spacetime it may not always be possible to distinguish between scalar and tensor dynamics or “sectors” due to the derivative coupling between the scalar and metric fields in the EdGB equations of motion; see Eqs. 3.3.

⁴In EdGB gravity curvature always sources a scalar field, though for $r \gg m$ for an isolated source in an asymptotically flat spacetime, the fall off of the curvature-sourced scalar field is sufficiently fast not to alter, through back reaction, the fall off of the metric derived when $P = Q = 0$.

radius r_1 (such that $\phi(r > r_1, t = 0) = 0$ and $\partial_t \phi(r > r_1, t = 0) = 0$), the Gauss-Bonnet curvature will source an asymptotic field that decays like $1/r^4$; by causality (as long as the equations are hyperbolic) the $1/r$ component sourced by the black hole, or any scalar radiation from a field we put in at $r < r_1$, will never reach spatial infinity. We note that in principle it is possible that even with finite characteristic speeds, some scalar field could approach $x = L$ at the level of truncation error. As we exactly impose $\phi = 0$ at $x = L$ though, with Kreiss-Oliger dissipation these effects should not affect our simulations, and should converge away with higher resolution.

3.3.3 Initial data

The computational domain covers $x \in [x_{exc}, L]$ ($r \in [r_{exc}, \infty]$), where x_{exc} (r_{exc}) is the excision radius, and can vary with time (described in the following section). We set initial data at $t = 0$ by specifying the values of P and Q , and then solve for α and ζ using the momentum and Hamiltonian constraints. These ordinary differential equations (ODEs) are discretized using the trapezoid rule and solved with a Newton relaxation method, integrating from $x = x_{exc}$ to $x = L$. At $x = x_{exc}$ (some distance inside the horizon, as discussed in the next section) we set α and ζ to their Schwarzschild values:

$$\alpha|_{t=0, x=x_{exc}} = 1, \quad \zeta|_{t=0, x=x_{exc}} = \sqrt{\frac{2m}{r(x_{exc})}}. \quad (3.21)$$

If we begin with zero scalar field energy ($Q|_{t=0} = P|_{t=0} = 0$), solving the constraints recovers the Schwarzschild solution on $t = 0$ to within truncation error.

3.3.4 Excision

At every time step we solve for α , ζ , P , and Q by alternating between an iterative Crank-Nicolson solver for P and Q and the ODE solvers for α and ζ , until the discrete infinity norm of all the residuals are below a pre-defined tolerance (typically the tolerance was $\lesssim 10^{-10}$, smaller than the typically size of the one-norm (L_1) of

the independent residuals. This is a similar strategy to that used in our earlier code based on Schwarzschild-like coordinates, and more details can be found in [RP19a]). The excision strategy assumes all characteristics of hyperbolic equations are pointing out of the domain at the excision surface $x = x_{exc}$. This implies that for P and Q we cannot set boundary conditions there, rather their evolution equations must be solved, with the finite difference stencils for the radial derivatives appropriately changed to one-sided differences. For α , as with the initial data, the inner boundary condition is arbitrary, and after each iteration we rescale it so that $\alpha(t, x = L) = 1$. For ζ , to obtain a consistent solution to the full field equations requires that the boundary condition $\zeta(t, x = x_{exc})$ be set by solving the corresponding evolution equation for ζ there (optionally ζ could be evolved over the entire domain using this equation). Taking algebraic combinations of the equations of motion (3.3a), an appropriate evolution equation for ζ can be obtained

$$\mathcal{A}_{(\zeta)}\partial_t\zeta + \mathcal{F}_{(\zeta)} = 0, \quad (3.22)$$

The expressions for $\mathcal{A}_{(P)}$ and $\mathcal{F}_{(P)}$ are lengthy expressions of λ , $\{\alpha, \zeta, P, Q\}$, and their radial derivatives. Their full form may be found in the Appendix of [RP20b]. In the limit $\lambda = 0$, Eq. (3.22) reduces to

$$\partial_t\zeta - \alpha\zeta\partial_r\zeta - \frac{\alpha}{2r}\zeta^2 - \frac{r}{2\zeta}T_{tr} = 0. \quad (3.23)$$

Eq. (3.22) provides the boundary condition for ζ at the excision surface. We then integrate outwards in r using the Hamiltonian constraint, Eq. (3.9a) as described above to solve for ζ .

The formation of a MOTS is signaled by $\zeta = 1$ (Eq. (3.17)), and we always place the excision surface inside the MOTS⁵. The location of x_{exc} is updated every time step before solving for the scalar and metric fields. The location of the excision point

⁵In all cases we have considered we find that the ‘‘characteristic horizon’’ (the location where $c_+ < 0$ for the EdGB scalar field) is exterior to the MOTS, so placing the excision point interior to the MOTS should lead to well posed evolution, provided the equations of motion for the EdGB scalar remain hyperbolic.

is chosen so that it is always interior to the MOTS, but lies exterior to (or directly on) the sonic line (for further discussion see Sec. 3.3.1 and Sec. 3.4.4). The location for r_{exc} on our initial data slice depended on the strength of the curvature coupling C , which we detail in our Results, Sec. 3.4.

3.3.5 Fixed mesh refinement with a hyperbolic-ODE system

To achieve the necessary long term accuracy over thousands of m in evolution using limited computational resources, we evolved some simulations using a Berger and Olinger (BO) style mesh refinement algorithm [BO84]. Due to the nature of our initial data and perturbations, a fixed hierarchy suffices, with the higher resolution meshes confined to smaller volumes centered about the origin. For those runs, we typically used 4 additional levels beyond the base (coarsest) level, with a 2 : 1 refinement ratio between levels; specifically, we set the inner boundary for all levels at x_{exc} , and the outer refinement boundary locations at $x_l/m = \{5.00, 2.30, 2.00, 1.75, 1.55\}$, from coarsest to finest (the initial horizon location $r = 2m$, and we chose the excision radius x_{exc} so that $r_{exc}(x_{exc}) = 0.8 \times 2m$; see Eq. (3.20)).

In Appendix B we present a more detailed description of the mesh refinement algorithm, a description of an adaptive mesh extension of it, and discuss ways in which it could be improved.

3.4 Scalarized black holes: numerical results

3.4.1 Overview of simulations and plots

To help keep track of the various simulation results we present, we collect some of our simulation parameters in Table. (3.1). We found for long time evolution simulations ($t \gtrsim 10^3 m$) fixed mesh refinement was essential to maintain high accuracy evolution ($\delta m/m \lesssim 10^{-2}$). Unigrid evolution was sufficient for shorter simulation runs. When

Figure	grid layout	Δx	CFL number	initial data
2,3,4,5,6,12	FMR	0.38	0.25	Schwarzschild
7	unigrid	0.024	0.5	Schwarzschild with bump: $\phi_0 = 0.1, a = 45, b = 55.$
8	unigrid	0.012	0.2 and 0.1	Schwarzschild
9	unigrid	0.049	0.2	Schwarzschild
10	unigrid	0.049	0.4	Schwarzschild
11	unigrid	0.012	0.2	Schwarzschild

Table 3.1: Simulation parameters. “FMR” means “fixed mesh refinement”. Grid resolution Δx refers to the base grid resolution for the fixed mesh refinement runs. A discussion of Schwarzschild initial data can be found in Sec. 3.4.2, and a discussion of “Schwarzschild with bump” initial data can be found in Sec. 3.4.3. See also Sec. 3.4.1.

we quote a value of resolution Δx , it represents the resolution of the coarsest (base) level if fixed mesh refinement was used, otherwise it is the resolution of the unigrid mesh. We found that stably resolving the initial growth of the sonic line that formed inside the EdGB black hole required using smaller Courant-Friedrichs-Lewy (CFL) numbers, but CFL numbers as large as 0.5 led to stable evolution if we excised well away from the sonic line.

3.4.2 Growth of “hair” from Schwarzschild initial data

For most of our simulations we begin with a ($t = \text{const.}$) slice of the Schwarzschild black hole solution in PG coordinates; which is (as is any spacelike slice of Schwarzschild) an *exact* solution to the initial value problem in EdGB gravity. Specifically, at $t = 0$, for $x > x_{exc}$ (the initial excision radius as described in Sec. 3.3.4), we set

$$\phi|_{t=0} = 0, \quad Q|_{t=0} = 0, \quad P|_{t=0} = 0, \quad \alpha|_{t=0} = 1, \quad \zeta|_{t=0} = \sqrt{\frac{2m}{r}}. \quad (3.24)$$

We then evolve this, performing a survey of outcomes varying the EdGB coupling parameter λ (in the GR case $\lambda = 0$, as expected, the resultant numerical solution is static to within truncation error).

Previous studies of static scalarized black hole solutions in EdGB gravity have found that regularity of the scalar field at the horizon places an upper limit on the

coupling parameter. For the linear coupling case we consider, this is (see e.g. [SZ14b])

$$\frac{\lambda}{r_h^2} \leq (192)^{-1/2} \approx 0.07, \quad (3.25)$$

where r_h is the areal radius of the horizon. For black holes much larger than this, $r_h \approx 2m$ (the space time is close to Schwarzschild), though approaching the extremal limit a non-negligible amount of the spacetime mass m can be contained in the scalar field, and simply replacing r_h with $2m$ to express the above in terms of our curvature-coupling parameter C (3.14) gives a poor estimate of the corresponding extremal value C_{extr} . From Figure 4 of [SZ14b] we can infer a more accurate translation :

$$C \leq C_{extr} \approx 0.22. \quad (3.26)$$

We find the extremal limit is not characterized by the appearance of a naked curvature singularity, but instead the formation of a sonic line (and elliptic region) outside of the horizon of the black hole. Our measured extremal limit of $C_{extr} \sim 0.23$, as shown in Sec. 3.4.4, is quite close to the above limit from [SZ14b].

Note that the “extremal limit” for a scalarized EdGB black hole is of a different nature than the extremal limits of Kerr or Reissner-Nordstrom black holes. The spin or electric charge of a black hole is set by the black hole’s formation history: black holes of the same mass can have different spins or charges depending on the initial configuration and net charge and angular momentum of the matter that fell in to form the black hole. By contrast for an EdGB black hole the final scalar charge is set by the Gauss-Bonnet coupling, and Gauss-Bonnet curvature at the horizon, independent of its formation history [KMR+96, SZ14b].

Given that the Schwarzschild solution, of any mass, is valid initial data in EdGB gravity, we can certainly begin with superextremal black holes in our evolution (and again to be clear, here we use the term “superextremal” to refer to $C > C_{extr}$; there is no spin or charge in our numerical solutions). As we show below however, these develop elliptic regions outside the horizon. Moreover, our results in [RP19b, RP19a] show that trying to form a superextremal black hole from gravitational collapse of

the dilaton field (in spherical symmetry) will result in an elliptic region appearing before a horizon. This suggests superextremal black holes in EdGB gravity exist in the regime of the theory governed by mixed-type equations, and their presence or “formation” (however that could be interpreted in a mixed-type problem) would mark a breakdown of the Cauchy problem. Also note that failure of the Cauchy problem is not *a priori* connected to regions of strong curvature or black hole formation; as further shown in [RP19b, RP19a], strong coupling and mixed-type character can be present for arbitrarily small spacetime curvature.

We first present results from evolution of Schwarzschild black hole initial data, and curvature couplings below the extremal limit. In all cases, if we move our excision radius sufficiently far interior to the horizon, we find that at some time an elliptic region forms in the interior. However, for these cases we can choose an excision radius closer to the horizon so that the evolution settles to a stationary state without any elliptic region forming in this new domain. As discussed in the introduction, we view this as a consistent initial boundary value evolution of EdGB gravity where the elliptic region is “censored” from the exterior hyperbolic region. In Figs. 3.3 and 3.4 we show examples of scalar hair growth for these cases (with the elliptic region excised), and their difference from the static “decoupled” scalar field profiles for a Schwarzschild black hole background (see Appendix D), for various curvature-couplings. These runs employed the fixed mesh refinement algorithm described above, with the base level grid having $\Delta x = 0.39$ resolution, Courant-Friedrichs-Lewy (CFL) number of 0.25, and an excision radius at fixed at $r_{exc} = 0.95 \times 2m$. We find the scalar field settles down to solutions that differ little from the static decoupled scalar field profile, although the difference grows as the curvature coupling approaches the extremal limit (c.f. Fig. 3 of [SZ14b]). Nevertheless, in agreement with the results of [SZ14b], the difference of the full solution from the static decoupled limit solution remains small outside the black hole horizon. From convergence studies we find we can resolve the difference of the scalar field profile from its decoupled value well within truncation error; see

Fig. 3.7. For the case $C = 0.16$, in Fig. 3.8 we show growth of Ricci curvature sourced by the scalar field, and in Fig. 3.9 a corresponding plot of convergence and estimated truncation error in R .

3.4.3 Perturbed Schwarzschild initial data

Schwarzschild initial data is not generic; in particular, the scalar field is (initially) only growing in response to the Gauss-Bonnet curvature source. To investigate a slightly broader class of initial conditions, here we add a small, mostly ingoing propagating perturbation to ϕ outside the horizon:

$$\phi(t, r)|_{t=0} = \begin{cases} \phi_0 \exp\left[-\frac{1}{(r-a)(b-r)}\right] \exp\left[-5\left(\frac{r-(a+b)/2}{a+b}\right)^2\right] & a < r < b \\ 0 & \text{otherwise} \end{cases}, \quad (3.27a)$$

$$Q(t, r)|_{t=0} = \partial_r \phi(t, r)|_{t=0}, \quad (3.27b)$$

$$P(t, r)|_{t=0} = 0. \quad (3.27c)$$

This family of initial data (rescaled “bump functions” multiplied by a Gaussian) is smooth and compactly supported outside the initial black hole horizon for $a > 2m$. With a fixed curvature-coupling C , we find that we can stably evolve an initial black hole plus scalar field bump if the amplitude of the latter is sufficiently small; or equivalently if the metric curvature measured by the Ricci scalar R induced by the scalar field bump is sufficiently small. For our initial data for α and ζ , we set their values at the excision surface as in Eq. (3.24), and then integrate outwards in r . An example of such a case is shown in Fig. 3.10. When the induced curvature is large, an elliptic region forms outside the black hole horizon (and soon after that the code crashes). As a rough estimate, we find this occurs when $|R \times \lambda|_\infty \gtrsim 0.1$. This result is consistent with our earlier findings of collapse of a scalar field pulse without any interior black hole [RP19b, RP19a].

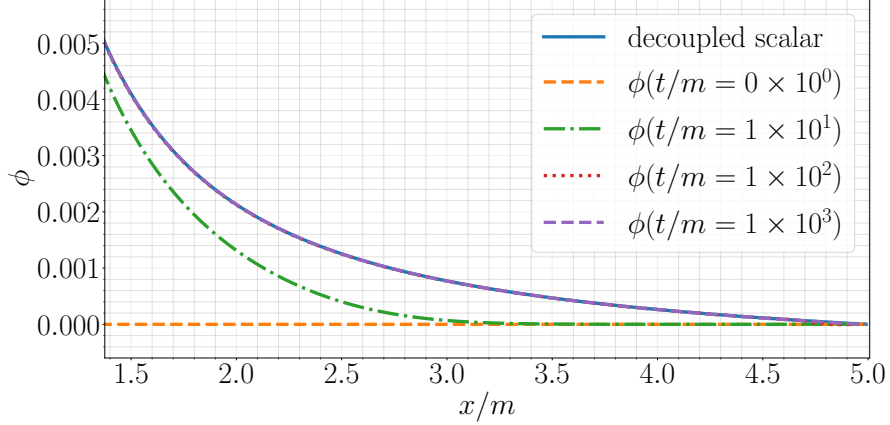


Figure 3.1: $C = 2.5 \times 10^{-3}$

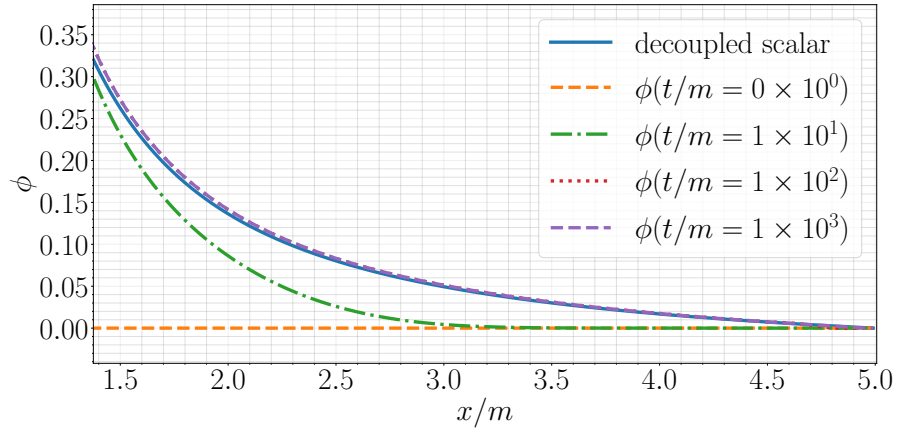


Figure 3.2: $C = 0.16$

Figure 3.3: Growth of scalar “hair” from Schwarzschild initial data. Shown is the scalar field profile at several times during an evolution for two different cases of the curvature coupling C (3.14); the extremal limit (see the discussion in Sec. 3.4.2) is $C_{extr} \approx 0.23$. The horizon (MOTS) is located at $x_h/m \approx 1.48$, and spatial infinity is at $x/m = 5$. Notice the different range of scales on the y-axis of each figure. Also shown for comparison is the estimate of the final profile using the decoupled scalar approximation (Appendix D); see also Fig. 3.4. For simulation parameters see Table. 3.1.

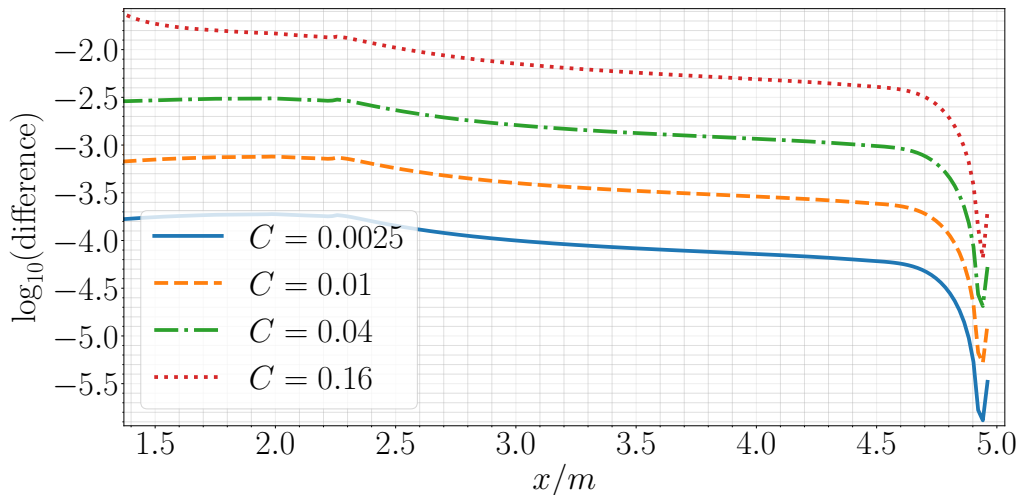


Figure 3.4: Difference between the late time ($t \sim 2000m$) scalar field profile obtained from the non-linear simulations to that of the decoupled estimate (see Appendix D), for several values of the curvature coupling C ; see also Fig. 3.3. The black hole horizon (MOTS) is at $x/m \approx 1.48$, and spatial infinity is at $x/m = 5$. As expected, the decoupling limit approximation improves the further C is away from the extremal limit $C_{extr} \sim 0.23$. For simulation parameters see Table. 3.1.

3.4.4 Internal structure of an EdGB black hole, and the near extremal limit

For small values of the curvature coupling we can consistently excise any elliptic region that forms interior to the horizon. We always excise the Schwarzschild curvature singularity at $r = 0$, and in none of the cases we have run (small or large curvature coupling) do we see any signs of a curvature or scalar field singularity forming away from $r = 0$ while the equations remain hyperbolic. We can typically evolve for some time after an elliptic region forms without excising it before the code crashes, however this as an artifact of finite resolution, and we can only expect convergence to the continuum limit using our hyperbolic scheme until the first appearance of the sonic line. In other words, to say anything rigorous about what might occur within the elliptic region would require solving a mixed-type problem, and we do not have the tools for doing so.

With increasing values of the curvature coupling approaching the extremal limit

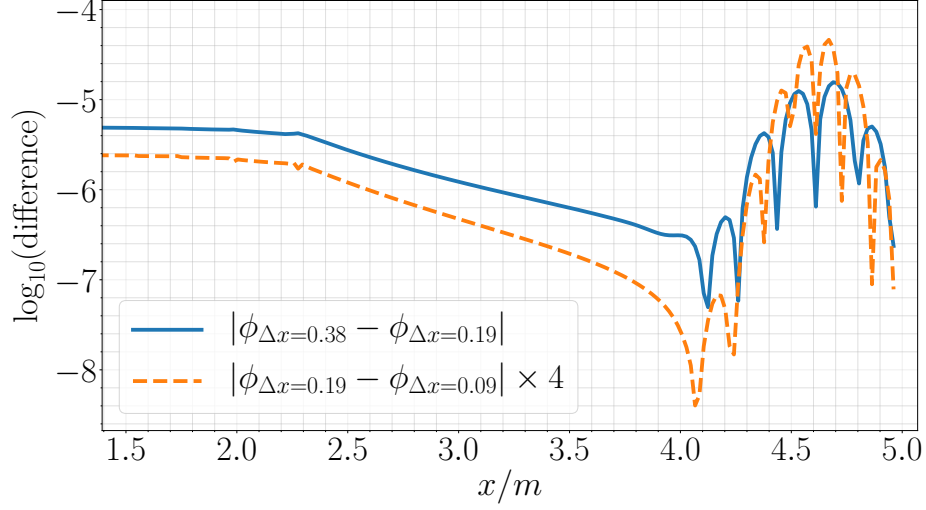


Figure 3.5: $C = 2.5 \times 10^{-3}$

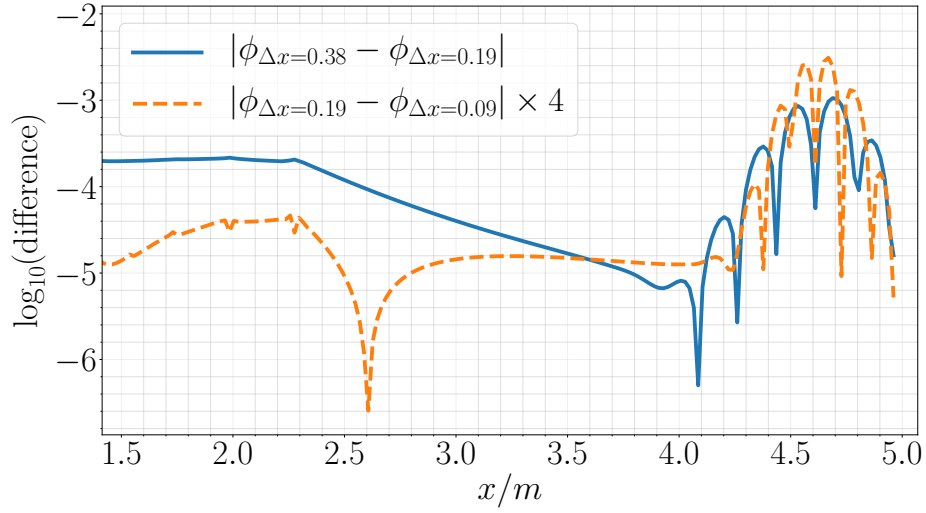


Figure 3.6: $C = 0.16$

Figure 3.7: Convergence and truncation error estimate at $t \sim 100m$ for the scalar field ϕ . Shown are point-wise differences of the solution computed with different resolutions; the decrease going to successively higher resolutions is consistent with second order convergence, and the magnitude for a given pair is an estimate of the error in the scalar field profile at those resolutions. Comparing with Fig. 3.4, we see we can resolve the difference of the scalar field from the decoupled value well above truncation error for the range of curvature-couplings considered here. We rescale the smaller truncation error estimate by 4, which is the expected convergence rate of our code based on the order of the second order finite difference stencils we use. For simulation parameters see Table. 3.1.

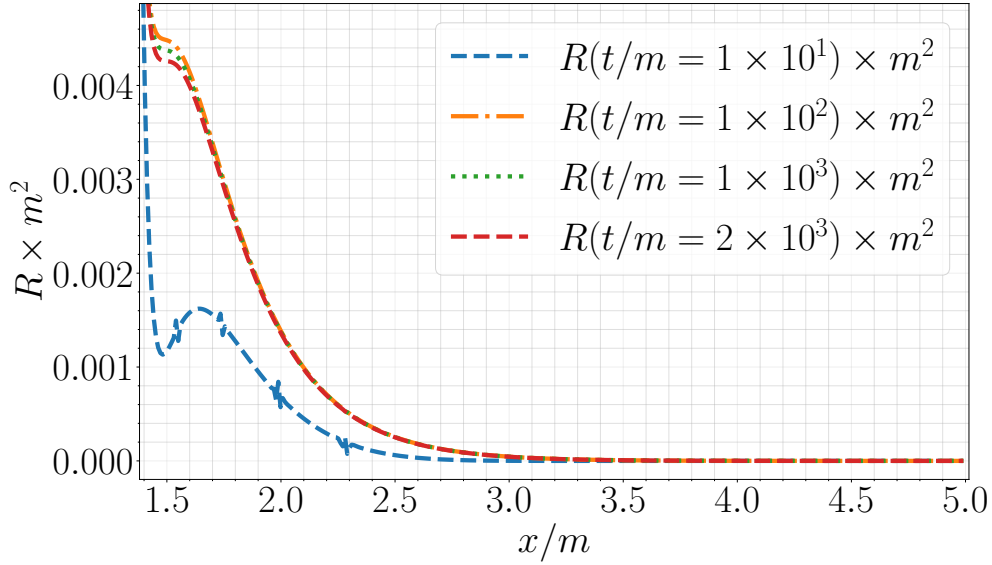


Figure 3.8: Evolution of the Ricci scalar for the case $C = 0.16$; see Fig. 3.3 for evolution of the scalar field for this same simulation. The small “features” in the Ricci scalar at the $t = 10m$ time slice are located at grid refinement boundaries, and converge away with higher base resolution (compare with Fig. 3.9). For simulation parameters see Table. 3.1.

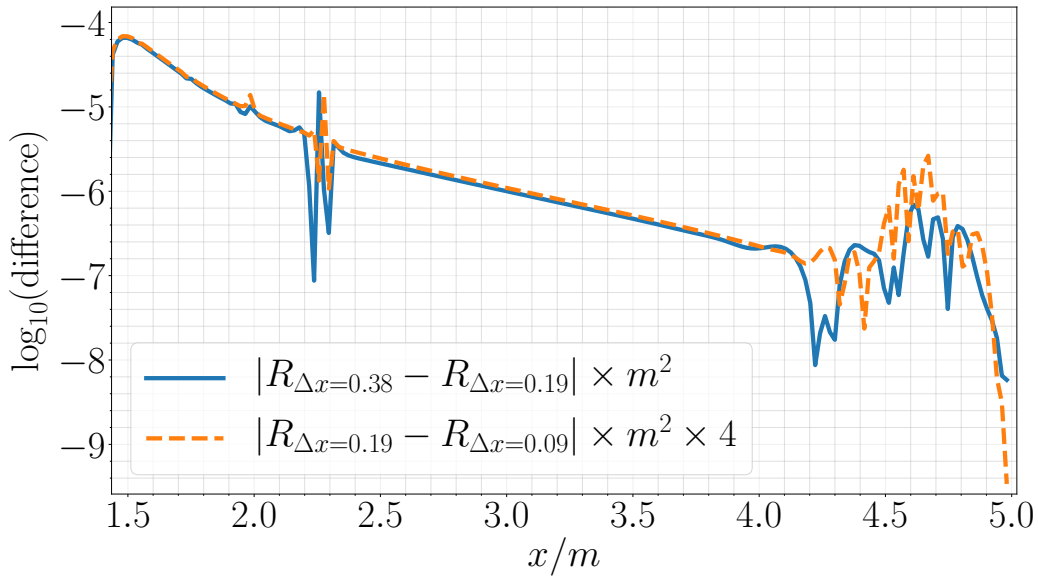


Figure 3.9: Convergence and truncation error estimate at $t \sim 100m$ for the Ricci scalar R , for the $C = 0.16$ case (see Fig. 3.7 for a similar plot of the scalar field ϕ for this case, and the caption there for a discussion of the error estimates). The oscillations near $x/m \sim 2.3$ are at grid refinement boundary. We rescale the smaller truncation error estimate by 4, which is the expected convergence rate of our code based on the order of the second order finite difference stencils we use. For simulation parameters see Table. 3.1.

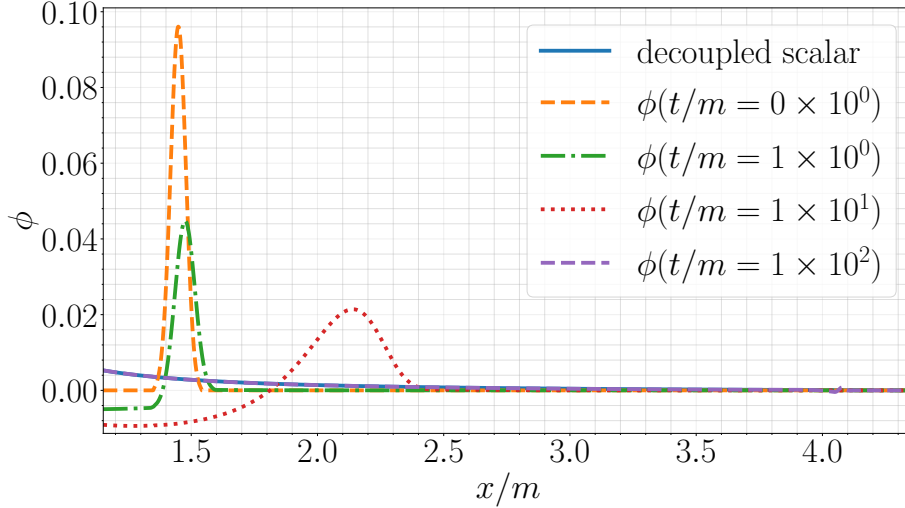


Figure 3.10: Schwarzschild initial data perturbed by an EdGB scalar bump (see Eq. (4.23a)) outside the horizon. The mass of the initial Schwarzschild black hole is $m_s = 20$, while the scalar bump adds an additional ~ 3 in mass, giving a net mass $m = 23$; thus with $\lambda = 1$ the curvature coupling is $C = \lambda/m^2 \approx 2 \times 10^{-3}$. Some of the scalar field falls into the black hole, while some disperses to infinity, and at late times the scalar field approaches the decoupled scalar field profile. For simulation parameters see Table. 3.1.

(3.26), as the scalar field grows, the location at which the sonic line first appears moves closer to the MOTS. Prior to this, we excise some distance within the MOTS, though when the sonic line appears we increase the excision radius to be at the sonic line ⁶. We then employ a “high water mark” strategy during subsequent evolution, increasing the excision radius to match the location of the sonic line if it grows, though do not reduce the excision radius if the sonic line shrinks (presumed to be happening if the characteristic discriminant on the excision boundary increases in magnitude away from zero).

For cases where the elliptic region remains censored, we typically find that initially the sonic line does grow, and then (presumably) shrinks within the excision radius

⁶The scalar and null characteristics are generally different from each other in EdGB gravity. For our excision strategy to be stable, we require all of the metric and scalar characteristics to point into the excised region. In all cases we have studied, the scalar characteristics always are not tangent to the sonic line (the characteristics can be defined up to the sonic line, which is also why we classify the EdGB equations as Tricomi type here [RP19b, RP19a]). Thus excising on the sonic line should be fine, as long as it remains within the horizon.

as the solution settles to a stationary state. For interest, we estimate the location of the sonic line by extrapolation, as follows. Recall, the equation for the radial characteristics is (Eq. (3.16))

$$\mathcal{A}c^2 + \mathcal{B}c + \mathcal{C} = 0, \quad (3.28)$$

where $\mathcal{A}, \mathcal{B}, \mathcal{C}$ are functions of α, ζ, P, Q , and their radial derivatives. The characteristics thus satisfy

$$c_{\pm} = \frac{1}{2\mathcal{A}} \left(-\mathcal{B} \pm \sqrt{\mathcal{B}^2 - 4\mathcal{A}\mathcal{C}} \right), \quad (3.29)$$

and the location of the sonic line is at the zero of the discriminant, $\mathcal{D} \equiv \mathcal{B}^2 - 4\mathcal{A}\mathcal{C}$. After excising, if \mathcal{D} becomes positive definite within the computational domain, we estimate the location of the sonic line as the zero of a quadratic polynomial fitted to the function

$$c_+ - c_- = \frac{1}{\mathcal{A}} \sqrt{\mathcal{B}^2 - 4\mathcal{A}\mathcal{C}}, \quad (3.30)$$

using a set of points adjacent to the excision boundary. In typical cases for Schwarzschild initial data, and subextremal curvature couplings, this estimate suggests the true location of the final stationary sonic line lies within $\sim 94\%$ of its maximum value (the excision point with respect to r); see Fig. 3.11 for a survey of the late time values of the excision radius, MOTS location and sonic line estimate, and Fig. 3.12, for the evolution of these quantities for one example (including several resolutions). In the latter figure, the shrinking of the MOTS after some initial growth coincides with violation of the null convergence condition ($R_{\mu\nu}k^{\mu}k^{\nu} \geq 0$ for all null vectors k^{μ} ; see e.g. [HE75]), which is known to occur in EdGB gravity (for more details in the spherical collapse problem see [RP19a]). A plot of $R_{\mu\nu}k^{\mu}k^{\nu}$ is shown in Fig. 3.13. We note that the stable violation of the Null Convergence Condition (NCC) is thought to be a key ingredient in the construction of singularity free cosmological and black hole solutions (for a review, see e.g. [Rub14]). This violation of the NCC appears to be transient: as the scalarized black hole settles to a stationary solution, we find the horizon stops

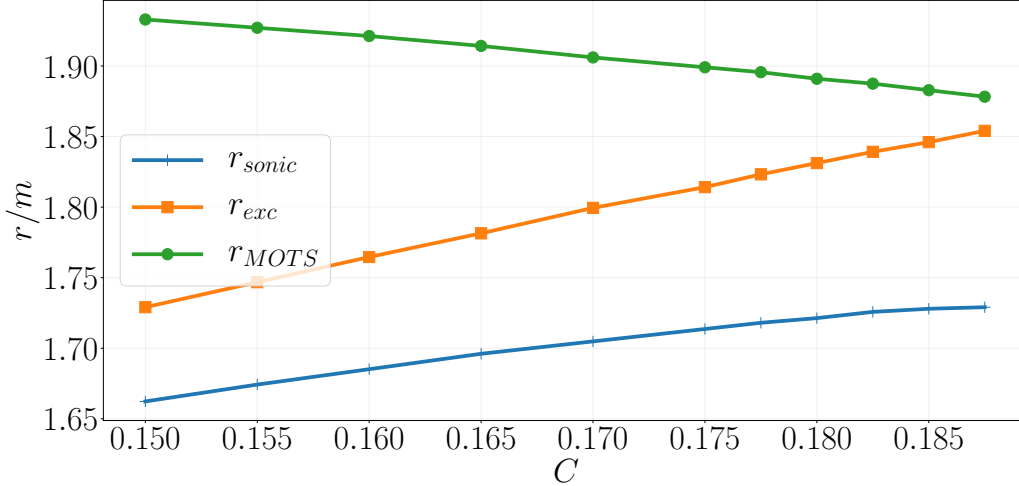


Figure 3.11: The location of the MOTS r_{MOTS} , excision radius r_{exc} , and *estimated* sonic line position r_{sonic} , as a function of the curvature coupling C , measured at $t \sim 80m$ during the evolution of Schwarzschild initial data, which is sufficiently late to give a good estimate of their static end state values (see Fig. 3.12). Due to our high water mark excision strategy, the excision point represents the largest measured radius the sonic line attained during evolution. Extrapolating the curves for the MOTS and sonic lines, we estimate the “extremal” coupling for our initial data to be $C_{extr} \sim 0.23$. These results were obtained with unigrid evolution using $\Delta x = 0.012$ (corresponding to the highest resolution curves shown in Fig. 3.12). For $C \geq 0.17$ runs the CFL number was 0.2, while for $C < 0.17$ the CFL number was 0.1. For other simulation parameters see Table. 3.1.

shrinking and the region of NCC violation disappears. The slow increase in the horizon size for $t/m \gtrsim 50$ is due to numerical error; we find it converges to zero with increasing resolution.

For curvature couplings above C_{extr} , the sonic line can move outside the MOTS, or initially appear outside it. Linearly extrapolating the data shown in Fig.3.11 to the location where the late time MOTS will cross the sonic line, we estimate $C_{extr} \sim 0.23$, close to but slightly larger than the value $C_{extr} \sim 0.22$ coming from seeking exactly static EdGB black hole solutions with a non-singular ϕ field on the horizon[SZ14b] (though even beyond caveats with our extrapolations, we do not expect these two methods to give identical numerical values for an extremal coupling). In Fig. 3.14 we show an example evolution of Schwarzschild initial data with superextremal curvature coupling. We see the sonic line quickly overtakes the black hole horizon, leading to a

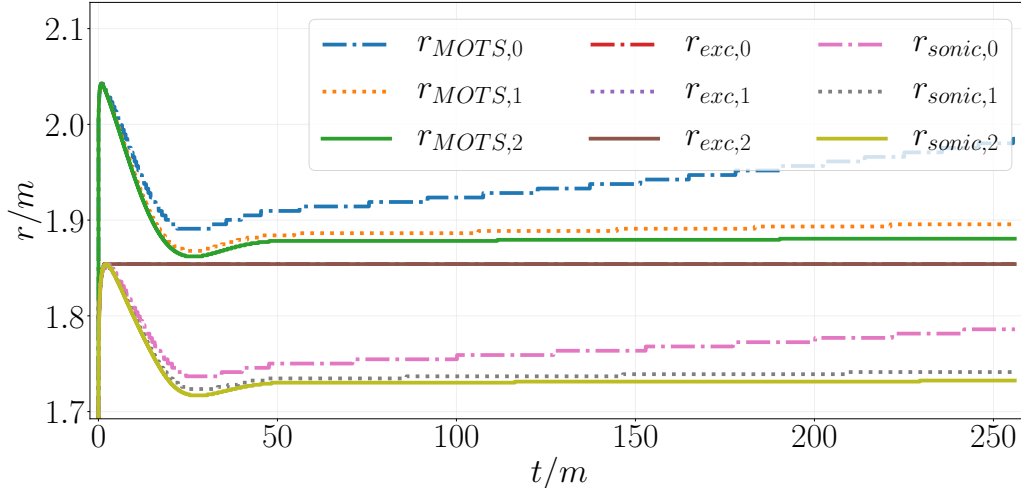


Figure 3.12: Evolution of the MOTS, excision point, and sonic line as a function of time, for curvature coupling $C = 0.1875$ (c.f. Fig. 3.11), and from runs at three resolutions : the labels 0, 1, 2 refer to unigrad resolutions $\Delta x = 0.049$, $\Delta x = 0.024$, and $\Delta x = 0.012$, respectively (a CFL factor of 0.2 was used in all cases). At early times as the sonic line grows, we increase the location of the excision surface to match; after reaching a maximum radius, the sonic line presumably starts to shrink again, and then the curves in the figure show an estimate of this location based on extrapolation of the characteristic speeds (see Sec. 3.4.4). The resolution study demonstrates that at late times we are converging to a static solution (in the vicinity of the horizon). For other run parameters see Table. 3.1.

“naked” elliptic region.

3.5 Discussion

In this article we have presented numerical evidence that in spherical symmetry, and for sufficiently small curvature couplings (what we call subextremal), EdGB black holes are nonlinearly stable. For subextremal couplings even moderately close to the extremal limit, solving the decoupled scalar equation for the scalar field profile provides a good fit to the numerical solution obtained in the full theory. Beginning from Schwarzschild initial data, instead of developing a non-central curvature singularity in the interior as was found for static solutions [SZ14b], we find the formation of a sonic line and elliptic region in the interior. Our treatment of the EdGB equations as hyperbolic does not allow us to conclude anything about possible extensions of the

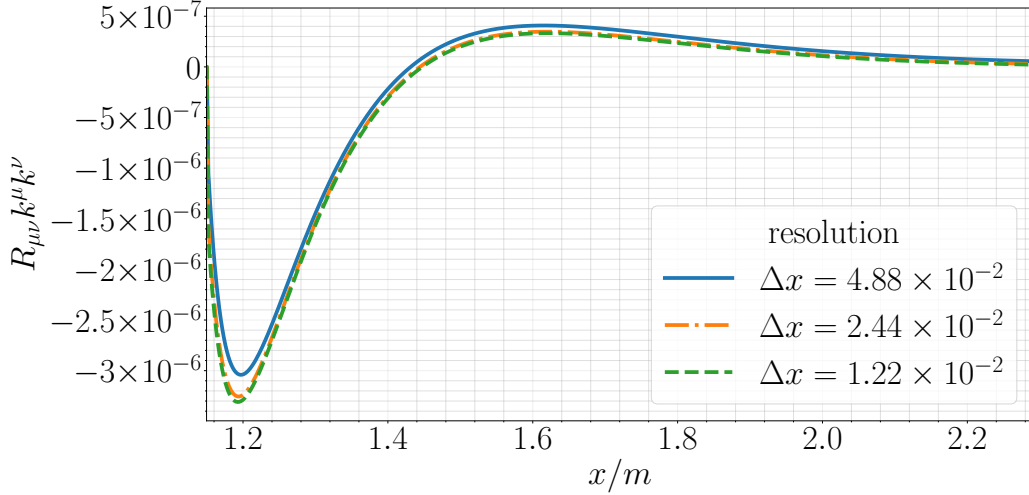


Figure 3.13: Ricci tensor contracted with outgoing null vector $k^\mu = (1, \alpha(-1 + \zeta), 0, 0)$ ($R_{\mu\nu}k^\mu k^\nu$) at time $t/m = 14$. The curvature coupling $C = 0.16$. We see that the null convergence factor is not positive definite; where it is negative indicates a region of NCC violation. The region of NCC violation is localized near the black hole horizon and region of strongest scalar field growth. This resolution study demonstrates we can resolve the stable violation of the null convergence condition in EdGB gravity during the formation of a scalarized black hole solution. For simulation parameters see Table. 3.1.

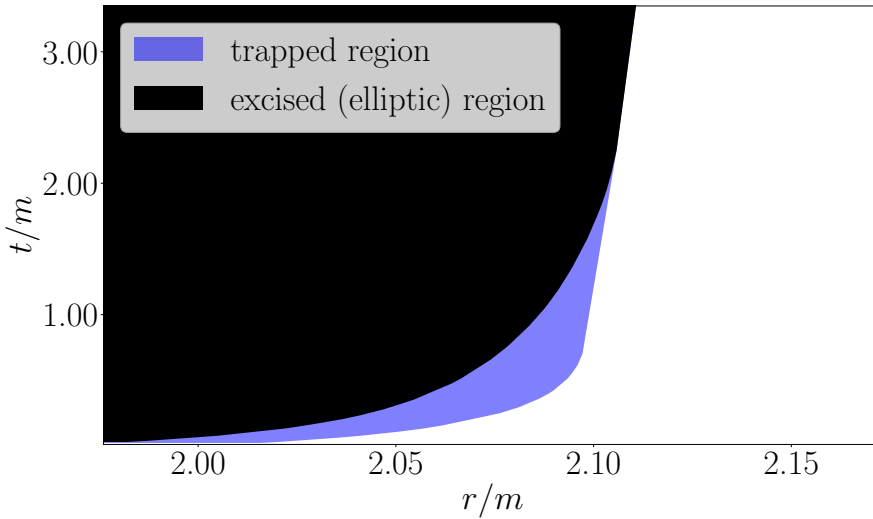


Figure 3.14: Example evolution of Schwarzschild initial data with superextremal curvature coupling: $C = 0.275$. We excise along the sonic line, so the excised region can be thought of as the elliptic region. The sonic line very quickly reaches and overtakes the MOTS, and the elliptic region subsequently becomes “naked”, shortly after which the code crashes. We note our code crashes if we do not excise the elliptic region, regardless if it is interior or exterior to the black hole horizon. For simulation parameters see Table. 3.1.

spacetime into the elliptic region. For subextremal black holes, our statement about their stability relates to the region exterior to the horizon, and assumes that our excision strategy used to eliminate the interior elliptic region is self-consistent (which is supported by the stability/convergence of the corresponding numerical evolutions). For superextremal cases, the sonic line forms or evolves to be outside the horizon, meaning we cannot excise it, and we would need to treat the exterior equations as mixed-type to obtain sensible solutions (or said another way, then the exterior evolution ceases to satisfy a well-posed Cauchy initial value problem). The particular value of the curvature coupling we find for the extremal limit is similar to, but slightly different from that given for static EdGB black holes solutions [KMR⁺96, SZ14b]; this is not particularly surprising given we are dynamically forming them from Schwarzschild initial data.

There are various ways in which this work could be extended. One is to explore a wider class of initial conditions; for example, collapse to a black hole from a regular matter source, whether the pure EdGB scalar field as in [RP19a], or coupled to another source of matter driving most of the collapse (e.g. extending the study of [BSW17], which only considered the decoupled EdGB field on top of Oppenheimer-Snyder style collapse, to the full EdGB equations). Recent work suggests that whether or not scalarized black holes form in the theory depends on the functional form of $f(\phi)$ (see Eq. (3.1)) [SMS⁺19, MI19]; with the methods presented in this paper one could explore these questions with numerical solutions to the full theory in spherical symmetry. Another future direction is to study critical collapse in EdGB gravity using adaptive mesh refinement.

Finally, this work could be extended by considering numerical solutions of EdGB gravity in axisymmetry, or without any symmetry restrictions. This would couple in propagating metric degrees of freedom, and hence introduce a qualitatively different aspect of the theory not available in spherical symmetry. If, similar to the conclusions found here and in [RP19b, RP19a], there exist subsets of initial data that offer well-

posed hyperbolic evolution, then EdGB gravity may still be viable as an interesting modified gravity theory to confront with gravitational wave binary merger data. On the other hand, if the linear analysis in [PR17, Pap17] that EdGB gravity is generically ill-posed in a particular gauge applies to all gauges, then the well-posed cases we have found could be an artifact of spherical symmetry, and including any gravitational wave degrees of freedom would render the theory ill-posed.

3.6 Appendix: Convergence of an independent residual

In Fig. (3.15) we present the two-norm (L_2) of the $E_{\theta\theta}$ component of the equation of motion for a representative case, excising the elliptic region, and evolved with fixed mesh refinement. We see second order convergence to zero over the entire run-time $t \approx 2 \times 10^3 m$ of the simulation. The plot only shows the norm computed on the coarsest level, although we observe second order convergence over all levels of fixed mesh refinement (four in addition to the base level). As an example of how this translates to solution error, for the highest resolution case shown in Fig.3.15, after the early time transient behavior and the solution has settled to be nearly static at the horizon (see Fig.3.12), we see a net drift in the mass of the black hole of $\delta m/m \sim 0.4\%$ over the remainder of the simulation. Other curvature couplings give similar results. If we do not excise the elliptic region we begin to lose convergence there, and eventually the code crashes, as expected.

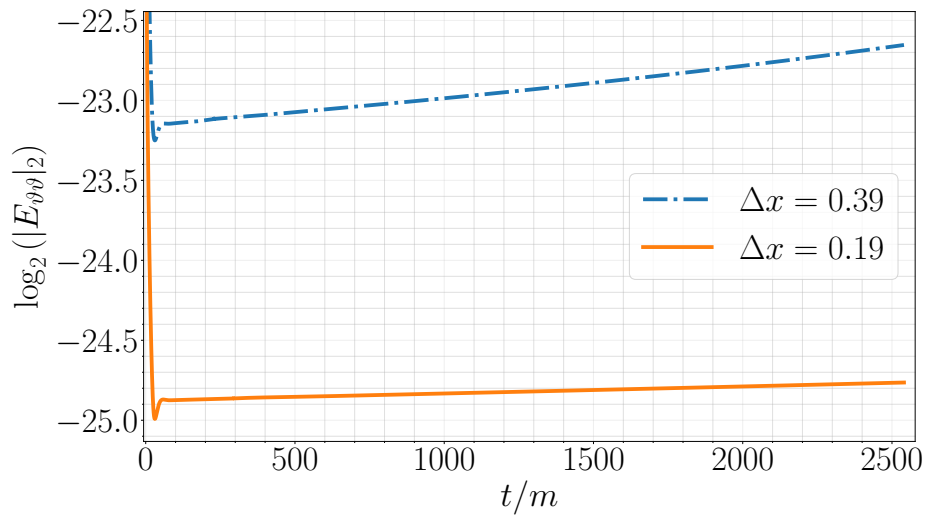


Figure 3.15: Second order convergence to zero of the $\vartheta\vartheta$ component of the equation of motion (3.3a) from a representative run: Schwarzschild black hole initial data, and curvature coupling $C = 0.16$. Shown is $\log_2(|E_{\vartheta\vartheta}|_2)$ versus time computed on the base level of a fixed mesh refinement run (other levels also show second order convergence to zero). The \log_2 is chosen so the second order convergence is more apparent. For simulation parameters see Table. 3.1.

Chapter 4

Dynamics of a \mathbb{Z}_2 symmetric EdGB gravity in spherical symmetry

Here we consider the nonlinear dynamics of EdGB gravity with a different class of couplings and scalar field potentials. This is adapted from a paper I wrote with Frans Pretorius [[RP20a](#)].

4.1 Introduction

The recent advent of the field of gravitational wave astronomy has led to increased interest in testing modifications/extensions of general relativity (GR) (e.g. [[A+16a](#)]). This requires understanding the dynamics of those theories during binary black hole inspiral and merger. While perturbative solutions to modified gravity theories may be sufficient to describe their predictions during the inspiral phase, where the black holes are well separated and gravitational fields are relatively weak, the loudest signal during binary inspiral comes from the merger phase, where gravity is in the strong field, dynamical regime (e.g. [[YYP16](#)]). Order reduction solutions to modified gravity theories offer a potential route to extracting predictions from those theories (e.g. [[OSSH17](#), [OST19](#)]). Solving the full equations of motion without using order reduction

potentially offers certain advantages though, as in this approach one does not have to consider delicate issues (e.g. “secular effects”) regarding when the perturbative order-reduction approximation may fail. Motivated by this, here we consider the nonlinear spherical dynamics of a variant of Einstein dilaton Gauss-Bonnet (EdGB) gravity in spherical symmetry. While much of the relevant physics to gravitational wave astronomy (most importantly, gravitational waves) are not present in spherical symmetry, our study explores the dynamics of the scalar degree of freedom in the theory, which will be relevant when solving for the dynamics of the theory in less symmetrical spacetimes.

The variant of EdGB gravity we study has been shown to possess spherically symmetric scalarized black hole solutions that are stable to linear, radial perturbations [MSB⁺19]. We find numerical evidence that stable scalarized black holes can be formed in this theory, but for large enough Gauss-Bonnet coupling the theory dynamically loses hyperbolicity. Our results, along with the recent work of [KR20a, KR20b], suggests that for sufficiently small couplings scalarized black hole solutions in this theory could be studied in binary inspiral and merger scenarios.

An outline of the remainder of the paper is as follows. In Sec.4.2 we describe the particular EdGB theory we consider, and the resulting equations of motion in spherical symmetry. In Sec.4.3 we briefly summarize earlier work on scalarized black holes in this theory. In Sec.4.4 we describe our numerical code. In Sec. 4.5 we describe the characteristic analysis we employ during evolution, contrasting it with linear perturbation analysis. In Secs. 4.6 and 4.7 we describe our initial data and evolution results respectively. We present concluding remarks in Sec. 4.8.

We use geometric units ($8\pi G = 1$, $c = 1$) and follow the conventions of Misner, Thorne, and Wheeler [MTW17].

4.2 Equations of motion

The action for the class of EdGB gravity theories we consider is

$$S = \int d^4x \sqrt{-g} \left(\frac{1}{2}R - \frac{1}{2}(\nabla\phi)^2 - V(\phi) + W(\phi)\mathcal{G} \right), \quad (4.1)$$

where ϕ is a scalar field (the “dilaton” field), g is the metric determinant, $V(\phi)$ and $W(\phi)$ are (so far unspecified) functions of ϕ , R is the Ricci scalar, and \mathcal{G} is the Gauss-Bonnet scalar:

$$\mathcal{G} \equiv \frac{1}{4} \delta_{\rho\sigma\gamma\delta}^{\mu\nu\alpha\beta} R^{\rho\sigma}{}_{\mu\nu} R^{\gamma\delta}{}_{\alpha\beta}, \quad (4.2)$$

where $\delta_{\rho\sigma\gamma\delta}^{\mu\nu\alpha\beta}$ is the generalized Kronecker delta tensor and $R^{\rho\sigma}{}_{\mu\nu}$ is the Riemann tensor. Varying (4.1) with respect to the metric and scalar fields, the EdGB equations of motion are

$$E_{\mu\nu}^{(g)} \equiv R_{\mu\nu} - \frac{1}{2}g_{\mu\nu}R + 2\delta_{\alpha\beta\rho\sigma}^{\gamma\delta\kappa\lambda} R^{\rho\sigma}{}_{\kappa\lambda} (\nabla^\alpha \nabla_\gamma W(\phi)) \delta^\beta_{(\mu} g_{\nu)\delta} - T_{\mu\nu} = 0, \quad (4.3a)$$

$$T_{\mu\nu} \equiv \nabla_\mu \phi \nabla_\nu \phi - g_{\mu\nu} \left[\frac{1}{2}(\nabla\phi)^2 + V(\phi) \right],$$

$$E^{(\phi)} \equiv \nabla_\mu \nabla^\mu \phi - V'(\phi) + W'(\phi)\mathcal{G} = 0, \quad (4.3b)$$

where the “prime” operation defines a derivative with respect to the scalar field ϕ ; e.g. $V'(\phi) \equiv dV(\phi)/d\phi$. We see that if $\phi = \text{const.}$, then the Gauss-Bonnet scalar term does not contribute to the equations of motion; this is a consequence of the fact that the Gauss-Bonnet scalar is locally a total derivative in four dimensional spacetime (see e.g. [Nak18]). In this article we will solve Eqs. (4.3) with the following choice for functions $V(\phi)$ and $W(\phi)$

$$V(\phi) = \frac{1}{2}\mu^2\phi^2 + \lambda\phi^4, \quad (4.4a)$$

$$W(\phi) = \frac{1}{8}\eta\phi^2, \quad (4.4b)$$

where μ, λ and η are constant parameters¹. In our earlier works on EDGB gravity we used the potentials $V = 0, W = \lambda\phi$ [RP19b, RP20b, RP19a]); that choice en-

¹These are the same potentials used by the authors in [MSB⁺19]; for the particular numerical values of the coupling parameters μ, λ , and η we have rescaled ours to match those in [MSB⁺19], taking into account our different choice of scalar field normalization.

compasses the leading order term for shift symmetric $\phi \rightarrow \phi + \text{const.}$ EdGB gravity models. Here, we focus on the form (4.4a) and (4.4b), the leading order contributions to theories that have $\phi \rightarrow -\phi$ (\mathbb{Z}_2) symmetry [MSB+19]². We note that with the code we have developed we could in principle investigate the spherical dynamics of EdGB gravity theories with arbitrary functions $V(\phi)$ and $W(\phi)$ (see Sec. 4.4.1).

The potential $W(\phi)$ satisfies an “existence condition” for pure GR solutions [SSG+18]: at the minimum ϕ_0 of the potential $W(\phi)$, here $\phi_0 = 0$, the potential satisfies:

$$W'|_{\phi=0} = 0. \quad (4.5)$$

That is, for W that obey Eq. (4.5) we can obtain dynamical GR solutions with $\phi = 0$, as the ϕ will not be sourced by curvature (although it could still potentially be sourced by other matter fields, and once there are regions where $\phi \neq 0$, $W' \neq 0$ and the scalar field could then be sourced by curvature terms).

We evolve this system in Painlevé-Gullstrand (PG)-like coordinates (e.g. [ABCL05, ZK09, KSH11, Rip19])

$$ds^2 = -\alpha(t, r)^2 dt^2 + (dr + \alpha(t, r)\zeta(t, r)dt)^2 + r^2 (d\vartheta^2 + \sin^2\vartheta d\varphi^2), \quad (4.6)$$

so-named since $t = \text{const.}$ cross sections are spatially flat as in the PG coordinate representation of the Schwarzschild black hole (which in these coordinates is given by $\alpha = 1, \zeta = \sqrt{2m/r}$).

We define the variables

$$Q \equiv \partial_r \phi, \quad (4.7a)$$

$$P \equiv \frac{1}{\alpha} \partial_t \phi - \zeta Q = n^\mu \partial_\mu \phi, \quad (4.7b)$$

and obtain the following system of evolution equations for ϕ , Q and P :

$$E_{(\phi)} \equiv \partial_t \phi - \alpha (P + \zeta Q) = 0, \quad (4.8a)$$

²We note though that we do not have a $(\nabla\phi)^4$ term in our action, even though it is symmetric under $\phi \rightarrow -\phi$ and is of no higher order than the Gauss-Bonnet term, as in this work we only wish to consider how black hole dynamics are affected by the addition of a scalar Gauss-Bonnet coupling.

$$E_{(Q)} \equiv \partial_t Q - \partial_r (\alpha [P + \zeta Q]) = 0, \quad (4.8b)$$

$$E_{(P)} \equiv \mathcal{A}_{(P)} \partial_t P + \mathcal{F}_{(P)} = 0. \quad (4.8c)$$

The evolution equation for ϕ (Eq. (4.8a)) follows from the definition of P (Eq. (4.7b)), and the evolution equation for Q (Eq. (4.8b)) follows from taking the radial derivative of Eq. (4.8a). The evolution equation for P (Eq. (4.8c)) comes from taking algebraic combinations of Eq. (4.3b) and the tr , rr , and $\vartheta\vartheta$ components of Eq. (4.3a) (c.f. [RP19a]). The quantities $\mathcal{A}_{(P)}$ and $\mathcal{F}_{(P)}$ are lengthy expressions of $\{\alpha, \zeta, P, Q\}$ and their radial derivatives. In the limit $W = 0$, Eq. (4.8c) reduces to

$$\partial_t P - \frac{1}{r^2} \partial_r (r^2 \alpha [Q + \zeta P]) + \alpha V' = 0. \quad (4.9)$$

Interestingly, in PG coordinates the Hamiltonian and momentum constraints do not change their character as elliptic differential equations (or more properly, as ordinary differential equations in the radial coordinate r) going from GR to EdGB gravity:

$$\begin{aligned} E_{\mu\nu}^{(g)} n^\mu n^\nu &\propto \left(1 - \frac{8QW'}{r} - \frac{12P\zeta W'}{r}\right) \partial_r \zeta + \left(\zeta - \frac{8Q\zeta W'}{r} - \frac{12P\zeta^2 W'}{r}\right) \frac{\partial_r \alpha}{\alpha} \\ &+ \frac{\zeta}{2r} - \frac{r}{2\zeta} \rho - \frac{4W'\zeta}{r} \partial_r Q - \frac{4W''Q^2\zeta}{r} = 0, \end{aligned} \quad (4.10a)$$

$$\begin{aligned} E_{\mu r}^{(g)} n^\mu &\propto \left(1 - \frac{8W'Q}{r} - \frac{8W'P\zeta}{r} + \frac{4W'Q\zeta^2}{r}\right) \frac{\partial_r \alpha}{\alpha} - \frac{r}{2\zeta} j_r \\ &+ \frac{4W'\zeta}{r} \partial_r P + \frac{4W'Q\zeta}{r} \partial_r \zeta + \frac{4W''PQ\zeta}{r} = 0, \end{aligned} \quad (4.10b)$$

where

$$\rho \equiv n^\mu n^\nu T_{\mu\nu} = \frac{1}{2} (P^2 + Q^2) + V, \quad (4.11a)$$

$$j_\kappa \equiv -\gamma^\mu{}_\kappa n^\nu T_{\mu\nu} = -PQ, \quad (4.11b)$$

and $n_\mu \equiv (-\alpha, 0, 0, 0)$.

4.3 Earlier work on \mathbb{Z}_2 symmetric EdGB gravity

Here we briefly review recent work on \mathbb{Z}_2 symmetric EdGB gravity theories. Potentials of the form $V = 0$ and $W = w_2 \phi^2$ were considered in [SSG+18]. There the authors

found scalarized black hole solutions, which were subsequently found to be mode unstable to radial perturbations in [BSDKY18]. Subsequently, radial mode-stable scalarized black hole solutions were found for couplings of the form $V = 0$, $W = w_2\phi^2 + w_4\phi^4$ in [MI19, SMS+19]. Couplings of the form $V = 0$ and $W = c_0 + \exp(c_e\phi^2)$ have been investigated in [DY18, BSDKY18], and also give rise to radially stable scalarized black hole solutions.

The authors in [MSB+19] introduced the model we study in this article, $V = \mu^2\phi^2 + 2\lambda\phi^4$, $W = \eta\phi^2/4$. This model is motivated by effective field theory arguments: assuming the action is invariant under the \mathbb{Z}_2 symmetry $\phi \rightarrow -\phi$, the action contains all terms (except for the term $(\nabla\phi)^4$, which we do not consider in this article) of mass dimension equal to or less than the mass dimension of $\phi^2\mathcal{G}$, which is the lowest order term that couples ϕ to the Gauss-Bonnet scalar subject to this symmetry. Though like the authors in [MSB+19], while we motivate this model from effective field theory we in fact will treat the theory as a complete classical field theory, and consider exact (to within numerical truncation error) solutions to the equations of motion.

In [MSB+19], the authors found scalarized black hole solutions stable to linear radial perturbations for certain ranges of the dimensionless parameters

$$\hat{M} \equiv \frac{M}{\eta^{1/2}}, \tag{4.12a}$$

$$\hat{\Phi} \equiv \frac{\Phi}{\eta^{1/2}}, \tag{4.12b}$$

$$\hat{\mu} \equiv \mu\eta^{1/2}, \tag{4.12c}$$

$$\hat{\lambda} \equiv \lambda\eta, \tag{4.12d}$$

where M is the asymptotic mass of the black hole plus scalar field configuration and Φ is the asymptotic scalar “charge”, i.e. for scalarized black hole solutions to the theory it is the coefficient to the leading nonzero term in $\phi(t, r)$ as r goes to infinity [MSB+19]

$$\lim_{r \rightarrow \infty} \phi(t, r) \sim e^{-\mu r} \left(\frac{1}{r} \Phi + \dots \right). \tag{4.13}$$

A nonzero value of $\hat{\lambda}$ is necessary to have radially linear mode stable scalarized black hole solutions, and the value of $\hat{\lambda}$ needed to stabilize a given scalarized black hole increases as $\hat{\mu}$ increases [MSB⁺19]. For example, when $\hat{\mu} = 0$, the minimum value of $\hat{\lambda} \approx 0.2$. There is also a maximum value of \hat{M} for a scalarized black hole (above this the Schwarzschild solution is stable); for example for $\hat{\mu} = 0$, found this maximum to be $\hat{M} \approx 0.6$.

4.4 Description of code and simulations

4.4.1 Code description

Our basic evolution strategy is the same as in [RP20b]: we freely evolve P and Q using Eqs. (4.8b) and (4.8c), and solve for α and ζ using the constraint equations, Eqs. (4.10a) and (4.10b). The boundary condition for ζ at the excision boundary is obtained by freely evolving it using the E_{tr} equation of motion (with algebraic combinations of the other equations of motion to remove time derivatives of α and P). We do not need to impose any boundary condition for α on the excision boundary due to the $\alpha \rightarrow \alpha + c(t)$ residual gauge symmetry in PG coordinates. The full equations of motion for P and the freely evolved ζ on the boundary are long and unenlightening, although see Appendix C of [RP20b] for their full form in PG coordinates for the special case $V = 0$ (and note that there we use the notation $W \equiv f$).

As in [RP20b], we solve the constraint equations using the trapezoid rule (a second order method) with relaxation. Unlike [RP20b] though, we solve the evolution equations for $\{P, Q\}$, and ζ on the excision boundary using a fourth order method of lines technique: we use fourth order centered difference stencils to evaluate the spatial derivatives, and evolve in time with a fourth order Runge-Kutta integrator (e.g. [PTVF07, GKO95]). At the excision boundary and the boundary at spatial infinity we used one-sided difference stencils to evaluate spatial derivatives. We solve the equations over a single grid (unigrad evolution). An example of a convergence

study with the independent residual E_{rr} is shown in Fig. 4.3.

The code is written in C++, and can be accessed at [\[Rip20a\]](#).

4.4.2 Diagnostics

Our code diagnostics are as in [\[RP19b, RP20b, RP19a\]](#), which we very briefly review here. The mass of a given simulation is determined by the value of the Misner-Sharp mass at spatial infinity:

$$m_{total} = \lim_{r \rightarrow \infty} m_{MS}(t, r) = \lim_{r \rightarrow \infty} \frac{r}{2} \zeta(t, r)^2. \quad (4.14)$$

Another diagnostic we compute is the radial characteristic speed of the dynamical degree of freedom of EdGB gravity in spherical symmetry. To compute the radial characteristic speeds, we compute the characteristic vector ξ_a by finding the zeros of the characteristic equation:

$$\det \left[\begin{pmatrix} \delta E_{(P)}/\delta(\partial_a P) & \delta E_{(P)}/\delta(\partial_a Q) \\ \delta E_{(Q)}/\delta(\partial_a P) & \delta E_{(Q)}/\delta(\partial_a Q) \end{pmatrix} \xi_a \right] = 0. \quad (4.15a)$$

and then compute the ingoing and outgoing characteristic speeds $c_{\pm} \equiv \mp \xi_t / \xi_r$. Expanding Eq. (4.15a) gives us a quadratic equation for the radial characteristic speeds

$$\mathcal{A}c^2 + \mathcal{B}c + \mathcal{C} = 0, \quad (4.16)$$

where \mathcal{A} , \mathcal{B} , and \mathcal{C} are complicated functions of the metric and scalar fields, and their time and radial derivatives (c.f. [\[RP20b\]](#)). The discriminant $\mathcal{D} \equiv \mathcal{B}^2 - 4\mathcal{A}\mathcal{C}$ determines the hyperbolicity of the theory at each spacetime point. Where $\mathcal{D} > 0$, the radial characteristic speeds are real and the equations of motion for the theory at that spacetime point are hyperbolic. Where $\mathcal{D} < 0$, the radial characteristic speeds are imaginary and the equations of motion for the system defined by Eq (4.8a), Eq (4.8b), and Eq (4.8c) at that spacetime point are elliptic ³. We discuss the

³Note that even though our evolution system consists of three transport equations, the system is degenerate and describes the evolution for a single degree of freedom, which we can define the ingoing and outgoing radial characteristic for. The system defined by Eq (4.8a), Eq (4.8b), and Eq (4.8c) is degenerate as $Q \equiv \partial_r \phi$, and the equation of motion for Q is just the radial derivative of the equation of motion for ϕ .

difference between computing the radial characteristics and computing the modes of radial linear perturbations about a stationary solution in Sec. 4.5.

We determine the location of the black hole horizon in our simulation by computing the location of the marginally outer trapped surface (MOTS) for outgoing null characteristics [Tho07]. In PG coordinates the radial null characteristics are

$$c_{\pm}^{(n)} = \alpha(\pm - \zeta), \quad (4.17)$$

thus the location of the MOTS is at the point $\zeta(t, r) = 1$.

4.5 Characteristics versus linearized perturbation analysis

Here we provide a brief discussion of the difference between linear perturbation theory analysis to identify stable/unstable modes (which is what is done in [MSB+19]) and characteristic analysis (which is the analysis we perform in our code).

The scalar field offers the only dynamical degree of freedom in EdGB gravity in spherical symmetry. The authors in [MSB+19] linearized the dynamics of that degree of freedom (which we denote by φ), and found that for a *static* background it obeys an equation of the form

$$h(r)\frac{\partial^2\varphi}{\partial t^2} - \frac{\partial^2\varphi}{\partial r^2} + k(r)\frac{\partial\varphi}{\partial r} + p(r)\varphi = 0, \quad (4.18)$$

where h, k, p are functions of the static background geometry. They considered solutions of the form $\varphi(t, r) = e^{i\omega t}\psi(r)$, and searched for conditions that would make $\omega^2 < 0$.

The characteristics of Eq. (4.18) are found by keeping only highest derivative terms and replacing $\partial_t \rightarrow \xi_t$, $\partial_r \rightarrow \xi_r$, where $\xi_a \equiv (\xi_t, \xi_r)$ is the characteristic vector (see e.g. [Lax73, KL89], or [RP19b, RP19a] in the context of shift symmetric EdGB gravity), and finding the zeros of this principal symbol of the system:

$$h(r)\xi_t^2 - \xi_r^2 = 0. \quad (4.19)$$

The solutions $c \equiv -\xi_t/\xi_r$ to this equation give the radial characteristic speeds. Finding $\omega^2 < 0$ solutions to Eq. (4.18) can simply indicate a particular background solution is unstable to perturbations. In that case, as long as the theory remains hyperbolic the unstable solution could evolve to a different, stable one. By contrast, finding a $c^2 < 0$ solution to Eq. (4.19) indicates a breakdown of hyperbolicity of the theory evaluated at that solution. When hyperbolicity has broken down, the equations of motion can no longer be solved as evolution equations.

We emphasize that the form of the characteristic equation we solve, Eq. (4.15a), does *not* take the form Eq. (4.19), as we solve the characteristic equation within a dynamical spacetime, and we use a different coordinate system than is used in [MSB⁺19]. Instead the characteristic equation takes the schematic form (compare to Eq. (4.16))

$$\mathcal{A}\xi_t^2 - \mathcal{B}\xi_t\xi_r + \mathcal{C}\xi_r^2 = 0, \quad (4.20)$$

where \mathcal{A} , \mathcal{B} , and \mathcal{C} depend on the background fields α , ζ , P , Q , and their radial and time derivatives.

From the forms of Eq. (4.18) and Eq. (4.19) it is clear that linear (in)stability does not necessarily imply (lack of) hyperbolicity, or vice-versa. Nevertheless our hyperbolicity analysis does conform with the general results of [MSB⁺19].

4.6 Initial data

4.6.1 General considerations

We may freely specify ϕ and $\partial_t\phi$ (or, ϕ and P) on the initial data surface as ϕ satisfies a second order in time wave-like equation, provided the characteristics for that equation are real. The variables α and ζ must satisfy the constraint equations, and are not freely specifiable.

Note that $\phi = 0, \partial_t\phi = 0$ is not just a solution to the initial value problem for

EdGB gravity with this coupling potential ((4.4a) and (4.4b)), it is also a consistent solution to the full evolution equations (in fact this was one criterion used by the authors in [SSG⁺18] in constructing this model of EdGB gravity). This is in contrast to EdGB gravity with a linear shift-symmetric potential, where $\phi = 0, \partial_t \phi = 0$ can be imposed as an initial condition, but then ϕ will generically evolve to non-zero values with time.

4.6.2 Black hole initial data with a small exterior scalar pulse

Our class of initial data is similar to that we used in [RP20b]: the free initial data is ϕ and P , from which we can determine Q, α, ζ . To have black hole initial data, at the initial excision boundary x_{exc} we set

$$\alpha|_{x=x_{exc}} = 1, \quad (4.21)$$

$$\zeta|_{x=x_{exc}} = \sqrt{\frac{2M}{r}}, \quad (4.22)$$

with ϕ and P compactly supported away from the excision boundary, and then integrate outwards in r to obtain α and ζ over the initial data surface. The quantity M in Eq. (4.21) is the initial mass of the black hole.

We choose the following for the exterior scalar pulse

$$\phi_b(t, r)|_{t=0} = \begin{cases} \frac{a_0}{n_0} (r - r_l)^2 (r_u - r)^2 \exp\left[-\frac{1}{r-r_l} - \frac{1}{r_u-r}\right] & r_l < r < r_u \\ 0 & \text{otherwise} \end{cases}, \quad (4.23a)$$

$$Q_b(t, r)|_{t=0} = \partial_r \phi(t, r)|_{t=0}, \quad (4.23b)$$

$$P_b(t, r)|_{t=0} = 0, \quad (4.23c)$$

where $r_u > r_c > r_l > 2M$, and the normalization n_0 is chosen such that

$$\max \phi_b(t, r)|_{t=0} = a_0. \quad (4.24)$$

4.6.3 Approximate scalarized profile

We also consider initial data that approximates the static decoupled scalarized profile on a Schwarzschild black hole background (see also [MSB⁺19]):

$$\phi(t, r)|_{t=0} = \frac{\Phi_0}{r} \exp(-\mu(r - 3M)), \quad (4.25)$$

$$Q(t, r)|_{t=0} = \partial_r \phi(t, r)|_{t=0}, \quad (4.26)$$

where Φ_0 is a constant. We choose P so that $\partial_t \phi \approx 0|_{t=0}$ (see (4.7b)): we set

$$P(t, r)|_{t=0} = -Q(t, r)\zeta(t, r)|_{t=0}, \quad (4.27)$$

and initially set $\alpha = 1$, $\zeta = \sqrt{2M/r}$. We then resolve the constraints for α and ζ , set P as above, and iterate this process until the maximum change in P , $|\Delta P|_\infty$, between iterations is less than 10^{-3} .

We next provide a derivation of Eq. (4.25). Consider a Schwarzschild background: we set $\alpha = 1$, $\zeta = \sqrt{2m/r}$, set $\partial_t \phi = 0$, and solve Eq. (4.3b)

$$\nabla_\mu \nabla^\mu \phi - \left(\mu^2 - \frac{1}{4} \eta \mathcal{G} \right) \phi - 4\lambda \phi^3 = 0. \quad (4.28)$$

Plugging things in, we find

$$\left(1 - \frac{2m}{r} \right) \frac{d^2 \phi}{dr^2} + 2 \left(1 - \frac{m}{r} \right) \frac{1}{r} \frac{d\phi}{dr} - \left(\mu^2 - \frac{12\eta m^2}{r^6} \right) \phi - 4\lambda \phi^3 = 0. \quad (4.29)$$

In the far field limit ($r \rightarrow \infty$), and assuming $\lim_{r \rightarrow \infty} \phi = 0$, we have to leading order

$$\frac{d^2 \phi}{dr^2} + \frac{2}{r} \frac{d\phi}{dr} = \mu^2 \phi. \quad (4.30)$$

The solution consistent with the field going to zero at spatial infinity is

$$\phi(r) = \frac{C}{r} \exp(-\mu r), \quad (4.31)$$

where C is a constant. We can split up this constant into two as follows:

$$\phi(r) = \frac{c_1}{r} \exp(-\mu(r - c_2)). \quad (4.32)$$

In our simulations we set $c_2 = 3m$ on the initial data slice, see Eq. (4.25).

4.7 Numerical results

We will only present results for $\eta > 0$, and absorb η into the definition of the dimensionless parameters (Eqs. (4.12a)-(4.12d)). As one check of the code we did perform simulations with the GR case $\eta = 0$; in these simulations some of the scalar field would fall into the black hole, and some of the field would disperse to infinity, leaving a vacuum Schwarzschild solution behind. This is consistent with the no hair theorems for a canonically coupled scalar field with a potential in asymptotically flat spacetimes (for a review and references see e.g. [Sot15]), along with perturbative solutions of scalar fields around a Schwarzschild black hole background (for a review and references see e.g. [BCS09]).

We find that for both classes of initial data described in the previous section, we can separate the solutions into three types: (1) the scalar field disperses, leaving behind a Schwarzschild black hole, (2) the black hole scalarizes and approaches a static solution, or (3) an elliptic region eventually forms outside the black hole (i.e. exterior to the apparent horizon).

4.7.1 Compact scalar pulse initial data

In Fig. 4.1 we show several points on a plot of \hat{M} versus $\hat{\lambda}$ (for the definition of \hat{M} and $\hat{\lambda}$ see respectively Eq. (4.12a) and Eq. (4.12d)), indicating the division between evolution that forms elliptic regions and that which does not, beginning from the compact pulse initial data described in Sec. 4.6.2. To arrive at the numerical data points in the figure, we fixed the initial data parameters r_l , r_u , and a_0 and black hole mass. Specifically, we chose $r_l = 0.24$, $r_u = 32$, $a_0 = 5 \times 10^{-3}$ ((4.23a)), and initial Schwarzschild black hole mass $M \approx 10$ ((4.21)). The contribution of the scalar field to the total mass of the spacetime is $M_\phi \sim 9.6 \times 10^{-3}$ ⁴. We then performed a

⁴We estimate the scalar field contribution to the total asymptotic Misner-Sharp mass by subtracting off from the initial Misner-Sharp mass the mass of the black hole initial data we had before we resolved the constraints with scalar field initial data.

bisection search for the value of η that would lead to regular evolution within a run time of $t/M \sim 200$ (sufficiently long for the solution to settle to a near-stationary state if no elliptic region formed). As we varied η , we varied μ and λ such that $\hat{\mu}$ and $\hat{\lambda}$ remained fixed (see Eqs. (4.12a)-(4.12d)). Fig. 4.1 shows that the theory can remain hyperbolic for perturbations of at least some black hole solutions.

Also overlaid on Fig. 4.1 are the estimated minimum $\hat{\lambda}$, $\min\hat{\lambda}$, to have a stable scalarized black hole solution, and the minimum \hat{M} , $\min\hat{M}$, to have a stable Schwarzschild black hole solution with respect to linear radial perturbations computed in [MSB⁺19]. From those results one would expect for $\hat{M} < \min\hat{M}$ and for $\hat{\lambda} > \min\hat{\lambda}$, Schwarzschild black holes would be unstable under radial scalar field perturbations to forming (stable) scalarized black hole solutions. Our numerical results are in general agreement with this reasoning (except that for small enough \hat{M} a elliptic region grows outside of the black hole horizon). In particular, above the horizontal purple line in Fig. 4.1 initial small perturbations in ϕ decay and leave behind a Schwarzschild black hole, while below this and to the right of the dashed yellow line the black holes scalarize (and the solutions above the line implied by the blue dots are free of elliptic regions exterior to the black hole horizon). For $\hat{\lambda}$ to the left of the yellow dashed line, we find only two regimes: either the scalar field disperses and the solution settles to a Schwarzschild black hole solution, or a naked elliptic region forms. From Fig. 4.1, we see that the dividing line between elliptic region formation and Schwarzschild end state solutions for $\hat{\lambda} < \min(\hat{\lambda})$ does not quite lie on the value of $\min(\hat{M})$ predicted for stable Schwarzschild black hole solutions by [MSB⁺19]. That being said, our value is not in significant “tension” with what they computed, given the estimated errors of our calculation and given that the authors in [MSB⁺19] performed a linear perturbation analysis about a static background.

In Fig. 4.2 we show example scalar field solutions at three different resolutions to demonstrate convergence for the three kinds of behavior we generally observe in our simulations—decay to Schwarzschild, scalarization, and development of an elliptic

region.

Fig. 4.3 provides an example of an independent residual for a run that formed an elliptic region, demonstrating convergence of the solution prior to the appearance of the elliptic region. The mass of the initial scalar field for this case is $M_\phi \approx 0.01$, compared to the initial black hole mass of $M \approx 10$. Once the scalar field interacts with the black hole, it begins to grow near the horizon, and an elliptic region grows and expands past the black hole horizon. This behavior is qualitatively similar to what we found for shift-symmetric EdGB gravity [RP20b].

4.7.2 Numerical results: approximately scalarized black hole initial data

The results of evolving the approximate scalarized initial data described in Sec. 4.6.3 are qualitatively similar to that of the perturbed Schwarzschild case described in the previous section; Fig. 4.4 is the analogous plot to that of Fig. 4.1 to illustrate. For the relevant initial data parameter we chose $\Phi_0 = 0.05$ and $M = 10$ in Eq. (4.25). We found empirically that choosing $\Phi_0 = 0.05$ provided a scalarized profile reasonably close to the final stable scalarized profiles for the \hat{M} , $\hat{\mu}$, and we considered (for the definition of \hat{M} , $\hat{\mu}$, and $\hat{\lambda}$ see respectively Eq. (4.12a), Eq. (4.12c), and Eq. (4.12d)). See Fig. 4.5 for an example of evolution of this initial data to a stable scalarized profile.

We also note that the onset of elliptic region formation in this parameter space does appear to depend on the initial data as well. Comparing Fig. 4.1 and Fig. 4.4 we see that our results support the conclusion that an elliptic region may form at a larger value of \hat{M} when we start with approximately scalarized initial data.

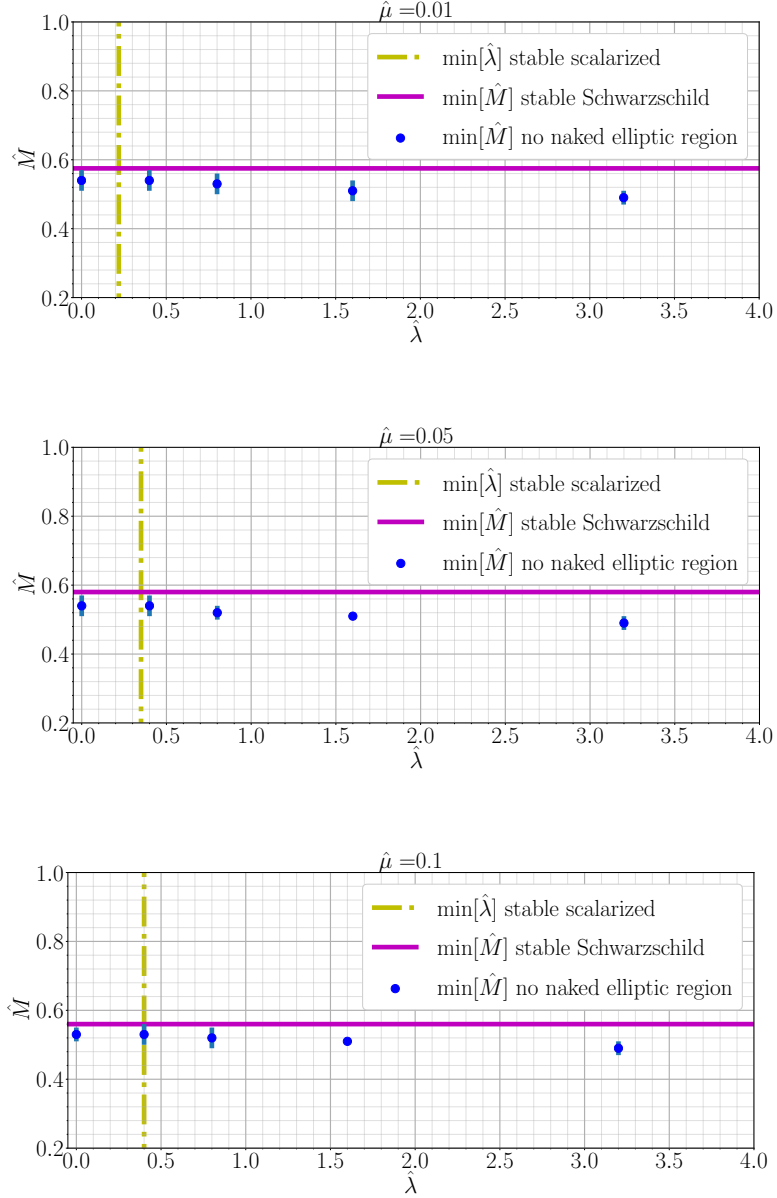
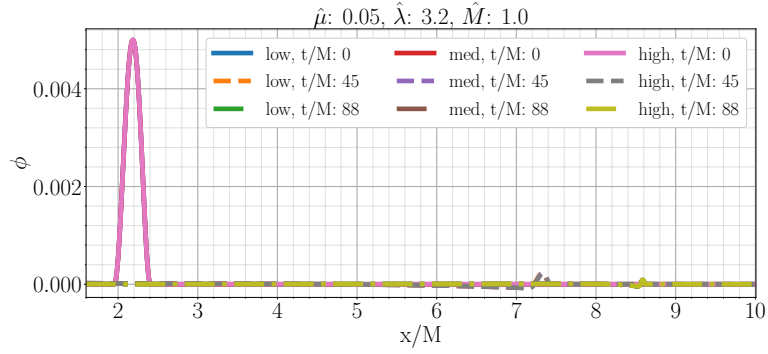
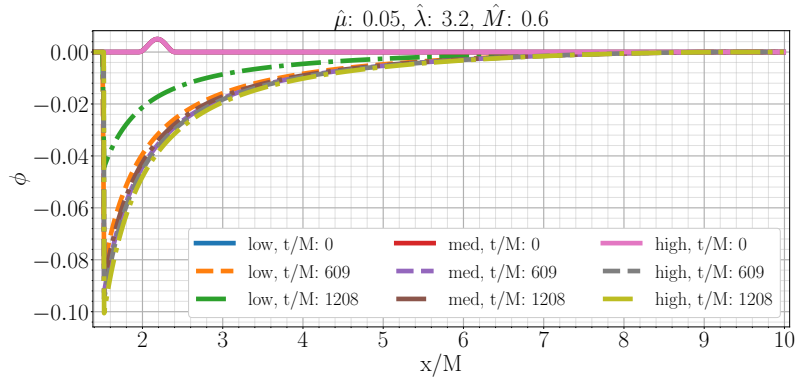


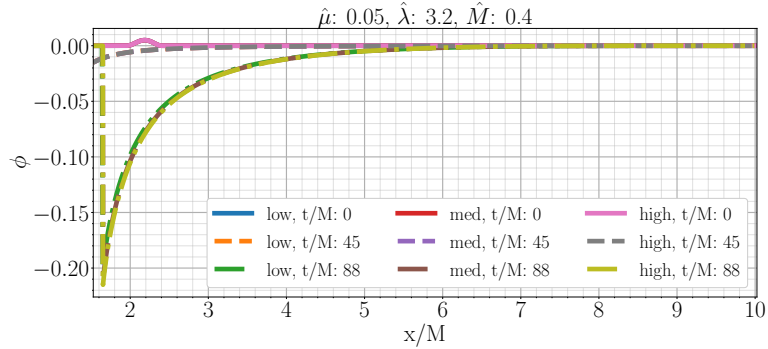
Figure 4.1: Onset of elliptic region formation, from evolution of perturbed Schwarzschild initial data as described in Sec. 4.7.1. The blue dots are our numerically computed values of \hat{M} , Eq. (4.12a), (for a given $\hat{\lambda}$, Eq. (4.12d)) below which an elliptic region eventually forms outside the horizon. The error bars about each point come from truncation error estimates, computed by taking the difference of the elliptic onset point computed with two different resolutions: $N_x = 2^{10} + 1$ and $N_x = 2^{11} + 1$ radial points. The solid purple horizon line is the minimum \hat{M} for a stable *Schwarzschild* black hole, and the dash-dotted yellow vertical line is the minimum $\hat{\lambda}$ for a stable *scalarized* black hole, with respect to linear radial perturbations according to the analysis of [MSB⁺19].



((a)) Scalar field disperses



((b)) Scalarized black hole forms



((c)) Elliptic region formation

Figure 4.2: Example evolution for EdGB solution with compact scalar field initial data as described in Sec. 4.7.1. Regarding the scalarized black hole case (b), there is some truncation error induced decay of the scalar field at late times, most evident in the lower resolution case (dash-dot green curve), however with increasing resolution we do find convergence to a stable, static scalarized black hole. Low resolution for cases (a) and (c) is $N_x = 2^{10} + 1$ grid points, and for case (b) $N_x = 2^9 + 1$ grid points. In all cases med and high resolution are double and quadruple the low resolution respectively.

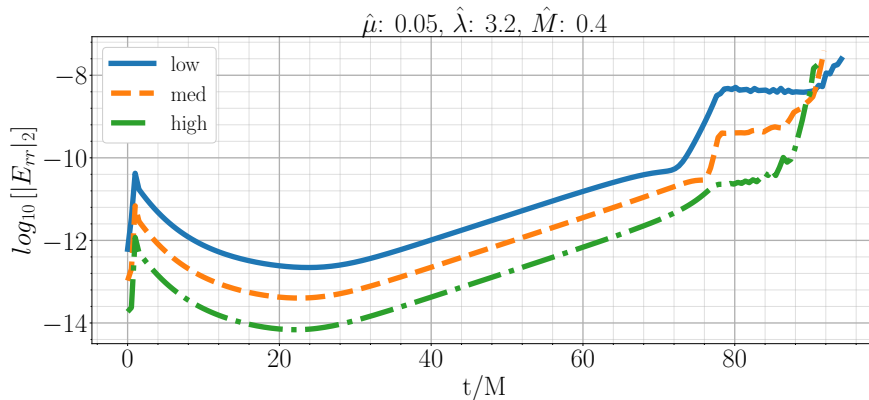


Figure 4.3: Two-norm of the independent residual E_{rr} for a run that forms a naked elliptic region, with compact scalar initial data (see lower panel of Fig. 4.2). We see convergence up until near the formation of the elliptic region. Low resolution corresponds to $N_x = 2^{10} + 1$ grid points, and med and high resolution correspond to double and quadruple that number of grid points. See Sec. 4.7.1 for simulation parameters.

4.8 Discussion

We have numerically investigated perturbed black hole solutions in a \mathbb{Z}_2 symmetric (i.e. a theory with an action invariant under the operation $\phi \rightarrow -\phi$) variant of EdGB gravity. We have found, consistent with the linear analysis of [MSB⁺19], that stable scalarized black holes exist within this theory. However, for sufficiently large couplings relative to the scale of the black hole the theory dynamically loses hyperbolicity: the scalar field grows around the black hole until an elliptic region expands past the black hole horizon. These results, along with the recent results of [KR20a, KR20b], suggests that in a limited parameter range scalarized black holes are subject to well-posed hyperbolic evolution. It would be interesting to see whether this conclusion extends beyond spherical symmetry, for example for binary black hole inspiral and merger. The existence of naked elliptic regions in the theory for sufficiently large couplings though strongly suggests that the theory makes most sense from an effective field theory point of view (which was the original motivation for the particular form of EdGB gravity studied here[MSB⁺19]).

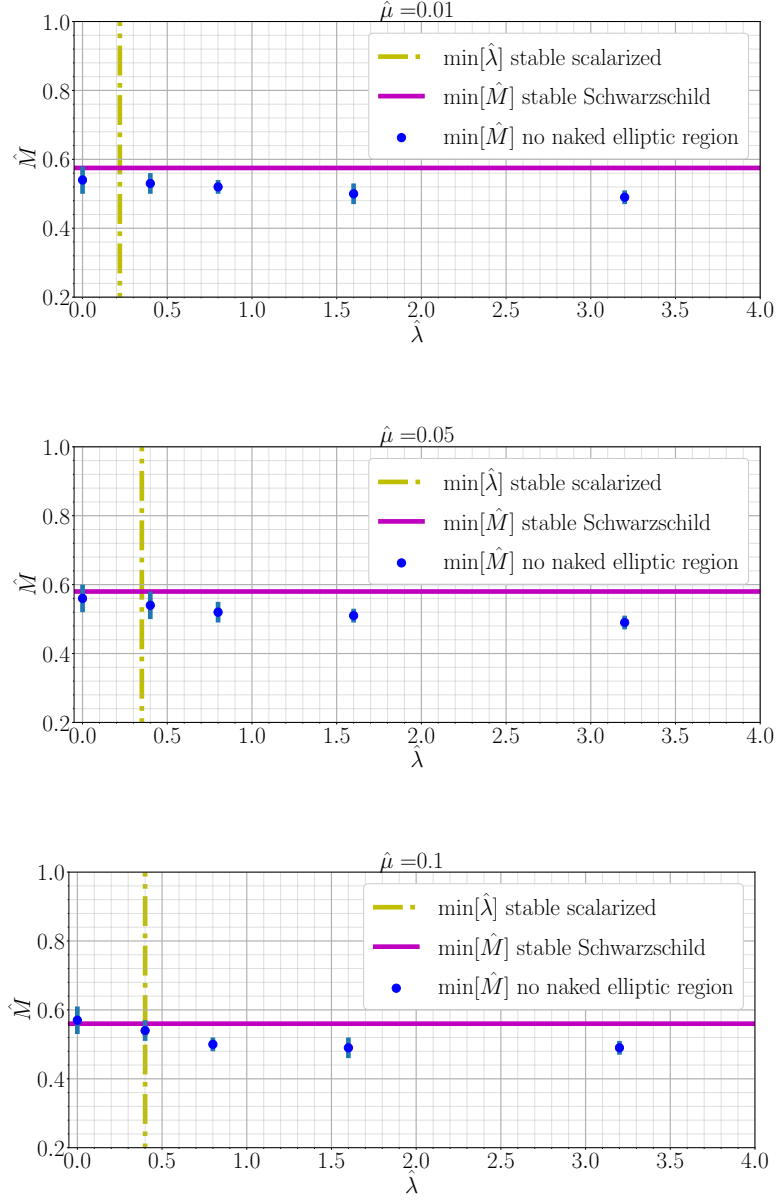


Figure 4.4: Onset of elliptic region formation, from evolution of approximate scalarized black hole initial data as described in Sec. 4.7.2. This is the analog of Fig. 4.1, and the same caption applies here. For definitions of \hat{M} and $\hat{\lambda}$ see respectively Eq. (4.12a) and Eq. (4.12d).

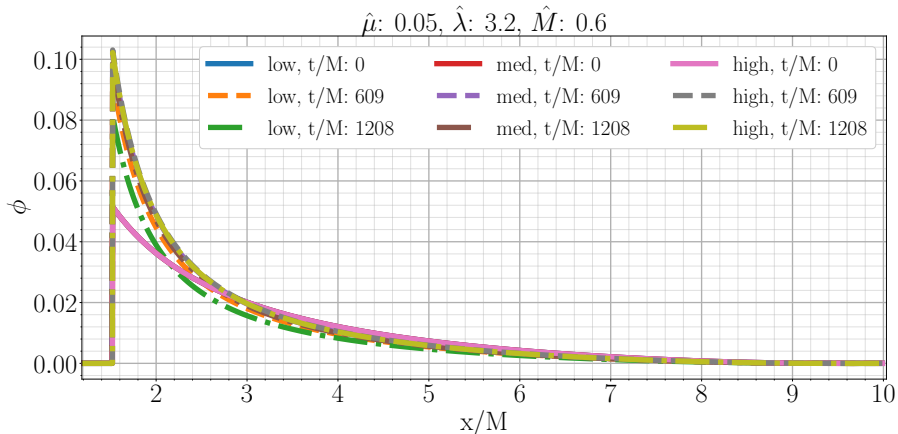


Figure 4.5: Formation of stable scalarized black hole from approximate scalarized initial data as described in Sec. 4.7.2. We show runs with three different resolutions: ‘low’, ‘med’, and ‘high’; ‘low’ resolution corresponds to $N_x = 2^{10} + 1$ radial grid points and ‘med’ and ‘high’ correspond to double and quadruple this number of radial points.

The code[Rip20a] we wrote and used to produce the simulation results presented here can easily be altered to accommodate other forms of Gauss-Bonnet coupling $W(\phi)$ and scalar field potential $V(\phi)$. It would be interesting to investigate how these potential functions influence the structure of scalarized black holes that can form, and the region of solution space hampered by naked elliptic regions. It would also be interesting to include the $(\nabla\phi)^4$ term in action, to see the full range of dynamics that could occur for this class of \mathbb{Z}_2 symmetric scalar-tensor theories.

Chapter 5

Concluding remarks

In this thesis we have described several numerical investigations into the nonlinear dynamics of Einstein dilaton Gauss-Bonnet gravity in spherical symmetry. For the couplings and scalar potentials we considered, we find that when the EdGB “corrections” are suitably small the theory admits a well-posed initial value problem, but for large enough deviations from GR the theory changes type from hyperbolic to elliptic type. As discussed in the introduction, in an order-reduction framework, and interpreted as in EFT, the theory clearly has a locally well-posed formulation, and our results say nothing about any potential UV completion of gravity that includes the EdGB corrections in that framework¹.

While it may not be surprising the EdGB gravity can change character, given that its principal symbol is a function of the background field configuration and their derivatives, it is still interesting to contrast this behavior with what is found in General Relativity (GR). Regular initial data in GR can evolve to geodesically incomplete or singular solutions (e.g. [Cho93, Chr94]), but its character never changes, even though its symbol depends on the background field configuration and it is widely expected that GR itself contains just the leading order terms in some UV complete

¹As discussed in the Introduction though, any potential implementation of an order-reduction approach to EdGB must be interpreted carefully, as the EFT interpretation requires us to include all terms in the equations of motion consistent with a pre-defined set of symmetries to each order in perturbation theory.

quantum theory of gravity. Of course, with the geometric interpretation of GR this fact is less surprising, as the character of the symbol of GR rests on the geometry being Lorentzian, and the dynamics of the Einstein equations cannot change this fundamental feature of the spacetime geometry.

Working in the simple setting of spherical symmetry was most likely crucial in helping us identify the mixed type behavior of the initial value problem in EdGB gravity. Considering the relative simplicity of our methods, it would be interesting to study some of the many other modified gravity theories that have been introduced in recent decades to model for example dark energy.

The work in this thesis could be extended in a variety of other directions. Recent work by Kovacs and Reall [[KR20a](#), [KR20b](#)] have demonstrated that EdGB gravity has a well-posed initial value formulation in generic backgrounds for which the EdGB corrections are suitably small. Their formulation would allow for more (astro)physically realistic numerical solutions to be found. The hyperbolicity of Horndeski theories used in early universe cosmology could be investigated with the techniques laid out in this thesis. We hope as well for the creation of new and better motivated modified gravity theories that could be used to address some of the still unresolved problems in physics described in the Introduction.

Appendix A

Covariant treatment of spherically symmetric spacetimes

We describe spherically symmetric spacetimes in a covariant manner. Parts of this Appendix are adapted from a publication we coauthored with Kent Yagi on black hole perturbation theory [RY18]. See also [AV10, FN12]. We then motivate the use of the quasi-local Misner-Sharp mass for spacetimes that satisfy the Einstein equations, and then for spacetimes that satisfy the EdGB equations.

A.1 Spherically symmetric spacetimes

Spherically symmetric spacetimes are *factorizable*, that is they can be written globally as $M = \Sigma^{(1)} \times \Sigma^{(2)}$, where both $\Sigma^{(i)}$ are (an infinite family of) submanifolds of M . Both submanifolds are two dimensional, one of them is maximally symmetric, and the spacetime can be written as the *warped product* of the maximally symmetric manifold with the other manifold. We can write the metric as

$$ds^2 = \alpha_{ab} du^a du^b + r^2 \Omega_{AB} d\theta^A d\theta^B, \quad (\text{A.1})$$

where Ω_{AB} is the intrinsic metric of the spherically symmetric space, and α_{ab} is the intrinsic metric of the perpendicular spacetime. The warp factor $r = r(u^0, u^1)$ is

called the *areal radius*, because if we integrate over the maximally symmetric manifold $\{\Sigma^{(2)}, \Omega_{AB}\}$ we get $4\pi r^2$. We follow the notation of [RY18]: lower case Latin indices range over 0, 1, upper case Latin indices range over 2, 3, and lower case Greek indices range over 0, 1, 2, 3. Moreover, D will denote a covariant derivative in the perpendicular spacetime, and ∇ will denote a covariant derivative over the whole spacetime.

Note more generally we could consider Ω_{AB} as the metric of a maximally symmetric two dimensional space. There are three potential curvatures for a maximally symmetric space, and for a two dimensional subspace we can classify them according to their Gauss curvature¹ $k = r^2 \frac{1}{2} Ricc[\Omega_{AB}] = 1$. We can then find coordinates such that

$$\Omega_{AB} d\theta^A d\theta^B = \frac{dl^2}{1 - kl^2} + l^2 d\phi^2, \quad (\text{A.2})$$

where $k = -1, 0, +1$ is the Gauss curvature for a negatively, zero, or positively curved maximally symmetric two dimensional space, respectively. For us we will always use $k = +1$, a spherical subspace.

The Einstein-Hilbert action becomes

$$\begin{aligned} S &= \int d^4x \sqrt{-g} R \\ &= 4\pi \int d^2u \sqrt{-\alpha} (r^2 \mathcal{R} + 2(\partial_a r)^2 + 2), \end{aligned} \quad (\text{A.3})$$

where \mathcal{R} is the Ricci scalar intrinsic to the perpendicular manifold, and we have integrated over the spherically symmetric submanifold.

Varying (A.3) with respect to r and α^{ab} gives us

$$0 = r\mathcal{R} - 2\Box r, \quad (\text{A.4a})$$

$$0 = (2r\Box r + (\partial_c r)^2 - 1) \alpha_{ab} - 2r D_a D_b r \equiv r^2 G_{ab}. \quad (\text{A.4b})$$

¹ More generally (as in FLRW cosmologies) we can classify a maximally symmetric space according to the sign of the Ricci scalar: flat is $R = 0$, negative curvature $R < 0$, and positive curvature is $R > 0$.

We can alternatively rewrite the Einstein equations $G_{\mu\nu}$ directly in terms of these coordinates. For reference, the nonzero components of the Riemann tensor are [MN08, RY18]

$$R_{abcd} = \mathcal{R}_{abcd} = \frac{1}{2} \mathcal{R} (\alpha_{ac} \alpha_{bd} - \alpha_{ad} \alpha_{bc}), \quad (\text{A.5a})$$

$$R_{aAbB} = - (r D_a D_b r) \Omega_{AB}, \quad (\text{A.5b})$$

$$R_{ABCD} = [k - (D_c r)^2] r^2 (\Omega_{AC} \Omega_{BD} - \Omega_{AD} \Omega_{BC}), \quad (\text{A.5c})$$

where \mathcal{R}_{abcd} is the Riemann tensor associated with α_{ab} , and k is the Gauss curvature of the maximally symmetric subspace ($k = 1$ when the subspace is spherical, which is what we always will work with).

The nonzero components of the Riemann double dual are

$$(*R^*)^{abcd} = - [k - (D_l r)^2] \frac{1}{r^2} (\alpha^{ac} \alpha^{bd} - \alpha^{ad} \alpha^{bc}), \quad (\text{A.6})$$

$$(*R^*)^{aAbB} = \frac{1}{r^3} \Omega^{AB} (\alpha^{ab} \square r - D^a D^b r), \quad (\text{A.7})$$

$$(*R^*)^{ABCD} = - \frac{1}{2} \mathcal{R} \frac{1}{r^4} (\Omega^{AC} \Omega^{BD} - \Omega^{AD} \Omega^{BC}). \quad (\text{A.8})$$

The nonzero components of the Ricci tensor, along with the Ricci scalar are

$$R_{ab} = \frac{1}{2} \mathcal{R} \alpha_{ab} - \frac{2}{r} D_a D_b r, \quad (\text{A.9})$$

$$R_{AB} = [k - (D_c r)^2 - r \square r] \Omega_{AB}, \quad (\text{A.10})$$

$$R = \mathcal{R} + \frac{2}{r^2} [k - (D_c r)^2] - \frac{4}{r} \square r. \quad (\text{A.11})$$

The nonzero components of the massless scalar stress energy tensor are similarly $T_{ab}[\phi]$ and $T_{AB}[\phi]$. The Gauss-Bonnet scalar is

$$\mathcal{G} \equiv -R_{\alpha\beta\gamma\delta} (*R^*)^{\alpha\beta\gamma\delta} = 4 \frac{1}{r^2} [2(\square r)^2 - 2(D_a D_b r)^2 + (k - (D_c r)^2) \mathcal{R}]. \quad (\text{A.12})$$

A.2 Kodama vector and Misner-Sharp mass

While there is no diffeomorphism invariant definition of quasilocal mass in a general spacetime that is only a function of the metric and derivatives of it, there is a family

of such definitions for spherically symmetric spacetimes. This is due to there being a “geometrically preferred” timelike vector in spherically symmetric spacetimes. The simplest quasi-local mass in this family was defined by Misner and Sharp in [MS64]. This mass is also sometimes called the “Hawking mass” and “Misner-Sharp-Hernandez” mass.

To motivate the functional form of the Misner-Sharp mass, we first define the *Kodama vector* [Kod80]

$$k^a \equiv \epsilon^{ab} \nabla_b r, \quad (\text{A.13})$$

where ϵ^{ab} is the Levi-Cevita tensor for the perpendicular space. We see that the Kodama vector is the Hodge dual of the radial vector $\nabla^a r$, and when $\nabla^a r$ is spacelike, k^a is timelike. We next define the *Kodama current*

$$J^a \equiv G^{ab} k_b. \quad (\text{A.14})$$

Despite the use of lower case Latin indices, this is a well-defined four vector; we can think of this expression as $(G^{0a} k_a, G^{1a} k_a, 0, 0)$. In a general spherically symmetric spacetime (*regardless* of whether the Einstein equations hold) a short calculation (see [AV10]) shows us that

$$J^a = -\frac{2}{r^2} \epsilon^{ab} \nabla_b m, \quad (\text{A.15})$$

where we have defined the *Misner-Sharp* mass m

$$m \equiv \frac{r}{2} (1 - (\nabla r)^2). \quad (\text{A.16})$$

From (A.15) we see that $\nabla_\alpha J^\alpha = 0$, and that m is the Noether charge for the conserved current J^α .

So far there is no reason to prefer using the Misner-Sharp mass over any other scalar for the quasi-local mass. For example, the vector

$$J_{(\phi)}^a \equiv \frac{1}{r^2} \epsilon^{ab} \nabla_b \phi, \quad (\text{A.17})$$

where ϕ is any scalar dependent on u^a , is also covariantly conserved in spherical symmetry. If now we assume the Einstein equations $G_{\alpha\beta} = T_{\alpha\beta}$ hold though, we find that m can be simply related to covariant notion of energy density. Defining $r^a \equiv \nabla^a r$, we see that

$$\begin{aligned} r^a \nabla_a m &= \frac{r^2}{2} k^a k^b G_{ab} \\ &= \frac{r^2}{2} k^a k^b T_{ab}. \end{aligned} \tag{A.18}$$

Provided r^a is spacelike, then k^a is timelike, and we can think of this as saying the radial derivative of the Misner-Sharp mass is equal to a radially rescaled energy density, which one could call the *Kodama energy density*.

A.3 Misner-Sharp mass and EdGB gravity

We now investigate how the above arguments hold up when considering modified gravity theories. The Misner-Sharp mass is special as there is a simple covariant formula, Eq. (A.18), relating it to a geometrically preferred energy density. For modified gravity theories the Einstein equations generally do not hold, and modifications of the Misner-Sharp mass have been found for, e.g. Lanczos-Lovelock gravity in five dimensional spacetimes [MN08]. This is because in Lanczos-Lovelock gravity, there is some ambiguity on how to define the “stress-energy” tensor in that theory. In particular, in that theory there is another divergenceless tensor in addition to the Einstein tensor, which we’ll call $\mathcal{G}_{\mu\nu}$. The equations of motion in that theory could then be written

$$G_{\mu\nu} + \mathcal{G}_{\mu\nu} = T_{\mu\nu}, \tag{A.19}$$

where $T_{\mu\nu}$ is the stress-energy tensor of the matter fields, or

$$G_{\mu\nu} = T_{\mu\nu} - \mathcal{G}_{\mu\nu}. \tag{A.20}$$

Thus there are two competing definitions for the stress-energy tensor, $T_{\mu\nu}$ and $T_{\mu\nu} - \mathcal{G}_{\mu\nu}$. If we choose the former, then we find a new formula for a new Misner-Sharp mass in Lanczos-Lovelock gravity [MN08].

For EdGB gravity though, there is essentially only one choice for the (divergenceless) stress-energy tensor. In particular, we have

$$G_{\mu\nu} = -2\delta_{\alpha\beta\rho\sigma}^{\gamma\delta\kappa\lambda} R^{\rho\sigma}{}_{\kappa\lambda} (\nabla^\alpha \nabla_\gamma W) \delta^\beta{}_{(\mu} g_{\nu)\delta} + \nabla_\mu \phi \nabla_\nu \phi + g_{\mu\nu} \left[\frac{1}{2} (\nabla\phi)^2 + V(\phi) \right] + T_{\mu\nu}. \quad (\text{A.21})$$

The R.H.S. is divergenceless, and if we move the dilaton Gauss-Bonnet term to the L.H.S., it not longer would be. This suggests the Misner-Sharp mass as the geometrically preferred quasi-local energy density in spherical symmetry for EdGB gravity.

A.4 Noether charge for shift-symmetric EdGB gravity

In spherically symmetric spacetimes we can find an explicit representation of the Noether charge for EdGB gravity (for a review of Noether's theorem see any of the standard textbooks on field theory; e.g. [PS95, Sre07]).

The Lagrangian density for shift-symmetric EdGB gravity is invariant under *global* shifts in $\phi(x^\mu) \rightarrow \phi(x^\mu) + c$ up to a total divergence:

$$\mathcal{L}_{ssGB} \rightarrow \mathcal{L}_{ssGB} + \lambda c \mathcal{G}. \quad (\text{A.22})$$

Locally we can write $\mathcal{G} = \partial_\mu v^\mu$, where v^μ is a four vector. Calling $\mathcal{J}^\mu \equiv \lambda v^\mu$, the Noether current would then be

$$\begin{aligned} J_{(N)}^\mu &= \frac{\delta \mathcal{L}_{ssGB}}{\delta (\partial_\mu \phi)} - \mathcal{J}^\mu \\ &= -\partial^\mu \phi - \lambda v^\mu, \end{aligned} \quad (\text{A.23})$$

(here we have set $\Delta\phi = 1$, and used $|c| \ll 1$ as the infinitesimal book-keeping parameter). In spherically symmetric spacetimes there is a simple expression for v^μ . Using

Eq. (A.12), and using the fact that the two dimensional Ricci scalar is a total divergence in two dimensions $\mathcal{R} = D_a w^a$, and using the equations of motion in spherical symmetry we have

$$\begin{aligned}\mathcal{G} &= \frac{4}{r^2} [2(\square r)^2 - 2(D_a D_b r)^2 + (k - (D_c r)^2) \mathcal{R}] \\ &= \frac{1}{r^2} D_a [8r (D^a r) D_b D^b r - 8 (D_b r) D^a D^b r + 4w^a].\end{aligned}\quad (\text{A.24})$$

The factor of $1/r^2$ in the front cancels out the r^2 in the metric determinant in the action integral. The Noether current for shift-symmetric EdGB gravity in spherical symmetry is then

$$J_{(N)}^a = -\partial^a \phi - \lambda [8r (D^a r) D_b D^b r - 8 (D_b r) D^a D^b r + 4w^a]. \quad (\text{A.25})$$

To compute the Noether charge over a spacelike hypersurface, one needs to integrate the contraction of this quantity with the unit normal timelike vector over that hypersurface. As the Noether charge is conserved by the evolution equations, evaluating it would be useful mostly as a diagnostic; on the other hand one could define a *quasi-local* Noether charge in a particular set of coordinates by computing

$$q_{(N)} \equiv \int^t dt' \int_0^r dr' J_{(N)}^a n_a, \quad (\text{A.26})$$

although we have found it more convenient² to only evaluate the Misner-Sharp mass in our numerical spherically symmetric evolution of shift-symmetric EdGB gravity.

²and we believe with no important loss of information, although it would be useful to determine if that is actually the case.

Appendix B

An adaptive mesh code for $1 + 1$ dimensional systems

Here we describe an adaptive mesh refinement code that we wrote in C, which is publically available on our github account [Rip20b]. The code is designed to solve systems of hyperbolic partial differential equations and systems of ordinary differential equations (ODEs). A variant of this code (that only employed fixed mesh refinement; the adaptive routine was not used) was used in [RP20b]; see also Chapter (3) of this thesis. As will be discussed in more detail below, the main idea behind the code is the *extrapolation and delayed solution* method described by Choptuik and Pretorius in [PC06] (see also Choptuik’s thesis [Cho86] for a description of an AMR code that solves a hyperbolic-ODE system in $1 + 1$). Some of the main implementation ideas are drawn from Pretorius’ “PAMR” code, which can presently be accessed on Choptuik’s webpage [Cho20]¹,

Some caveats and asides: we have successfully run convergent simulations with a fixed mesh refinement version of this code that used second order finite difference stencils [RP20b]. We have also successfully run stable codes that used the adaptive

¹ Although if you wish to use PAMR for actual computations, a more up-to-date version of the code can be requested from either Frans Pretorius or William East, who has made significant contributions to the PAMR code as well.

features of the AMR code, and which showed some limited evidence of being convergent. Unfortunately, as of this moment the regridding algorithm seems to generate a fair amount of noise at the regridding boundaries, which can only be fully smoothed out with (4th order Kreiss-Oliger [KKOC73]) dissipation after a few time steps. This is to say, the code is still very much in development and more changes may need to be made to it before it could be used for, e.g. critical collapse simulations (for a review of critical collapse see e.g. [GMG07]). We should also mention that at least at the moment the code can only have one refined grid per level. In fact, in retrospect we have found using higher (4th) order difference stencils to be more practical than using fixed mesh refinement around black holes. Moreover for, e.g. 1+2 or 1+3 dimensional systems it will surely be more practical to use professionally developed AMR libraries. Nevertheless developing AMR for coupled hyperbolic and ode systems is sufficiently specialized and simple that at least for the project [RP20b] the month or two spent developing this code seemed to be worthwhile, and we may continue developing this code for specialized research projects (most likely critical collapse problems).

B.1 Adaptive mesh refinement for hyperbolic systems

The original BO (Berger-Oliger) algorithm [BO84] was designed for purely hyperbolic systems of equations. We will only consider finite difference solutions to PDEs (and ODEs). This description of BO AMR will be schematic and we refer the reader to the excellent original article on the subject for more details [BO84]. The basic idea behind BO AMR is to decompose the computational domain into a hierarchy of grids, with grids with finer meshes being contained within grids with coarser meshes. Each finer (“child”) grid is layered on top of the coarser (“parent”) grid. Unlike in [BO84] we will impose the condition that the parent and child grid lines must be parallel to each other; e.g. for 2 : 1 mesh refinement every other grid point of the child grid

must lie exactly on top of a parent grid point (this condition is not restrictive for $1 + 1$ hyperbolic systems as one cannot “rotate” the grids with respect to each other anyways).

The idea is to design the algorithm such that finer grids are placed near solution regions where more resolution is needed. The AMR code as it stands determines this by performing a *truncation error estimate*, which is also how the PAMR and BO algorithms determine where to regrid as well. Consider where the coarser and finer grids overlap, and assume (as our AMR code does) that we use $2 : 1$ mesh refinement. Start on time level n where both the finer and coarser grids overlap. Then take one large step on the coarser level, then two smaller steps on the finer level. The finer and coarser grids are now on the same time level. We label a grid function u at (t_n, x_j) by u_j^n . We assume (following Richardson, e.g. [RG11]) that the error can be expanded polynomially

$${}_c u_j^n = u(t_n, x_j) + e_j^n (\Delta t)^2, \quad (\text{B.1})$$

where u is the solution to the underlying PDE and e_j^n is some (unknown) error function for our discretization. The subscript c in ${}_c u_j^n$ stands for “coarse” (coarser grid). The finer grid solution is

$${}_f u_j^n = u(t_n, x_j) + 2e_j^n \left(\frac{1}{2}\Delta t\right)^2. \quad (\text{B.2})$$

We take the pointwise difference where the grid points overlap to get

$$2\frac{{}_c u_j^n - {}_f u_j^n}{(\Delta t)^2} = e_j^n. \quad (\text{B.3})$$

The subscript f in ${}_f u_j^n$ stands for “fine” (finer grid). In this way we estimate the truncation error with a *shadow hierarchy*. The regions where this error term grows too large are regions that should be overlaid with a finer grid. Note that if we want to perform these truncation error estimates on the base (coarsest) level we in fact need to evolve an even coarser “shadow” grid underneath the base grid.

We use precisely this kind of truncation error estimate in determining where to add finer grids in our AMR code. Every number of predetermined time steps, we make the truncation error estimate over a given fine grid. If there are regions where the difference Eq. (B.3) exceeds some pre-determined error bound, we enclose the convex hull of that region with a finer grid.

B.2 Including Ordinary Differential Equations

The original BO (Berger-Oliger) algorithm [BO84] was designed for purely hyperbolic systems of equations; to include the ordinary differential equation (ODE) constraint equations, we employ the *extrapolation and delayed solution* modification developed for such coupled elliptic/hyperbolic systems [PC06]. For the hyperbolic equations, the solution is obtained on the mesh hierarchy with the usual BO time-stepping procedure : one time step is first taken on a coarse *parent* level before two² steps are taken on the next finer *child* level, and this is repeated recursively down the mesh hierarchy. During this phase the ODEs are not solved, and where the values of the corresponding constrained variables are needed to evaluate terms in the hyperbolic equations, approximations for these variables are obtained via extrapolation from earlier time levels. Instead, the ODEs are solved after the fine-to-coarse level injection phase of the hyperbolic variables, when the advanced time of a given parent level is in sync with all overlapping child levels (thus, on the very finest level this scheme reduces to the unigrid algorithm described in the previous section). For more details see [PC06].

One difference with our system of equations compared to that described in [PC06], is there some form of global relaxation method was assumed for the elliptics, while here the ODE nature of our constraint equations requires integration from the inner to outer boundary. We thus solve the ODEs from the inner to outer boundary, using

²because of our 2 : 1 refinement ratio in space and time.

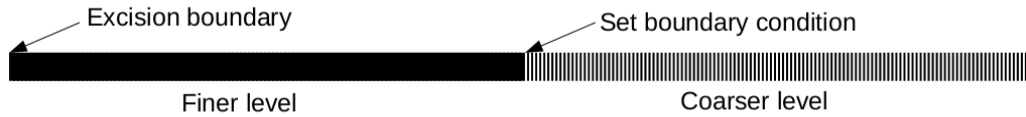


Figure B.1: Setting boundary conditions on next ODE level with fixed mesh refinement, with all finer levels contained inside a coarser level and adjacent to the excision boundary.

the value of the ODE integrated on the adjacent level to the left to set the boundary condition for the ODE to be solved in the domain on the right.

B.3 Fixed mesh refinement around a black hole

Further simplifications to the algorithm are made in [RP20b]. There we use fixed mesh refinement, and the lower boundary of each subgrid lies on the excision boundary inside the black hole. Thus we do not need to extrapolate the initial conditions for the ODEs on each level; instead we can freely evolve the initial conditions on the black hole boundary by using transport equations for the ODE variables which we find from the Einstein/EdGB equations of motion. More details can be found in [RP20b], or in Chptr. (3); see also Fig. (B.1), which is adapted from [RP20b].

Appendix C

Variation of the Gauss-Bonnet scalar

Here we derive equations of motion for the dilaton Gauss-Bonnet term

$$S_{GB} = \int d^4x \sqrt{-g} f(\phi) \mathcal{G}. \quad (\text{C.1})$$

Varying the Gauss-Bonnet term with respect to the metric, we have

$$\begin{aligned} & \delta \left(\sqrt{-g} \frac{1}{4} \delta_{\lambda\sigma\gamma\delta}^{\rho\kappa\alpha\beta} R^{\lambda\sigma}{}_{\rho\kappa} R^{\gamma\delta}{}_{\alpha\beta} \right) = \\ & \sqrt{-g} \frac{1}{4} \delta_{\lambda\sigma\gamma\delta}^{\rho\kappa\alpha\beta} \left(2R^{\lambda\sigma}{}_{\rho\kappa} \delta R^{\gamma\delta}{}_{\alpha\beta} - \frac{1}{2} R^{\lambda\sigma}{}_{\rho\kappa} R^{\gamma\delta}{}_{\alpha\beta} g_{\mu\nu} \delta g^{\mu\nu} \right). \end{aligned} \quad (\text{C.2})$$

We focus on the variation of the Riemann tensor term:

$$\delta_{\lambda\sigma\gamma\delta}^{\rho\kappa\alpha\beta} R^{\lambda\sigma}{}_{\rho\kappa} \delta R^{\gamma\delta}{}_{\alpha\beta} = \delta_{\lambda\sigma\gamma\delta}^{\rho\kappa\alpha\beta} \left(R^{\lambda\sigma}{}_{\rho\kappa} R^{\gamma}{}_{\omega\alpha\beta} \delta g^{\omega\delta} + R^{\lambda\sigma}{}_{\rho\kappa} g^{\omega\delta} \delta R^{\gamma}{}_{\omega\alpha\beta} \right). \quad (\text{C.3})$$

In four dimensions, a five index antisymmetric tensor is zero, so we may write (c.f. Appendix A and B of [tHV74])

$$\begin{aligned} & \delta_{\lambda\sigma\gamma\delta}^{\rho\kappa\alpha\beta} g_{\omega\lambda} R^{\lambda\sigma}{}_{\rho\kappa} R^{\gamma\omega}{}_{\alpha\beta} \delta g^{\omega\delta} = \\ & \left(\delta_{\lambda\sigma\gamma\delta}^{\rho\kappa\alpha\beta} g_{\omega\lambda} + \delta_{\lambda\omega\gamma\delta}^{\rho\kappa\alpha\beta} g_{\omega\sigma} + \delta_{\lambda\sigma\gamma\delta}^{\rho\kappa\alpha\beta} g_{\omega\gamma} + \delta_{\lambda\sigma\gamma\delta}^{\rho\kappa\alpha\beta} g_{\omega\delta} \right) R^{\lambda\sigma}{}_{\rho\kappa} R^{\gamma\omega}{}_{\alpha\beta} \delta g^{\omega\delta}, \end{aligned} \quad (\text{C.4})$$

which implies

$$\delta_{\lambda\sigma\gamma\delta}^{\rho\kappa\alpha\beta} R^{\lambda\sigma}{}_{\rho\kappa} R^{\gamma}{}_{\omega\alpha\beta} \delta g^{\omega\delta} = \frac{1}{4} \delta_{\lambda\sigma\gamma\delta}^{\rho\kappa\alpha\beta} R^{\lambda\sigma}{}_{\rho\kappa} R^{\gamma\delta}{}_{\alpha\beta} g_{\mu\nu} \delta g^{\mu\nu}. \quad (\text{C.5})$$

We conclude that in four spacetime dimensions, the variation of the Gauss-Bonnet term with respect to the metric is

$$\begin{aligned} \delta \left(\sqrt{-g} \frac{1}{4} \delta_{\lambda\sigma\gamma\delta}^{\rho\kappa\alpha\beta} R^{\lambda\sigma}{}_{\rho\kappa} R^{\gamma\delta}{}_{\alpha\beta} \right) &= \sqrt{-g} \frac{1}{2} \delta_{\lambda\sigma\gamma\delta}^{\rho\kappa\alpha\beta} R^{\lambda\sigma}{}_{\rho\kappa} g^{\omega\delta} \delta R^{\gamma}{}_{\omega\alpha\beta} \\ &= \sqrt{-g} \delta_{\lambda\sigma\gamma\delta}^{\rho\kappa\alpha\beta} R^{\lambda\sigma}{}_{\rho\kappa} g^{\omega\delta} g^{\gamma\iota} \nabla_{\alpha} \nabla_{\omega} \delta g_{\iota\beta}. \end{aligned} \quad (\text{C.6})$$

Relabeling indices, and noting that from the Bianchi identities $\delta_{\lambda\sigma\gamma\delta}^{\rho\kappa\alpha\beta} R^{\lambda\sigma}{}_{\rho\kappa}$ is divergenceless on all its indices (e.g. [MTW17] §13.5) the variation of the dilaton Gauss-Bonnet term is

$$\delta S_{GB} = -\delta_{\beta\alpha\rho\sigma}^{\gamma\delta\kappa\lambda} R^{\rho\sigma}{}_{\kappa\lambda} (\nabla_{\gamma} \nabla^{\alpha} f(\phi)) \delta_{\mu}^{\beta} g_{\nu\delta} \delta g^{\mu\nu}, \quad (\text{C.7})$$

plus surface terms. Note that if we set $f(\phi) = 1$, then the variation of S_{GB} produces *only* surface terms. A review of how in this case S_{GB} relates to the topology of the four dimensional manifold (the ‘‘Chern-Gauss-Bonnet’’ theorem) is contained in [Nak18].

Using similar manipulations as presented above, we note that taking the divergence of the Gauss-Bonnet tensor is

$$\begin{aligned} \nabla^{\mu} \left(\delta_{\alpha\beta\rho\sigma}^{\gamma\delta\kappa\lambda} R^{\rho\sigma}{}_{\kappa\lambda} (\nabla_{\gamma} \nabla^{\alpha} f(\phi)) \delta_{\mu}^{\beta} g_{\nu\delta} \right) &= \frac{1}{2} g_{\nu\delta} R^{\rho\sigma}{}_{\kappa\lambda} R_{\gamma\omega}{}^{\beta\alpha} \delta_{\alpha\beta\rho\sigma}^{\gamma\delta\kappa\lambda} \nabla^{\omega} \phi \\ &= -\frac{1}{2} \mathcal{G} \nabla_{\nu} f(\phi). \end{aligned} \quad (\text{C.8})$$

so that assuming $\nabla_{\nu} \phi \neq 0$, taking the divergence of Eq. (2.2a) gives us Eq. (2.2b) (the ‘‘generalized Bianchi identity’’ [TO17]).

Appendix D

Decoupled scalar profile for linear EdGB coupling

For reference, we present the decoupled scalar solutions for EdGB gravity in Schwarzschild and Painlevé-Gullstrand coordinates. The decoupling limit for EdGB gravity is the solution of the scalar wave equation

$$\square\phi + \lambda\mathcal{R}_{GB} = 0, \quad (\text{D.1})$$

about a GR background. In this thesis we worked in Schwarzschild and Painlevé-Gullstrand coordinates:

$$ds^2 = -e^{2A(t,r)}dt^2 + e^{2B(t,r)}dr^2 + r^2(d\vartheta^2 + \sin^2\vartheta d\varphi^2), \quad (\text{D.2a})$$

$$ds^2 = -\alpha(t,r)dt^2 + (dt + \alpha(t,r)\zeta(t,r)dr)^2 + r^2(d\vartheta^2 + \sin^2\vartheta d\varphi^2). \quad (\text{D.2b})$$

Since ϕ is a scalar, and since in both coordinate systems r is the areal radius, the static decoupled scalar profiles for ϕ about a Schwarzschild black hole solution is the same for in coordinate systems. We present the calculation in Schwarzschild coordinates.

Since ϕ is a scalar, and

$$ds^2 = -\left(1 - \frac{2M}{r}\right)dt^2 + \left(1 - \frac{2M}{r}\right)^{-1}dr^2 + r^2(d\vartheta^2 + \sin^2\vartheta d\varphi^2). \quad (\text{D.3})$$

With this, Eq. (D.1) reduces to

$$\frac{1}{r^2} \frac{d}{dr} \left(r^2 \left(1 - \frac{2M}{r} \right) \frac{d\phi}{dr} \right) + \lambda \frac{48M^2}{r^6} = 0. \quad (\text{D.4})$$

Imposing regularity of $\partial_r \phi$ at the geometric horizon $r = 2M$, setting $\lim_{r \rightarrow \infty} \phi = 0$, and changing variables to $x \equiv r/M$, we obtain

$$\phi(x) = \frac{2\lambda}{M^2} \left(\frac{1}{x} + \frac{1}{x^2} + \frac{4}{3x^3} \right). \quad (\text{D.5})$$

References

- [A⁺16a] B. P. Abbott et al. Tests of general relativity with GW150914. *Phys. Rev. Lett.*, 116(22):221101, 2016, 1602.03841.
- [A⁺16b] B.P. Abbott et al. Observation of Gravitational Waves from a Binary Black Hole Merger. *Phys. Rev. Lett.*, 116(6):061102, 2016, 1602.03837.
- [A⁺18] N. Aghanim et al. Planck 2018 results. VI. Cosmological parameters. 7 2018, 1807.06209.
- [A⁺19] B. P. Abbott et al. Tests of General Relativity with GW170817. *Phys. Rev. Lett.*, 123(1):011102, 2019, 1811.00364.
- [ABB⁺99] E. Anderson, Z. Bai, C. Bischof, S. Blackford, J. Demmel, J. Dongarra, J. Du Croz, A. Greenbaum, S. Hammarling, A. McKenney, and D. Sorensen. *LAPACK Users' Guide*. Society for Industrial and Applied Mathematics, Philadelphia, PA, third edition, 1999.
- [ABCL05] R. J. Adler, J. D. Bjorken, P. Chen, and J. S. Liu. Simple analytic models of gravitational collapse. *Am. J. Phys.*, 73:1148–1159, 2005, gr-qc/0502040.
- [AGS11] Ratindranath Akhoury, David Garfinkle, and Ryo Saotome. Gravitational collapse of k-essence. *JHEP*, 04:096, 2011, 1103.0290.

- [AHS11] K. Atkinson, W. Han, and D.E. Stewart. *Numerical Solution of Ordinary Differential Equations*. Pure and Applied Mathematics: A Wiley Series of Texts, Monographs and Tracts. Wiley, 2011.
- [AK04] A. Ashtekar and B. Krishnan. Isolated and Dynamical Horizons and Their Applications. *Living Reviews in Relativity*, 7:10, December 2004, gr-qc/0407042.
- [AL19] Gwyneth Allwright and Luis Lehner. Towards the nonlinear regime in extensions to GR: assessing possible options. *Class. Quant. Grav.*, 36(8):084001, 2019, 1808.07897.
- [AV10] Gabriel Abreu and Matt Visser. Kodama time: Geometrically preferred foliations of spherically symmetric spacetimes. *Phys. Rev.*, D82:044027, 2010, 1004.1456.
- [AYY14] Dimitry Ayzenberg, Kent Yagi, and Nicolas Yunes. Linear Stability Analysis of Dynamical Quadratic Gravity. *Phys. Rev.*, D89(4):044023, 2014, 1310.6392.
- [BCH73] J. M. Bardeen, B. Carter, and S. W. Hawking. The four laws of black hole mechanics. *Communications in Mathematical Physics*, 31:161–170, June 1973.
- [BCS09] Emanuele Berti, Vitor Cardoso, and Andrei O. Starinets. Quasinormal modes of black holes and black branes. *Class. Quant. Grav.*, 26:163001, 2009, 0905.2975.
- [BD61] C. Brans and R. H. Dicke. Mach’s principle and a relativistic theory of gravitation. *Phys. Rev.*, 124:925–935, Nov 1961.

- [BLL19] Laura Bernard, Luis Lehner, and Raimon Luna. Challenges to global solutions in Horndeski's theory. *Phys. Rev.*, D100(2):024011, 2019, 1904.12866.
- [BO84] Marsha J. Berger and Joseph Oliger. Adaptive Mesh Refinement for Hyperbolic Partial Differential Equations. *Journal of Computational Physics*, 53(3):484–512, Mar 1984.
- [BSDKY18] Jose Luis Blázquez-Salcedo, Daniela D. Doneva, Jutta Kunz, and Stoytcho S. Yazadjiev. Radial perturbations of the scalarized Einstein-Gauss-Bonnet black holes. *Phys. Rev.*, D98(8):084011, 2018, 1805.05755.
- [BSMC⁺16] Jose Luis Blazquez-Salcedo, Caio F. B. Macedo, Vitor Cardoso, Valeria Ferrari, Leonardo Gualtieri, Feich Scen Khoo, Jutta Kunz, and Paolo Pani. Perturbed black holes in Einstein-dilaton-Gauss-Bonnet gravity: Stability, ringdown, and gravitational-wave emission. *Phys. Rev.*, D94(10):104024, 2016, 1609.01286.
- [BSW16] Robert Benkel, Thomas P. Sotiriou, and Helvi Witek. Dynamical scalar hair formation around a schwarzschild black hole. *Phys. Rev. D*, 94:121503, Dec 2016.
- [BSW17] Robert Benkel, Thomas P. Sotiriou, and Helvi Witek. Black hole hair formation in shift-symmetric generalised scalar-tensor gravity. *Class. Quant. Grav.*, 34(6):064001, 2017, 1610.09168.
- [Bur04] C.P. Burgess. Quantum gravity in everyday life: General relativity as an effective field theory. *Living Rev. Rel.*, 7:5–56, 2004, gr-qc/0311082.
- [Bur15] C.P. Burgess. The Cosmological Constant Problem: Why it's hard to get Dark Energy from Micro-physics. In *100e Ecole d'Ete de Physique: Post-Planck Cosmology*, pages 149–197, 2015, 1309.4133.

- [Car04] Sean M. Carroll. *Spacetime and geometry: An introduction to general relativity*. 2004.
- [CB08] Y. Choquet-Bruhat. *General Relativity and the Einstein Equations*. Oxford Mathematical Monographs. OUP Oxford, 2008.
- [CFLT13] Tai-jun Chen, Matteo Fasiello, Eugene A. Lim, and Andrew J. Tolley. Higher derivative theories with constraints: Exorcising Ostrogradski’s Ghost. *JCAP*, 1302:042, 2013, 1209.0583.
- [CH62] R. Courant and D. Hilbert. *Methods of Mathematical Physics*. Number v. 2 in *Methods of Mathematical Physics*. Interscience Publishers, 1962.
- [Cho86] Matthew William Choptuik. *A study of numerical techniques for radiative problems in general relativity*. PhD thesis, University of British Columbia, 1986.
- [Cho93] Matthew W. Choptuik. Universality and scaling in gravitational collapse of a massless scalar field. *Phys. Rev. Lett.*, 70:9–12, 1993.
- [Cho20] Matthew Choptuik. UBC numerical relativity: Software and related, 2020. <http://laplace.physics.ubc.ca/Group/Software.html>.
- [Chr94] Demetrios Christodoulou. Examples of naked singularity formation in the gravitational collapse of a scalar field. *Annals of Mathematics*, 140(3):607–653, 1994.
- [Chr08] D. Christodoulou. *Mathematical Problems of General Relativity I*. *Mathematical Problems of General Relativity*. European Mathematical Society, Zurich, 2008.
- [CNT10] Paolo Creminelli, Alberto Nicolis, and Enrico Trincherini. Galilean Genesis: An Alternative to inflation. *JCAP*, 1011:021, 2010, 1007.0027.

- [COL17] Juan Cayuso, Néstor Ortiz, and Luis Lehner. Fixing extensions to general relativity in the nonlinear regime. *Phys. Rev.*, D96(8):084043, 2017, 1706.07421.
- [Col19] Alan A. Coley. Mathematical General Relativity. *Gen. Rel. Grav.*, 51(6):78, 2019, 1807.08628.
- [DY18] Daniela D. Doneva and Stoytcho S. Yazadjiev. New gauss-bonnet black holes with curvature-induced scalarization in extended scalar-tensor theories. *Phys. Rev. Lett.*, 120:131103, Mar 2018.
- [ea15] Emanuele Berti et. al. Testing general relativity with present and future astrophysical observations. *Classical and Quantum Gravity*, 32(24):243001, dec 2015.
- [EGHS17] Solomon Endlich, Victor Gorbenko, Junwu Huang, and Leonardo Senatore. An effective formalism for testing extensions to General Relativity with gravitational waves. 2017, 1704.01590.
- [Eic19] Astrid Eichhorn. An asymptotically safe guide to quantum gravity and matter. *Front. Astron. Space Sci.*, 5:47, 2019, 1810.07615.
- [Eva10] L.C. Evans. *Partial Differential Equations*. Graduate studies in mathematics. American Mathematical Society, 2010.
- [FdC13] F. Flaherty and M. do Carmo. *Riemannian Geometry*. Mathematics: Theory & Applications. Birkhäuser Boston, 2013.
- [FK95] U. Frisch and A.N. Kolmogorov. *Turbulence: The Legacy of A. N. Kolmogorov*. Cambridge University Press, 1995.
- [FN12] Valeri Frolov and Igor Novikov. *Black hole physics: basic concepts and new developments*, volume 96. Springer Science & Business Media, New York, 2012.

- [FPD39] M. Fierz, Wolfgang Ernst Pauli, and Paul Adrien Maurice Dirac. On relativistic wave equations for particles of arbitrary spin in an electromagnetic field. *Proceedings of the Royal Society of London. Series A. Mathematical and Physical Sciences*, 173(953):211–232, 1939, <https://royalsocietypublishing.org/doi/pdf/10.1098/rspa.1939.0140>.
- [FSW93] John L. Friedman, Kristin Schleich, and Donald M. Witt. Topological censorship. *Phys. Rev. Lett.*, 71:1486–1489, Sep 1993.
- [Ger96] Robert P. Geroch. Partial differential equations of physics. In *General relativity. Proceedings, 46th Scottish Universities Summer School in Physics, NATO Advanced Study Institute, Aberdeen, UK, July 16-29, 1995*, 1996, gr-qc/9602055.
- [GK99] Nigel Goldenfeld and Leo P. Kadanoff. Simple lessons from complexity. *Science*, 284(5411):87–89, 1999, <https://science.sciencemag.org/content/284/5411/87.full.pdf>.
- [GKO95] B. Gustafsson, H.O. Kreiss, and J. Olinger. *Time Dependent Problems and Difference Methods*. A Wiley-Interscience Publication. Wiley, 1995.
- [GMG07] Carsten Gundlach and Jose M. Martin-Garcia. Critical phenomena in gravitational collapse. *Living Rev. Rel.*, 10:5, 2007, 0711.4620.
- [GS87] David J. Gross and John H. Sloan. The Quartic Effective Action for the Heterotic String. *Nucl. Phys.*, B291:41–89, 1987.
- [GSWW99] G. J. Galloway, K. Schleich, D. M. Witt, and E. Woolgar. Topological censorship and higher genus black holes. *Phys. Rev.*, D60:104039, 1999, gr-qc/9902061.

- [GVL13] G.H. Golub and C.F. Van Loan. *Matrix Computations*. Johns Hopkins Studies in the Mathematical Sciences. Johns Hopkins University Press, 2013.
- [Hay94] Sean A. Hayward. General laws of black-hole dynamics. *Phys. Rev. D*, 49:6467–6474, Jun 1994.
- [Hay96] Sean A. Hayward. Gravitational energy in spherical symmetry. *Phys. Rev.*, D53:1938–1949, 1996, gr-qc/9408002.
- [HE75] Stephen W. Hawking and G. F. R. Ellis. *The Large Scale Structure of Space-Time (Cambridge Monographs on Mathematical Physics)*. Cambridge University Press, 1975.
- [Hin12] Kurt Hinterbichler. Theoretical Aspects of Massive Gravity. *Rev. Mod. Phys.*, 84:671–710, 2012, 1105.3735.
- [Hor74] Gregory Walter Horndeski. Second-order scalar-tensor field equations in a four-dimensional space. *International Journal of Theoretical Physics*, 10(6):363–384, 1974.
- [HR14] Carlos A. R. Herdeiro and Eugen Radu. Kerr black holes with scalar hair. *Phys. Rev. Lett.*, 112:221101, 2014, 1403.2757.
- [IK15] Alexandru Ionescu and Sergiu Klainerman. Rigidity Results in General Relativity: a Review. 1 2015, 1501.01587.
- [IRS16] Anna Ijjas, Justin Ripley, and Paul J. Steinhardt. NEC violation in mimetic cosmology revisited. *Phys. Lett.*, B760:132–138, 2016, 1604.08586.
- [IS79] W. Israel and J. M. Stewart. Transient relativistic thermodynamics and kinetic theory. *Annals Phys.*, 118:341–372, 1979.

- [IS17] Anna Ijjas and Paul J. Steinhardt. Fully stable cosmological solutions with a non-singular classical bounce. *Phys. Lett. B*, 764:289–294, 2017, 1609.01253.
- [KKOC73] H. Kreiss, H.O. Kreiss, J. Olinger, and Global Atmospheric Research Programme. Joint Organizing Committee. *Methods for the approximate solution of time dependent problems*. GARP publications series. International Council of Scientific Unions, World Meteorological Organization, 1973.
- [KL89] H.O. Kreiss and J. Lorenz. *Initial-boundary Value Problems and the Navier-Stokes Equations*. Number v. 136 in Initial-boundary value problems and the Navier-Stokes equations. Academic Press, 1989.
- [KMR⁺96] P. Kanti, N. E. Mavromatos, J. Rizos, K. Tamvakis, and E. Winstanley. Dilatonic black holes in higher curvature string gravity. *Phys. Rev.*, D54:5049–5058, 1996, hep-th/9511071.
- [Kob19] Tsutomu Kobayashi. Horndeski theory and beyond: a review. *Rept. Prog. Phys.*, 82(8):086901, 2019, 1901.07183.
- [Kod80] Hideo Kodama. Conserved Energy Flux for the Spherically Symmetric System and the Back Reaction Problem in the Black Hole Evaporation. *Prog. Theor. Phys.*, 63:1217, 1980.
- [Kov19] Áron D. Kovács. Well-posedness of cubic Horndeski theories. *Phys. Rev. D*, 100(2):024005, 2019, 1904.00963.
- [KR20a] Aron D. Kovacs and Harvey S. Reall. Well-posed formulation of Lovelock and Horndeski theories. *Phys. Rev. D*, 101(12):124003, 2020, 2003.08398.

- [KR20b] Aron D. Kovacs and Harvey S. Reall. Well-posed formulation of scalar-tensor effective field theory. *Phys. Rev. Lett.*, 124(22):221101, 2020, 2003.04327.
- [KSH11] Yuki Kanai, Masaru Siino, and Akio Hosoya. Gravitational collapse in Painleve-Gullstrand coordinates. *Prog. Theor. Phys.*, 125:1053–1065, 2011, 1008.0470.
- [KYY11] Tsutomu Kobayashi, Masahide Yamaguchi, and Jun’ichi Yokoyama. Generalized G-inflation: Inflation with the most general second-order field equations. *Prog. Theor. Phys.*, 126:511–529, 2011, 1105.5723.
- [Lax73] P.D. Lax. *Hyperbolic Systems of Conservation Laws and the Mathematical Theory of Shock Waves*. Number nos. 11-16 in CBMS-NSF Regional Conference Series in Applied Mathematics. Society for Industrial and Applied Mathematics, 1973.
- [Lis17] Mariangela Lisanti. Lectures on Dark Matter Physics. In *Proceedings, Theoretical Advanced Study Institute in Elementary Particle Physics: New Frontiers in Fields and Strings (TASI 2015): Boulder, CO, USA, June 1-26, 2015*, pages 399–446, 2017, 1603.03797.
- [Lov71] D. Lovelock. The Einstein tensor and its generalizations. *J. Math. Phys.*, 12:498–501, 1971.
- [LZKM11] C. Danielle Leonard, Jonathan Ziprick, Gabor Kunstatter, and Robert B. Mann. Gravitational collapse of K-essence Matter in Painlevé-Gullstrand coordinates. *JHEP*, 10:028, 2011, 1106.2054.
- [Mag08] M. Maggiore. *Gravitational Waves: Volume 1: Theory and Experiments*. Gravitational Waves. OUP Oxford, 2008.

- [Mat05] Samir D. Mathur. The Fuzzball proposal for black holes: An Elementary review. *Fortsch. Phys.*, 53:793–827, 2005, hep-th/0502050.
- [MI19] Masato Minamitsuji and Taishi Ikeda. Scalarized black holes in the presence of the coupling to gauss-bonnet gravity. *Phys. Rev. D*, 99:044017, Feb 2019.
- [MM01] Pawel O. Mazur and Emil Mottola. Gravitational condensate stars: An alternative to black holes. 2001, gr-qc/0109035.
- [MN08] Hideki Maeda and Masato Nozawa. Generalized Misner-Sharp quasi-local mass in Einstein-Gauss-Bonnet gravity. *Phys. Rev.*, D77:064031, 2008, 0709.1199.
- [Mor70] Cathleen S. Morawetz. The dirichlet problem for the tricomi equation. *Communications on Pure and Applied Mathematics*, 23(4):587–601, 1970, <https://onlinelibrary.wiley.com/doi/pdf/10.1002/cpa.3160230404>.
- [Mor82] Cathleen S. Morawetz. The mathematical approach to the sonic barrier. *Bull. Amer. Math. Soc. (N.S.)*, 6(2):127–145, 03 1982.
- [MS64] Charles W. Misner and David H. Sharp. Relativistic equations for adiabatic, spherically symmetric gravitational collapse. *Phys. Rev.*, 136:B571–B576, Oct 1964.
- [MSB⁺19] Caio F. B. Macedo, Jeremy Sakstein, Emanuele Berti, Leonardo Gualtieri, Hector O. Silva, and Thomas P. Sotiriou. Self-interactions and Spontaneous Black Hole Scalarization. *Phys. Rev.*, D99(10):104041, 2019, 1903.06784.
- [MTW17] C.W. Misner, K.S. Thorne, and J.A. Wheeler. *Gravitation*. Princeton University Press, 2017.

- [Muk05] Viatcheslav Mukhanov. *Physical Foundations of Cosmology*. Cambridge Univ. Press, Cambridge, 2005.
- [Nak18] M. Nakahara. *Geometry, Topology and Physics*. CRC Press, 2018.
- [Noa83] David R. Noakes. The initial value formulation of higher derivative gravity. *Journal of Mathematical Physics*, 24(7):1846–1850, 1983, <https://doi.org/10.1063/1.525906>.
- [Oko19] Maria Okounkova. Stability of rotating black holes in Einstein dilaton Gauss-Bonnet gravity. 2019, 1909.12251.
- [OSM⁺20] Maria Okounkova, Leo C. Stein, Jordan Moxon, Mark A. Scheel, and Saul A. Teukolsky. Numerical relativity simulation of GW150914 beyond general relativity. *Phys. Rev. D*, 101(10):104016, 2020, 1911.02588.
- [OSSH17] Maria Okounkova, Leo C. Stein, Mark A. Scheel, and Daniel A. Hemberger. Numerical binary black hole mergers in dynamical Chern-Simons gravity: Scalar field. *Phys. Rev.*, D96(4):044020, 2017, 1705.07924.
- [OSST19] Maria Okounkova, Leo C. Stein, Mark A. Scheel, and Saul A. Teukolsky. Numerical binary black hole collisions in dynamical Chern-Simons gravity. *Phys. Rev.*, D100(10):104026, 2019, 1906.08789.
- [OST19] Maria Okounkova, Mark A. Scheel, and Saul A. Teukolsky. Evolving Metric Perturbations in dynamical Chern-Simons Gravity. *Phys. Rev.*, D99(4):044019, 2019, 1811.10713.
- [Otw15] T.H. Otway. *Elliptic–Hyperbolic Partial Differential Equations: A Mini-Course in Geometric and Quasilinear Methods*. SpringerBriefs in Mathematics. Springer International Publishing, 2015.
- [Pap17] Giuseppe Papallo. On the hyperbolicity of the most general Horndeski theory. *Phys. Rev.*, D96(12):124036, 2017, 1710.10155.

- [PC06] Frans Pretorius and Matthew W. Choptuik. Adaptive mesh refinement for coupled elliptic-hyperbolic systems. *J. Comput. Phys.*, 218:246–274, 2006, gr-qc/0508110.
- [Pol98] Joseph Polchinski. *String Theory*, volume 1 of *Cambridge Monographs on Mathematical Physics*. Cambridge University Press, 1998.
- [PR15] Giuseppe Papallo and Harvey S. Reall. Graviton time delay and a speed limit for small black holes in Einstein-Gauss-Bonnet theory. *JHEP*, 11:109, 2015, 1508.05303.
- [PR17] Giuseppe Papallo and Harvey S. Reall. On the local well-posedness of Lovelock and Horndeski theories. *Phys. Rev.*, D96(4):044019, 2017, 1705.04370.
- [PS95] Michael E. Peskin and Daniel V. Schroeder. *An Introduction to quantum field theory*. Addison-Wesley, Reading, USA, 1995.
- [PTVF07] William H. Press, Saul A. Teukolsky, William T. Vetterling, and Brian P. Flannery. *Numerical Recipes 3rd Edition: The Art of Scientific Computing*. Cambridge University Press, USA, 3 edition, 2007.
- [RG11] Lewis Fry Richardson and Richard Tetley Glazebrook. IX. the approximate arithmetical solution by finite differences of physical problems involving differential equations, with an application to the stresses in a masonry dam. *Philosophical Transactions of the Royal Society of London. Series A, Containing Papers of a Mathematical or Physical Character*, 210(459-470):307–357, 1911, <https://royalsocietypublishing.org/doi/pdf/10.1098/rsta.1911.0009>.
- [Rip19] Justin L. Ripley. Excision and avoiding the use of boundary conditions in numerical relativity. *Class. Quant. Grav.*, 36(23):237001, 2019, 1908.04234.

- [Rip20a] Justin Ripley. Spherically symmetric z2 symmetric edgb gravity, v1, June 2020. <https://github.com/JLRipley314/spherically-symmetric-Z2-edgb>.
- [Rip20b] Justin L. Ripley. one-dim-amr, 2020. <https://github.com/JLRipley314/one-dim-amr>.
- [Roo10] Matts Roos. Dark Matter: The evidence from astronomy, astrophysics and cosmology. *arXiv e-prints*, page arXiv:1001.0316, January 2010, 1001.0316.
- [Rov98] Carlo Rovelli. Loop quantum gravity. *Living Rev. Rel.*, 1:1, 1998, gr-qc/9710008.
- [RP19a] Justin L. Ripley and Frans Pretorius. Gravitational collapse in Einstein dilaton-Gauss-Bonnet gravity. *Class. Quant. Grav.*, 36(13):134001, 2019, 1903.07543.
- [RP19b] Justin L. Ripley and Frans Pretorius. Hyperbolicity in Spherical Gravitational Collapse in a Horndeski Theory. *Phys. Rev.*, D99(8):084014, 2019, 1902.01468.
- [RP20a] Justin L. Ripley and Frans Pretorius. Dynamics of a Z2 symmetric EdGB gravity in spherical symmetry. *Classical and Quantum Gravity*, 5 2020, 2005.05417.
- [RP20b] Justin L. Ripley and Frans Pretorius. Scalarized Black Hole dynamics in Einstein dilaton Gauss-Bonnet Gravity. *Phys. Rev.*, D101(4):044015, 2020, 1911.11027.
- [Rub14] V. A. Rubakov. The Null Energy Condition and its violation. *Phys. Usp.*, 57:128–142, 2014, 1401.4024. [Usp. Fiz. Nauk184,no.2,137(2014)].

- [RY18] Justin L. Ripley and Kent Yagi. Black hole perturbation under a $2 + 2$ decomposition in the action. *Phys. Rev.*, D97(2):024009, 2018, 1705.03068.
- [Sci53] D. W. Sciama. On the Origin of Inertia. *Monthly Notices of the Royal Astronomical Society*, 113(1):34–42, 02 1953, <https://academic.oup.com/mnras/article-pdf/113/1/34/8074129/mnras113-0034.pdf>.
- [Sho07] Assaf Shomer. A Pedagogical explanation for the non-renormalizability of gravity. 9 2007, 0709.3555.
- [SMS⁺19] Hector O. Silva, Caio F. B. Macedo, Thomas P. Sotiriou, Leonardo Gualtieri, Jeremy Sakstein, and Emanuele Berti. Stability of scalarized black hole solutions in scalar-gauss-bonnet gravity. *Phys. Rev. D*, 99:064011, Mar 2019.
- [Sot15] Thomas P. Sotiriou. Black Holes and Scalar Fields. *Class. Quant. Grav.*, 32(21):214002, 2015, 1505.00248.
- [Sre07] Mark Srednicki. *Quantum Field Theory*. Cambridge Univ. Press, Cambridge, 2007.
- [SSG⁺18] Hector O. Silva, Jeremy Sakstein, Leonardo Gualtieri, Thomas P. Sotiriou, and Emanuele Berti. Spontaneous scalarization of black holes and compact stars from a Gauss-Bonnet coupling. *Phys. Rev. Lett.*, 120(13):131104, 2018, 1711.02080.
- [ST12] Olivier Sarbach and Manuel Tiglio. Continuum and Discrete Initial-Boundary-Value Problems and Einstein’s Field Equations. *Living Rev. Rel.*, 15:9, 2012, 1203.6443.

- [SZ14a] Thomas P. Sotiriou and Shuang-Yong Zhou. Black hole hair in generalized scalar-tensor gravity. *Phys. Rev. Lett.*, 112:251102, 2014, 1312.3622.
- [SZ14b] Thomas P. Sotiriou and Shuang-Yong Zhou. Black hole hair in generalized scalar-tensor gravity: An explicit example. *Phys. Rev.*, D90:124063, 2014, 1408.1698.
- [Sza09] László B. Szabados. Quasi-local energy-momentum and angular momentum in general relativity. *Living Reviews in Relativity*, 12(1):4, Jun 2009.
- [TFL18] Oliver J. Tattersall, Pedro G. Ferreira, and Macarena Lagos. Speed of gravitational waves and black hole hair. *Phys. Rev.*, D97(8):084005, 2018, 1802.08606.
- [Tho07] Jonathan Thornburg. Event and apparent horizon finders for 3 + 1 numerical relativity. *Living Reviews in Relativity*, 10(1):3, Jun 2007.
- [tHV74] Gerard 't Hooft and M. J. G. Veltman. One loop divergencies in the theory of gravitation. *Ann. Inst. H. Poincare Phys. Theor.*, A20:69–94, 1974.
- [TO17] Norihiro Tanahashi and Seiju Ohashi. Wave propagation and shock formation in the most general scalar–tensor theories. *Class. Quant. Grav.*, 34(21):215003, 2017, 1704.02757.
- [Wal84] Robert M Wald. *General relativity*. Chicago Univ. Press, Chicago, IL, 1984.
- [Wei72] S. Weinberg. *Gravitation and cosmology: principles and applications of the general theory of relativity*. Wiley, 1972.
- [Wei89] Steven Weinberg. The cosmological constant problem. *Rev. Mod. Phys.*, 61:1–23, Jan 1989.

- [WGPS19] Helvi Witek, Leonardo Gualtieri, Paolo Pani, and Thomas P. Sotiriou. Black holes and binary mergers in scalar Gauss-Bonnet gravity: scalar field dynamics. *Phys. Rev.*, D99(6):064035, 2019, 1810.05177.
- [Whi11] G.B. Whitham. *Linear and Nonlinear Waves*. Pure and Applied Mathematics: A Wiley Series of Texts, Monographs and Tracts. Wiley, 2011.
- [Wil14] Clifford M. Will. The Confrontation between General Relativity and Experiment. *Living Rev. Rel.*, 17:4, 2014, 1403.7377.
- [Woo15] Richard P. Woodard. Ostrogradsky’s theorem on Hamiltonian instability. *Scholarpedia*, 10(8):32243, 2015, 1506.02210.
- [YSY16] Kent Yagi, Leo C. Stein, and Nicolas Yunes. Challenging the Presence of Scalar Charge and Dipolar Radiation in Binary Pulsars. *Phys. Rev.*, D93(2):024010, 2016, 1510.02152.
- [YYP16] Nicolas Yunes, Kent Yagi, and Frans Pretorius. Theoretical Physics Implications of the Binary Black-Hole Mergers GW150914 and GW151226. *Phys. Rev.*, D94(8):084002, 2016, 1603.08955.
- [ZK09] Jonathan Ziprick and Gabor Kunstatter. Numerical study of black-hole formation in painlevé-gullstrand coordinates. *Phys. Rev. D*, 79:101503, May 2009.
- [Zwi85] Barton Zwiebach. Curvature Squared Terms and String Theories. *Phys. Lett.*, 156B:315–317, 1985.